

# **Cartilage Properties Quantified With 7T MRI**

**Sander Brinkhof**

Cartilage properties quantified with 7T MRI  
PhD Thesis, Utrecht University, the Netherlands

Cover and illustrations design: Floor Beugels  
Lay-out design: Sander Brinkhof  
Printed by: ProefschriftMaken  
ISBN: 978-90-393-7289-0

Financial support for the publication of this thesis from WaveTronica, Össur and  
ChipSoft is gratefully acknowledged.

© 2020 Sander Brinkhof

# **Cartilage Properties Quantified With 7T MRI**

## **Kraakbeeneigenschappen gekwantificeerd met 7T MRI**

(met een samenvatting in het Nederlands)

### **Proefschrift**

ter verkrijging van de graad van doctor aan de Universiteit Utrecht  
op gezag van de rector magnificus, prof. dr. H.R.B.M. Kummeling,  
ingevolge het besluit van het college voor promoties  
in het openbaar te verdedigen op

donderdag 12 november 2020 des middags te 12.45 uur

door

**Sander Brinkhof**

geboren op 25 augustus 1991

te Deventer

**Promotoren:**

Prof. dr. D.W.J. Klomp

Prof. dr. K. Ito





## Contents

<b>Chapter 1</b>	Introduction	<b>9</b>
<b>Chapter 2</b>	Uncompromised MRI of knee cartilage while incorporating sensitive sodium MRI	<b>19</b>
<b>Chapter 3</b>	Can sodium MRI be used as a method for mapping of cartilage stiffness?	<b>33</b>
<b>Chapter 4</b>	T2* mapping in an equine articular groove model - visualizing changes in collagen orientation	<b>49</b>
<b>Chapter 5</b>	Detection of early cartilage damage: feasibility and potential of gagCEST imaging at 7T	<b>63</b>
<b>Chapter 6</b>	In Vivo Cartilage Quantification with gagCEST MRI: Correlation with Cartilage Properties	<b>79</b>
<b>Chapter 7</b>	Summary and general discussion	<b>93</b>
	Appendices	<b>103</b>

The image consists of a uniform, solid black field with no visible features, patterns, or variations in color.



# Introduction



## Introduction

This thesis summarizes work jointly carried out with clinicians (departments of Orthopaedic Surgery and Rheumatology) and engineers/physicists (Radiology), fitting my background in technical medicine. Therefore, this introduction is set out in a manner that both disciplines will understand the topic at hand, in this case imaging of the knee. This thesis aims to apply a number of MRI methods to quantify the quality of articular cartilage. The introduction starts by explaining the biology of articular cartilage and its common pathologies with corresponding treatments. Consequently, the gold standard diagnostic modalities are set out, where after the biochemical MRI methods as used in this thesis are described. Lastly, the outline of this thesis will be explained.

### Articular cartilage biology

Articular cartilage is a unique connective tissue covering the ends of bone in the joints, ensuring the joint can articulate smoothly and withstand heavy loads. Articular cartilage is about 2 to 4 mm thick and consists of hyaline cartilage. This specific type of cartilage contains a small number of specialized cells which are called chondrocytes, embedded in an extracellular matrix (ECM) mostly composed of collagens and glycosaminoglycans (GAGs). These chondrocytes are sparsely distributed throughout the cartilage in their own lacunae and take care of the breakdown of old cells and synthesis of new cells in their own micro-environment. The chondrocytes are in charge of forming the extracellular matrix, mainly to organize the content into an ordered structure. Though, since the chondrocytes aren't available in high abundance, cartilage has a hard time repairing itself when damage occurs.

The extracellular matrix is composed of several macromolecules (mostly collagens and GAGs) and fluid (water with dissolved electrolytes, such as sodium, calcium and magnesium). The content distribution of the extracellular matrix is not homogenous but varies with depth. From the top down, four zones can be identified: the superficial zone, the middle zone, the deep zone and the calcified zone<sup>1</sup>. The superficial zone accounts for about 10 to 20% of the thickness of the cartilage, the middle zone 40-60% and the deep zone 30-40% of the thickness of the cartilage. The most important characteristic of the ECM is that the macromolecular-fluid interaction causes the cartilage to be stiff. The fluid part accounts for 65 to 80% of the total weight, whereas the collagens and GAGs account for the remaining weight. The fluid also incorporates inorganic cations, mostly sodium.

Collagen fibrils, mostly type II, form a tight and dense network acting as the backbone of cartilage. An osmotic swelling pressure is caused by the negative charge of the GAGs attracting free cations, which is counterbalanced by the tensile stress provided

## Chapter 1

by the densely packed collagen fibrils. The GAGs also give the cartilage the ability to resist compression<sup>2</sup>. The superficial zone mostly has collagen fibrils oriented parallel to the bone-cartilage interface, whereas the fibrils are oriented perpendicular to the surface within the deep zone. The intermediate middle zone has a random, crossing-fiber orientation. In the deep zone, GAG content is high and water concentration is low, compared to the middle and superficial zones.

The GAGs in the cartilage are negatively charged due to their carboxyl and sulphate groups, inflicting a negative fixed charge density (FCD) onto the ECM<sup>3</sup>. Consequently, positive free ions are attracted into the ECM to preserve electroneutrality<sup>4</sup>. Ultimately, this increased ion concentration and therefore osmotic pressure creates a swelling pressure which enables the compressive resistance of cartilage<sup>5,6</sup>. The hydrophilic capacity of cartilage can decrease because of loss of GAGs. With this decreased hydration capacity, under high load, this will lead to thinning and 'drying' of the cartilage leading to faster wear and tear<sup>5</sup>.

### Cartilage pathology & treatments

Cartilage pathology is often divided into two types, being focal cartilage lesions (or defects) and degenerative lesions. The first often occurs due to trauma and is often delineated, where the latter is often part of degenerative disease which is often seen in the elderly population. These degenerative lesions are often poorly delineated and more diffuse compared to focal lesions.

#### *Focal defects*

Focal cartilage defects are often seen in the general population, causing morbid pain and functional impairment<sup>7</sup>. Often trauma is the cause of these focal defects, for example due to sports injuries or accidents. The shearing force of the trauma causes a (stress) fracture within the cartilage or even through the subchondral bone. Focal cartilage defects are scored during arthroscopy using the ICRS grading system, ranging from grade 0 (healthy, normal cartilage) to grade 4 (full thickness defects with denuded bone)<sup>8</sup>. Actual structural loss of cartilage is observed from grade 2 onwards.

Early treatment of these focal cartilage defects includes debridement (i.e. cleaning of the defect) and removal of loose cartilage. The microfracture technique was later developed by Richard Steadman and was carried out in patients with a posttraumatic cartilage defect. Tiny holes were drilled into the subchondral bone during microfracture surgery to allow blood and bone marrow to flow out and to create fibrous cartilage<sup>9,10</sup>. Microfracture showed good results in athletes treated for symptomatic lesions, though especially if they were younger than 40 years of age and have small lesions ( $<2\text{ cm}^2$ )<sup>10,11</sup>. Additionally, decrease in function is often seen

after initial improvement<sup>10-12</sup>. This decrease in function could be a predisposition to osteoarthritis<sup>12</sup>.

Mats Brittberg and Lars Peterson developed autologous chondrocyte implantation (ACI) especially for full thickness defects in knee cartilage, showing good results even for larger defects<sup>13</sup>. ACI is a technique which makes use of the patients' own cartilage to restore the defect. Cartilage slices are harvested during an arthroscopy, either from the defect rim or lesser weight bearing areas. The chondrocytes are isolated from these cartilage slices and cultured in the lab for a number of weeks until the number of chondrocytes is enough to implant in the defect. The implantation is carried out within an arthrotomy (open procedure), where the chondrocytes are placed back in the defect and covered with a membrane. These chondrocytes should form new, hyaline cartilage in the defect<sup>13</sup>.

After that, numerous techniques employing regenerative medicine for cartilage repair have been employed, most of them variations on the ACI technique. ACI shows better clinical outcome at short and long term follow-up compared with microfracturing, even for smaller defects<sup>14</sup>. More recently, new techniques have been developed using allogeneic mesenchymal stem cells in a one-stage cartilage repair which stimulates tissue regeneration<sup>15</sup>.

The treatment regime of a focal cartilage defect is mostly driven by the size of said defect<sup>16</sup>, where lesions larger than 2.5 cm<sup>2</sup> should be treated with sophisticated techniques<sup>17</sup>. Therefore, a proper assessment of the defect size is essential for a good outcome of the treatment.

### *Osteoarthritis*

Osteoarthritis (OA) is a degenerative whole-joint disease which mainly affects articular cartilage and is seen as the most common chronic condition of the joint. OA is a major cause of pain and disability in the elderly population and has a high burden on society. Though, no standard-of-care disease-modifying treatment is available for early stage OA. More and more knowledge is gained about various phenotypes of early OA and key challenges are to identify and target these specific phenotypes in treatment<sup>18,19</sup>.

Many knee OA patients eventually need a joint replacement (total knee arthroplasty, TKA), which is the standard treatment of end-stage OA. Almost 29.000 total knee arthroplasties were performed in the Netherlands alone in 2015<sup>20</sup>. Although, a total knee arthroplasty is not always the best option – patients younger than 55 years have a large lifetime risk for revision surgery compared to those 75 years or older (up to fivefold higher risk)<sup>21</sup>. Therefore, in relatively young patients with end-stage OA, a knee joint distraction is an alternative which showed non-inferiority in comparison

with TKA<sup>22</sup>. Five year follow-up of knee joint distraction showed prolonged clinical benefit as compared to natural progression of end-stage OA<sup>23</sup>.

### **Diagnosis – the conventional way**

The old fashioned way to diagnose knee issues are plain radiographs, used to evaluate malalignment and degenerative changes in the knee joints. In the case of OA, the Kellgren and Lawrence grading is commonly used to classify the severity of knee OA using five grades, ranging from 0 (no radiographic features of OA are present) to 4 (large osteophytes, marked joint space narrowing, severe sclerosis and definite bony deformity)<sup>24</sup>. However, using these radiographs have shown marginal clinical benefit in a population younger than 40 years<sup>25</sup>, a population in which cartilage defects can be treated properly. The main limitation of plain radiographs is that they do not visualize cartilage directly, since it can only detect joint space width (and narrowing of this width). Radiographs provide us a 2D projection image of the joint space, obscuring any spatial 3D information of the joint.

Magnetic Resonance Imaging (MRI) gives us a direct 3D visualization of articular cartilage, in contrast to radiographs. MRI provides us with possibilities to detect cartilage lesions earlier, proving a better window of opportunity for treatments. In addition, MRI can, among other things, visualize subchondral bone abnormalities, meniscal changes, the ligaments and intra-articular loose bodies. Cartilage defects can be measured by morphological MRI due to the high spatial resolution, which improves with the field strength<sup>26</sup>. MRI is not only applied in diagnosing cartilage defects and their size; several MRI semi-quantitative scoring systems are around to score knee OA, such as the Whole-Organ Magnetic Resonance Imaging Score (WORMS). WORMS includes cartilage signal and morphology, subchondral bone marrow abnormality, cysts, bone attrition and marginal osteophytes<sup>27</sup>. Another example is the Magnetic Resonance Observation of Cartilage Repair Tissue (MOCART), which semi-quantitatively evaluates cartilage after repair<sup>28</sup>. MRI provides us with an excellent structural analysis of cartilage. Though, when assessing cartilage damage, one would ideally have insight in the functional properties of cartilage, which is lacking in conventional MRI.

### **Biochemical MRI**

Sophisticated techniques are necessary to accurately quantify cartilage defects, especially those of the lower ICRS grades, to gain insight what actually happens inside the cartilage before large structural defects occur. Same goes for the occurrence of OA: biochemical changes precede the actual changes in morphology (i.e. thinning or defects), which are often missed on conventional diagnostic modalities. Quantitative biochemical MRI can quantify these intricate changes in tissue content. One could

apply one or a combination of these techniques in the diagnosis of cartilage defects, in treatment planning or treatment follow-up. These techniques could especially be helpful in diagnosis, since evidence shows that the cartilage lesion size is heavily underestimated by standard MRI measurements, on average up to 70% of the expected size<sup>29,30</sup>. As we know that cartilage treatment is driven by defect size, quantitative biochemical MRI could make a substantial difference.

Quantitative biochemical MRI techniques can focus on all the compartments of cartilage, but often the most attention goes to quantification of GAG content. The first and most established technique to quantify GAGs in articular cartilage is delayed gadolinium enhanced MRI (dGEMRIC) by using an ionic contrast agent. The tissue content of this contrast agent is inversely proportional to the GAG content and this can be quantified by the change in T1 relaxation time<sup>31</sup>. Measurements of cartilage quality by means of dGEMRIC have been successfully applied in cartilage repair patients<sup>32,33</sup>, in patients undergoing high tibial osteotomy and knee joint distraction<sup>34</sup> and (early) OA patients<sup>35,36</sup>. A non-contrast alternative to dGEMRIC is T1rho, using the time constant T1rho: spin lattice relaxation time in the rotating frame, quantifying the interactions between motion-restricted water molecules with their local macromolecular environment. It has been shown that suspected OA patients present with elevated T1rho relaxation times even if their radiographs did not indicate OA<sup>37</sup>. T1rho also has been applied within cartilage repair patients, showing potential for a quantitative and non-invasive monitoring of regenerated tissue<sup>38</sup>. Though, evidence in a study of van Tiel and colleagues shows that T1rho might not only relate to the GAGs in articular cartilage, whereas it could also be related to the collagen content<sup>39</sup>.

Therefore, a more direct method to quantify the GAG content is necessary. Other metabolites besides protons can be used to quantify the GAG content, for instance by sodium MRI. The sodium content has a direct relation with GAG content<sup>40,41</sup>. GAGs are negatively charged due to the sulphate and carboxyl side-groups, which attract positively charged ions such as sodium to ensure the electroneutrality of cartilage<sup>4</sup>. The sodium concentration is directly related to the GAG concentration, because of the fixed charge density (FCD)<sup>42</sup>. Preliminary studies employing sodium MRI have shown its potential in OA and focal cartilage defects<sup>43,44</sup>. This assessment can be improved when more sophisticated sodium MRI methods are used, such as a fluid inversion recovery preparation pulse<sup>45</sup> or an interleaved acquisition with proton<sup>46</sup>, which will benefit the quantification of sodium.

In contrast to these assessments of GAG, Chemical Exchange Saturation Transfer (CEST) directly quantifies GAG content based on the chemical exchange of its labile hydroxyl (-OH) protons with the bulk water<sup>44,47,48</sup>. These exchangeable protons resonate at a different frequency compared with bulk water protons and are saturated

via selective radio frequency (RF) irradiation. Because of the exchange, the saturation is transferred to the bulk water pool, which ultimately results in large contrast enhancement factors <sup>47,49–51</sup>. The quantification of GAG in articular cartilage with the use of CEST, i.e. gagCEST, has a high potential for the examination of cartilage degeneration and hence diagnosis of early-stage OA.

Cartilage imaging studies often focus on GAG content, but collagen and water content are just as important when characterizing cartilage quality. Most of these studies focus on T2(\*) relaxation time mapping, but some studies focused on diffusion MRI as a direct measurement of the collagen network. The apparent diffusion coefficient (ADC) shows to be dependent mainly on proteoglycan (PG) content, whereas the fractional anisotropy (FA) is correlated with the collagen architecture <sup>52</sup>. Early stage cartilage damage results in a loss of PG, namely glycosaminoglycans, at the surface of the cartilage<sup>53</sup>. This is reflected in an increase in ADC <sup>54</sup>, which is also shown in *in vitro* studies with PG extraction <sup>55,56</sup>. The same change in ADC has been shown in osteoarthritic cartilage, which is also accompanied with a lower FA in the deep zone of the cartilage <sup>57</sup>. Diffusion MRI could also be helpful as a follow-up measurement after cartilage therapies, because repair cartilage shows a higher ADC directly after repair <sup>58–60</sup>.

T2 mapping and T2\* mapping can assess different components of the cartilage, mainly the water content and the collagen architecture (especially the orientation of the collagen fibers). T2\* relaxation visualizes the combination of spin-spin relaxation (T2) and magnetic field inhomogeneities (T2'). Since T2\* imaging can be employed with a high resolution, the highly curvatuuous cartilage and the zonal variation within the cartilage could in theory be visualized. T2\* mapping has been successfully applied within a number of joints in the human body, such as the hip<sup>61,62</sup>, knee <sup>63,64</sup> and ankle <sup>65,66</sup>.

### Aims & outline thesis

This thesis aims to evaluate a number of MRI methods to quantify the quality of articular cartilage. Within this thesis, we implemented two methods for GAG quantification (sodium MRI and gagCEST) and one method for the quantification of the collagen network (T2\* mapping) giving complementary information on the quality of cartilage. We present a number of techniques in various stages of development, as well as technical developments in MRI acquisition in the form of a double tuned knee coil. This 1H/23Na coil is presented in **chapter 2**, showing the feasibility and comparison with the best available (proton) coil on the market.

When bringing new imaging techniques to the market, one has to go through a number of validation phases, from ex vivo imaging to in vivo feasibility and validation



studies. These stages of development are set out in this thesis, starting with **chapter 3**, where sodium MRI is tested in a number of total knee replacement samples to test whether sodium MRI could be a proxy for cartilage stiffness. **Chapter 4** focuses on imaging of larger ex vivo samples, in this case carpal joints of Shetland ponies. These have been used in an extensive OA model, where two different groove types were used to artificially induce OA.

**Chapter 5** describes the first in vivo study carried out with gagCEST MRI in our hospital, where we tested the technical feasibility of this protocol in cartilage repair patients and healthy volunteers. **Chapter 6** takes this work to the next level, by validating in vivo results in patients with biochemical testing in the lab as well as electromechanical testing.

The final chapter of this thesis, **Chapter 7**, summarizes the major findings of each chapter and discusses the clinical implications.

[illegible]

# Uncompromised MRI of knee cartilage while incorporating sensitive sodium MRI

S. Brinkhof<sup>1</sup>, A.A. Haghejad<sup>2</sup>, K. Ito<sup>3,4</sup>, K. Markenroth Bloch<sup>5</sup>, D.W.J. Klomp<sup>1</sup>

1. Department of Radiology, University Medical Center Utrecht, Utrecht, Netherlands
2. Wavetronica, Netherlands
3. Department of Orthopaedics, University Medical Center Utrecht, Utrecht, Netherlands
4. Orthopaedic Biomechanics, Department of Biomedical Engineering, Eindhoven University of Technology, Eindhoven, Netherlands
5. Lund University BioImaging Center, Lund, Sweden

**NMR in Biomedicine ; 31(11), 2019, e4173**

## Abbreviations

FCD	fixed charge density
GAG	glycosaminoglycans
gagCEST	glycosaminoglycan Chemical Exchange Saturation Transfer
SNR	signal-to-noise ratio

## Abstract

Sodium imaging is able to assess changes in ion content, linked to glycosaminoglycan content, which is important to guide orthopaedic procedures such as articular cartilage repair. Sodium imaging is ideally performed using double tuned RF coils, to combine high resolution morphological imaging with biochemical information from sodium imaging to assess ion content. The proton image quality of such coils is often harshly degraded, with up to 50% of SNR or severe acceleration loss as compared to single tuned coils. Reasons are that the number of proton receive channels often severely reduced and double tuning will degrade the intrinsic sensitivity of the RF coil on at least one of the nuclei. However, the aim of this work was to implement a double-tuned sodium/proton knee coil setup without deterioration of the proton signal whilst being able to achieve acquisition of high SNR sodium images.

A double-tuned knee coil was constructed as a shielded birdcage optimized for sodium and compromised for proton. To exclude any compromise, the proton part of the birdcage is used for transmit only and interfaced to RF amplifiers that can fully mitigate the reduced efficiency. In addition, a 15 channel single tuned proton receiver coil was embedded within the double-resonant birdcage to maintain optimal SNR and acceleration for proton imaging. To validate the efficiency of our coil, the designed coil was compared with the state-of-the-art single-tuned alternative at 7T. B1+ corrected SNR maps were used to compare both coils on proton performance and g-factor maps were used to compare both coils on acceleration possibilities. The newly constructed double-tuned coil was shown to have comparable proton quality and acceleration possibilities to the single-tuned alternative while also being able to acquire high SNR sodium images.

## Introduction

Osteoarthritis (OA) is a degenerative whole-joint disease which is a large burden on society. Patients with OA suffer from joint stiffness, reduced range of motion of the joints and often pain. The cause of these symptoms is cartilage degeneration, characterized by loss of glycosaminoglycans (GAG) and alterations to the collagen fiber network. The loss of GAG content leads to softening of articular cartilage and therefore a reduced ability to withstand loading and wear of the joint<sup>67,68</sup>. Early detection of cartilage damage is vital for treatment planning to prevent or decelerate irreversible damage to the joint. The treatment planning is often hampered by insufficient information from standard-of-care MRI, because the lesion size can be underestimated by 60 to 70%<sup>29,30</sup>. Assessment of early cartilage damage by biochemical MRI can improve this treatment planning. Current MRI methods can quantify the morphology of the joint, but biochemical changes in the joint often occur before morphological changes appear. This gives rise to the need for biochemical and quantitative MRI to capture these intricate changes in the biochemical composition of articular cartilage.

Examples of such biochemical MRI methods include T2 mapping<sup>64,69,70</sup>, T1ρ mapping<sup>39,71</sup>, delayed gadolinium enhanced MRI of cartilage (dGEMRIC)<sup>72,73</sup>, glycosaminoglycan chemical exchange saturation transfer (gagCEST)<sup>48,74,75</sup> and sodium imaging<sup>44,45,76</sup>, each probing one or more characteristics of articular cartilage. These techniques result in quantitative biomarkers which reflect the biochemical composition of articular cartilage and can assess early cartilage damage. Insight in cartilage damage is vital in diagnosis of cartilage repair, but also as a tool to realize optimal treatment planning. Understanding cartilage biology and damage can also help the follow-up of treatment of OA patients and be a powerful research tool to assess new treatment paradigms.

One of the signs of early cartilage damage is ion misbalance and its related loss of GAG content and its related ion misbalance, starting on the surface of the cartilage. GagCEST MRI can capture these changes in GAG content at a high resolution, but gagCEST MRI comes with a few drawbacks. These sequences are strongly dependent on a homogenous B<sub>0</sub> field, on the exchange rate and successful gagCEST at 7T is not that easily translated to conventional clinical field strengths like 1.5T and 3T since the GAG resonance is close to the water frequency which is difficult to disentangle at these clinical field strengths. The GAG loss can also be quantified by using sodium MRI due to its direct relation with GAG content<sup>40,41</sup>. Since GAG is negatively charged due to its sulphate and carboxyl groups it will attract positively charged ions, mainly in the form of sodium, to preserve the electroneutrality<sup>4</sup>. The sodium concentration is proportional to the GAG concentration, because of the fixed charge density (FCD)<sup>42</sup>.

Thus, sodium imaging is able to assess the GAG content and evaluate changes in the GAG content. Moreover, the FCD is a well-established (*ex-vivo*) biomarker for OA so an imaging strategy that links more directly to FCD simplifies translation to clinical use.

However, sodium imaging intrinsically suffers from a low signal-to-noise ratio (SNR) because of its lower gyromagnetic ratio<sup>77,78</sup>. Nonetheless, the sodium concentration is similar to GAG and in contrast to gagCEST provides positive contrast and practically no background signal. Moreover, higher field MR scanners provide larger SNR, and it is therefore appealing to use 7T MR for sodium imaging. Sodium imaging is ideally employed using double tuned RF coils, but the proton image quality of such coils is often severely compromised, even up to 30% of SNR loss in severe cases<sup>79–81</sup>. Reasons for this is that the number of proton receive channels are often reduced as compared to single tuned coils, and that double tuning will degrade the intrinsic sensitivity of the RF coil. However, when incorporating an array of single tuned <sup>1</sup>H receive coils inside a volume sodium transceiver, proton imaging performance may remain intact. Integrating a receive array not only facilitates the possibility for B<sub>0</sub> shimming and the ability to provide co-registered anatomical images, it can still facilitate all of the above mentioned MRI techniques potentially without compromises. Additionally, acceleration with the array is warranted to maintain acceptable overall scan time.

Due to the comprised MRI performance, sodium MRI is often not considered for clinical diagnoses. Though, there is a great interest in sodium imaging in research which is moving towards the clinic in various fields, such as orthopaedics<sup>41</sup>, neurology<sup>82,83</sup> and breast imaging<sup>84</sup>. In order to add sodium MRI for clinical use, one has to make sure that the quality of proton MRI is up to par with the best available coils. Therefore, for this study a dual tuned sodium-proton coil as transceiver for sodium and transmitter for hydrogen with a high-density proton receive array was designed. The setup was tested for the proton imaging performance in healthy volunteers and compared with a state-of-the-art single tuned knee coil. The aim of this work is to demonstrate that this new double tuned coil configuration besides <sup>23</sup>Na information also gives proton images with image quality comparable to commercially available single-tuned coils.

## Methods

### Coil design

A double-tuned knee coil was constructed as a double-resonant four-ring shielded birdcage (12 rods with a length of 15 cm) and 15 channel proton receiver coil embedded within the double-resonant birdcage<sup>85</sup>. The <sup>1</sup>H transmit and receive coils could be actively detuned using standard PIN diode circuitry based on activating

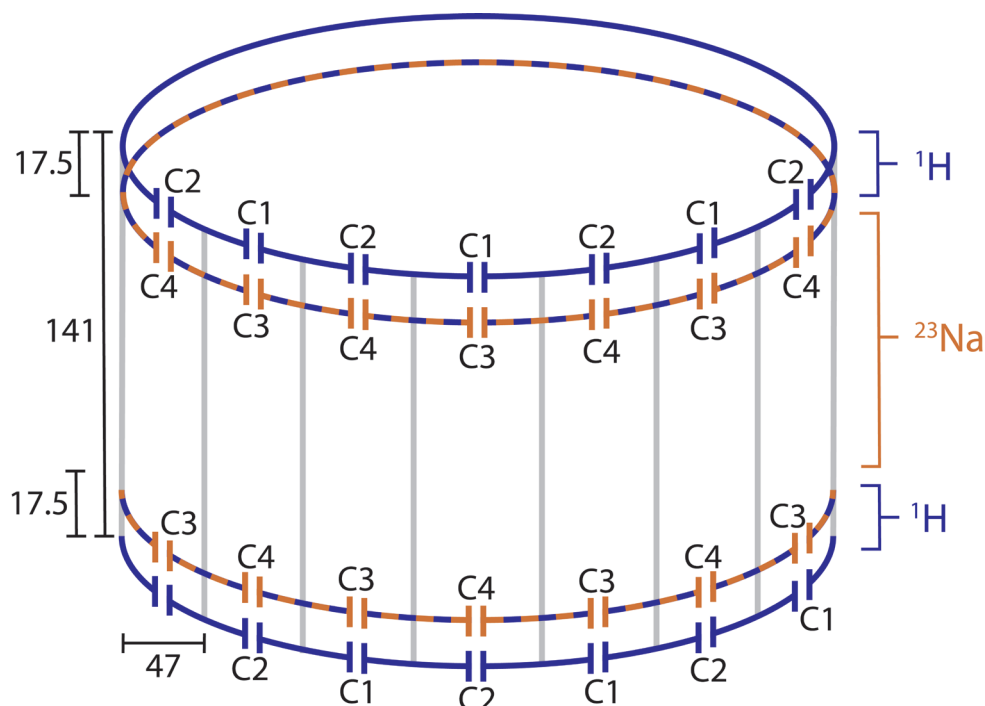


**Figure 1: Coil configuration, showing the double-tuned four-ring birdcage. The dimensions are in millimeters. The following capacitor values are used:  $C1 = 5.6 + 2 \text{ pF}$ ,  $C2 = 5.6 + 2.4 \text{ pF}$ ,  $C3 = 91 \text{ pF}$  and  $C4 = 91 + 8.2 \text{ pF}$ .**

a parallel resonant inductor over a tuning capacitor. The fifteen overlapping proton receive elements were each 5 cm width and 9.5 cm in length and connected to low impedance preamplifiers used for preamplifier decoupling and signal amplification before interfacing to the 7T MRI system. The double tuned coil is optimized for the sodium frequency by using a tank circuit tuned for tuning the  $^1\text{H}$  frequency and maintaining the natural inductance in the endring as observed for the impedance at the  $^{23}\text{Na}$  frequency. Due to the intrinsically high impedance of the  $^1\text{H}$  coil on the  $^{23}\text{Na}$  frequency no sodium trap is inserted on the array. A graphical representation of the coil configuration is shown in figure 1.

To validate the efficiency of the proton coil, our double tuned coil was compared with a vendor-built single tuned alternative (birdcage transmit and 28 channel receive; Quality Electrodynamics LLC, Ohio, USA).

## MR methods

MRI experiments were carried out on a 7.0 Tesla whole body scanner (Achieva; Philips



Healthcare, Best, Netherlands) and all experiments were performed with the double tuned coil and single tuned coil in separate imaging sessions. SNR maps were carried out by making a dynamic noise scan where the first dynamic is used to acquire the image, while the second dynamic is used to acquire noise only with the same scan parameters (no RF or gradients are used for the second dynamic, while signal combinations from coil elements in reconstruction is copied from the first dynamic). The following parameters were used: transversal, multi-slice fast field echo (FFE) with a Cartesian readout; TE = 1.95; TR = 199; flip angle = 10 degrees; field of view (FOV), 200 x 200 x 100 mm<sup>3</sup>; voxel size, 2 x 2 x 2 mm<sup>3</sup>. The B1+ map was acquired using a dual TR protocol with the following parameters: transversal, multi-slice FFE with a Cartesian readout; TE = 1.0; TR = 40; TR extension = 160; flip angle = 50 degrees; FOV, 170 x 170 x 100 mm<sup>3</sup>; voxel size, 4 x 4 x 4 mm<sup>3</sup>.

For this purpose, sixteen healthy volunteers were included after explaining the study procedures and informed consent was signed. Eight of the volunteers were examined with the single tuned coil, and the other eight with the double tuned coil. For consistency, the right knee was imaged in all healthy volunteers. In each volunteer, SNR maps and B1+ maps were acquired. In addition, for one volunteer per coil a set of g-factor maps were calculated. Finally, sodium images were acquired in four of the volunteers scanned with the double tuned coil. Scan parameters for the sodium protocol were chosen as follows: sagittal, three dimensional FFE with a cartesian readout; TE = 1.61 ms; TR = 100 ms; flip angle = 130 degrees (which was optimized via a flip angle series); FOV, 150 x 150 x 150 mm<sup>3</sup>; voxel size, 3 x 3 x 3 mm<sup>3</sup>; 5 signal averages; total acquisition time of 7 minutes and 45 seconds.

## Data analysis

Geometry factor (g-factor) maps were reconstructed on the scanner using reconstruction software available on the Philips system (delayed reconstruction). A total of nine g-factor maps was reconstructed, with SENSE accelerations in anterior-posterior (AP) and right-left (RL) to a maximum of three in both directions. The g-factor maps were reconstructed for both coils to assess differences in acceleration possibilities.

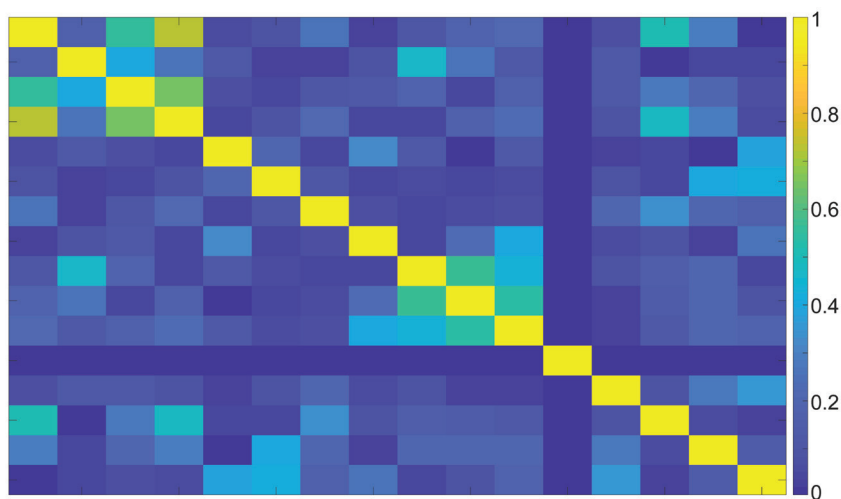
Noise scans were used to reconstruct SNR maps and B1+ maps were created by using a dual TR approach. Noise scans were carried out with same scan and reconstruction (i.e. same weighting between coil elements) parameters as the signal scan, but with RF and gradients off. The noise standard deviation is approximated by 0.8 times the mean noise, since the noise is a Rayleigh distribution<sup>86</sup>. Dividing the signal by this noise standard deviation results in a SNR map. Considering scans are obtained in the regime that SNR is linearly related to the (low) flip angle, this SNR map is normalized

for actual used flip angle using the B1+ maps to translate the SNR maps to sensitivity maps and properly assess differences between the double tuned and single tuned coil. Regions of interest (ROI) were drawn in the trochlear cartilage to compare the SNR performance between both coils.

Sodium signal intensity was converted to sodium concentration making use of a calibration curve. Four phantoms filled with known sodium concentrations (75, 150, 225 and 300 mM) were placed on the side of the knee and measured together with the volunteers. These four sodium concentrations were used to create a linear calibration curve, which was consequently used to correct the sodium signal intensity to sodium concentration. The sodium concentration map was corrected for the assumed 75% of water content<sup>4</sup>.

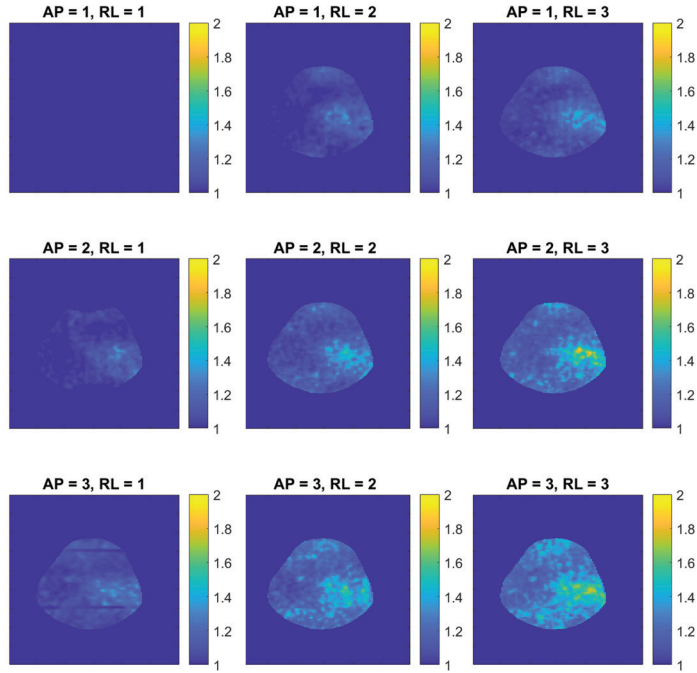
## Results

Figure 2 shows the noise correlation between the  $^1\text{H}$  receiver elements. Moreover, a low (maximum -19.0 dB, average -30.7 dB) RF coupling between the  $^{23}\text{Na}$  transceiver coil and  $^1\text{H}$  receivers was measured at the  $^{23}\text{Na}$  frequency, which confirms that the  $^1\text{H}$  receivers are invisible for the  $^{23}\text{Na}$  transceiver.



**Figure 2: Noise correlation matrix of the double-tuned coil. A small amount of coupling can be observed between channel 1 and 4, and 1 and 3.**

Figure 3 shows the axial g-factor maps of our double tuned coil, which indicated that a SENSE acceleration of 9 was feasible in this coil when accepting a factor of 2 enhanced noise (AP = 3, RL = 3, maximum g-factor 1.9). Figure 4 shows the same axial g-factor maps, acquired with the single tuned coil where the g-factor maps had a similar hotspot at SENSE acceleration of 9, with a maximum g-factor of 2.2.



**Figure 3: Axial g-factor maps of double tuned coil, with SENSE acceleration factors up to 3 in both directions.**

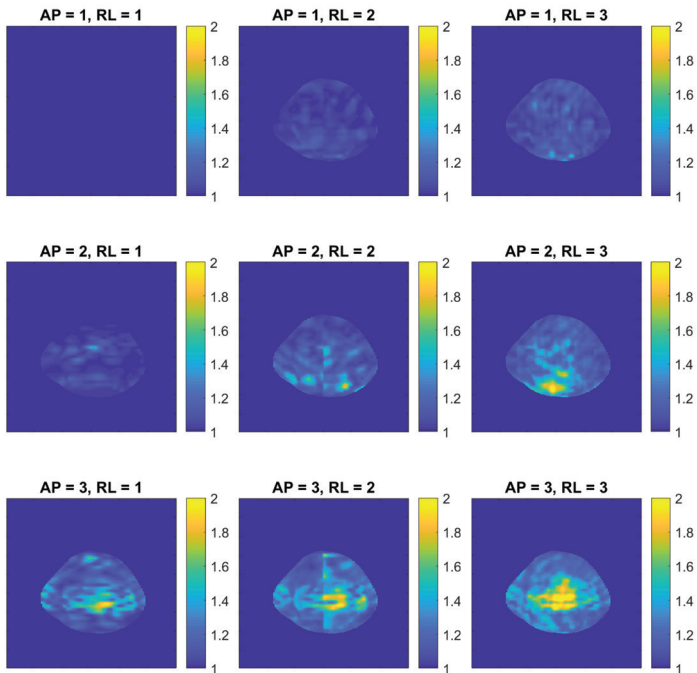


**Figure 4: Axial g-factor maps of the single tuned coil, with SENSE acceleration factors up to 3 in both directions.**

Figure 5 shows a typical axial and sagittal slice for each coil with corresponding g-factor maps (with SENSE AP = 3, RL = 3). The g-factor maps were acquired in axial slices on the same height as SNR maps in figure 5, with patella and femur visible on the slice. SNR maps are shown in figure 6 for our double tuned coil and the single tuned coil, indicating that both had similar SNR. The SNR maps were corrected for B1+ performance, hence reflecting intrinsic coil sensitivity. Table 1 shows the SNR values of both coils for all volunteers. Average SNR in the trochlear cartilage was 29.87 in the double tuned coil (standard deviation = 4.60) and 28.3 in the single tuned coil (standard deviation 1.61). The difference in B1+ efficiency between the two setups was on average 10% in favor of the single tuned coil, which was well within the limits of the RF amplifier (i.e. 2 x 4kW).

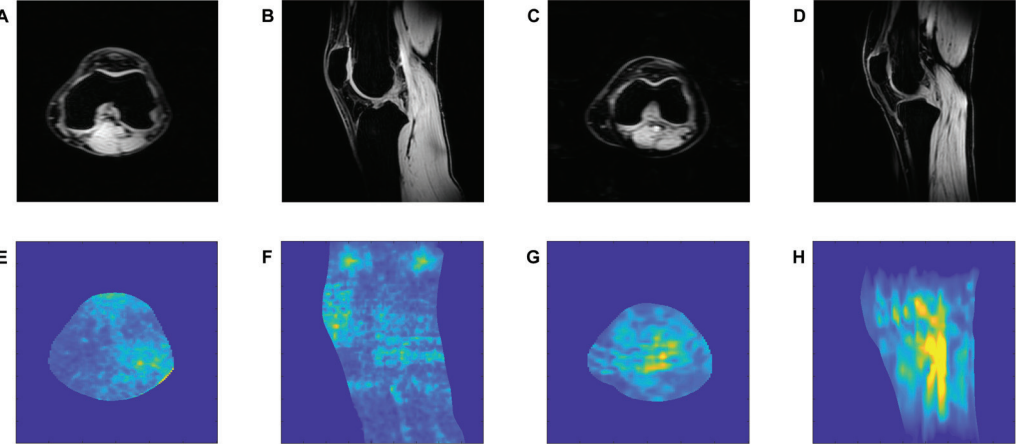


**Figure 5: Axial (A) and sagittal (B) image slices for double tuned coil with corresponding g-factor maps (E & F), and axial (C) and sagittal (D) image slices for single tuned coil with corresponding g-factor maps (G & H).**

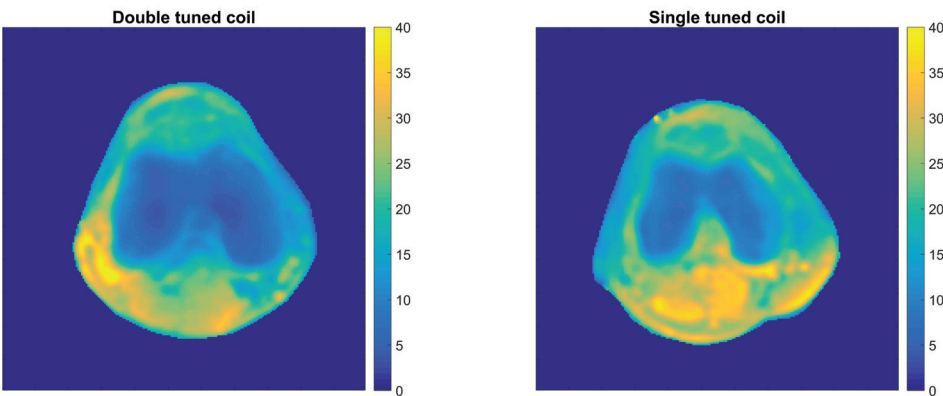


**Figure 6: SNR maps of double tuned coil (left) and single tuned coil (right).**

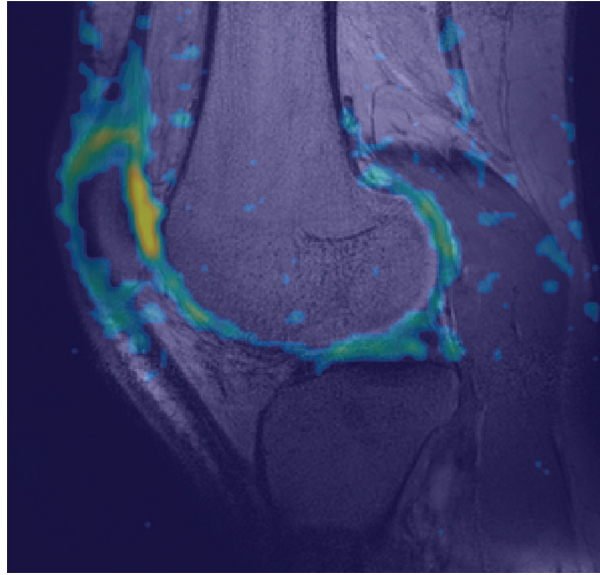


**Figure 7: Sodium image overlaid on proton density weighed anatomical scan**

Figure 7 shows a sodium scan from the double tuned coil overlaid on a proton density weighed anatomical scan. Cartilage sodium values are in line what has been reported in literature (around 250 mM in healthy cartilage tissue<sup>41,45</sup>).

**Table 1: Overview of SNR values in the trochlear cartilage in both coils.**

Volunteer	Double tuned coil		Single tuned coil	
	Mean	Standard deviation	Mean	Standard deviation
1	32.80	0.68	24.60	0.88
2	27.63	1.89	29.03	0.98
3	23.04	0.81	27.09	1.73
4	33.07	1.61	29.28	2.00
5	39.03	1.81	29.73	1.87
6	28.34	2.40	29.25	0.76
7	28.50	1.40	29.32	1.78
8	26.60	1.34	28.24	1.94
Average	29.88	4.60	28.32	1.61

## Discussion

This work presents a double tuned coil optimized for knee imaging with similar SNR and acceleration performance for  $^1\text{H}$  as the state-of-the-art single tuned alternative, because of the combined implementation of local  $^1\text{H}$  receive coils with an optimized volume sodium coil. The double tuned coil can produce proton images with high

## Chapter 2

sensitivity and acceleration possibilities, combined with a high SNR sodium map to assess the glycosaminoglycan content in the articular cartilage in the knee. Acquiring proton scans and sodium scans in the same session, without repositioning the patient, gives high-resolution anatomical images co-registered with sodium scans for excellent morphological reference.

The double tuned coil is built as a double-resonant shielded birdcage with 15 channel proton receive coil embedded within the birdcage. Relatively long receive elements were used within this design to maximize the tissue loss dominance and thereby of the sensitivity of the receive field. This design has no multiple elements in the Z direction, and therefore sacrifices acceleration possibilities in this direction.

This double-resonant birdcage has a lower efficiency compared to a single-tuned alternative. Since the diameter is relatively small in comparison to for instance a head coil, there is enough power available to compensate for the reduced efficiency. Moreover it should be noted that the efficiency reduction is only 10% in contrast to the 50% of some earlier work, which can be because the commercial birdcage coil did not needed to be designed for highest efficiency due to the presence of the high sensitivity receiver array. In our setup, the birdcage had to be efficient for it was used for sodium detection as well.

A quadrature sodium transceiver coil is preferred over a setup with multiple elements, because the intrinsic SNR in the center will be similar. A sodium array might be advantageous when higher SNR is needed at the periphery. In addition, any acceleration is not relevant, because T1 of sodium is very short and a fair number of signal averages is already needed to achieve reasonable SNR. Lastly, the T1 of sodium is very short, leading to a high spatial encoding speed. Therefore, a quadrature sodium transceiver coil will be the optimal setup.

To use the proton coil for superb MRI in the same scanning session, one has to be sure that it delivers similar image quality as a state-of-the-art standard single-tuned proton coil. Within this work, we chose to compare our coil to the state-of-the-art single tuned coil available for 7T, with the comparison based on the SNR maps and acceleration possibilities. Eight volunteers were included and scanned with the double tuned coil and another eight volunteers scanned with the single tuned coil. Ideally, the same eight volunteers would have been scanned with both coils, but this was logistically impractical. However, the low variation in SNR between individuals (Table 1) indicates that using the same volunteers in both coils would not have altered our results.

The g-factor maps of the double tuned coil showed the same acceleration possibilities as the single tuned coil. Both coils lost some performance with acceleration factor of

9 (AP = 3, RL=3, g-factor  $\sim 2$ ). The patterns within the g-factor maps showed some differences, which could be attributed to the differences in receive array designs. We opted for long receive elements within our coil, giving a higher tissue load dominance, though, a more diffuse hotspot pattern can be observed. The array in the single tuned coil has smaller loops, which give higher SNR on the surface but lowering the SNR in the middle of the coil. The design of the single tuned coil leads to the typical 'aliasing' artefacts in the g-factor maps as shown in the bottom right in figure 2.

Often, dual tuned coils severely lose SNR on the proton side because optimal sensitivity is desired on the X-nucleus side, in this case sodium. The sodium transmit efficiency is not compromised, because the coil has been optimized for sodium imaging. The loss of SNR at the proton frequency is often in the range of 20 to 30%<sup>80,81</sup>, but can account to over 50% of SNR loss in severe cases<sup>79</sup>. In our work, the SNR maps did not show substantial differences, indicating that the proton performance was not hampered by the addition of a sodium transmit/receive coil. Both coils produce an average B1+ corrected proton SNR of roughly 28 which was shown in eight volunteers per coil. The addition of a sodium transmit/receive coil gives the possibility to acquire high SNR sodium scans in the same session as the proton scans, without changing coils. By implementing an interleaved scanning protocol, sodium and proton scans can be acquired at the same time to be even more time efficient<sup>46</sup>.

Implementing a sodium protocol gives information on the condition of the joint. One of the potential clinical application lies in FCD maps, which can be a proxy for early stage cartilage damage. The sodium concentration map can be converted to the fixed charge density by using the ideal Donnan equilibrium equation<sup>42</sup>.

GAG content can also be visualized by employing a gagCEST imaging protocol, as shown in earlier work<sup>74</sup>. While the gagCEST signal can be contaminated by signals originating from other compounds or influenced by system imperfections, it can now be obtained in the same scan session as sodium; benefiting from both modalities. The sodium MRI will be more specific but is hindered by lower spatial resolution, and the higher resolution of gagCEST can reveal heterogeneities in more detail.

In conclusion, a double tuned coil was implemented with comparable proton image quality to the state-of-the-art single tuned alternative, while also being able to acquire high SNR sodium images.



[illegible]



# Can sodium MRI be used as a method for mapping of cartilage stiffness?

S. Brinkhof<sup>1</sup>, M. Froeling<sup>1</sup>, R.P.A. Janssen<sup>2,3,4</sup>, K. Ito<sup>4,5</sup>, D.W.J. Klomp<sup>1</sup>

1. Department of Radiology, University Medical Center Utrecht, Utrecht, Netherlands
2. Department of Orthopaedic Surgery and Trauma, Maxima Medisch Centrum, Eindhoven, Netherlands
3. Fontys University of Applied Sciences, Eindhoven, Netherlands
4. Orthopaedic Biomechanics, Department of Biomedical Engineering, Eindhoven University of Technology, Eindhoven, Netherlands
5. Department of Orthopaedics, University Medical Center Utrecht, Utrecht, Netherlands



## Abstract

### Introduction

Sodium concentration is responsible for (at least part of) the stiffness of the articular cartilage due to the osmotic pressure it generates. Therefore, we hypothesized that we could use sodium MRI to approximate the stiffness of cartilage to assess its functionality in early cartilage degeneration.

### Methods

Four human tibial plateaus were retrieved from patients undergoing TKA, and their cartilage stiffness mapped with indentation testing, after which the samples were scanned in a 7T MRI to determine sodium concentration. Cartilage samples were prepared from the indentation locations and the GAG content (per wet weight) quantified by means of a dimethylmethylene blue assay (DMMB). The relation of biomechanical parameters to MRI sodium and GAG concentration were explored by means of a linear mixed model.

### Results

Weak correlations of GAG concentration with apparent peak modulus ( $p = 0.0057$ ) and apparent equilibrium modulus ( $p = 0.0181$ ) were observed and a lack of correlation of GAG concentration versus MRI sodium concentration was observed. MRI sodium concentration was not correlated with apparent peak modulus, though a moderate correlation of MRI sodium concentration with permeability was shown ( $p = 0.0014$ ).

### Discussion and conclusion

Although there was a correlation between GAG concentration and cartilage stiffness, this was also not similar with sodium concentration as measured by MRI. Thus, if the correlation between MRI sodium imaging and GAG concentration could be resolved, this strategy for assessing cartilage functional quality still holds promise.

## Introduction

Focal cartilage defects are often treated with regenerative medicine therapies, because the body cannot heal these defects itself due to the sparsely distributed chondrocytes throughout the articular cartilage and its avascular nature. Patients with focal cartilage defects suffer from pain and functional impairment, which significantly affects their quality of life <sup>7</sup>. Early identification of these focal cartilage defects is important, since it improves the prognosis and outcome of treatment <sup>1,87</sup>. Arthroscopy has shown to be an excellent method to analyze articular cartilage, especially the discrimination between healthy cartilage and early degenerated cartilage <sup>88</sup>. This early stage cartilage damage is reflected in softness of the cartilage under indentation during arthroscopy <sup>8</sup>. Softer cartilage damages faster, since it cannot resist loading as well as healthy cartilage. Although arthroscopy is an excellent method for evaluating cartilage damage, an arthroscopy is still an invasive method to actually measure cartilage quality. Ideally, one would assess the stiffness of cartilage non-invasively, for instance with MRI, because the extent of cartilage damage is most helpful for treatment planning rather than changing treatment strategy intra-operatively.

Cartilage gains its stiffness amongst others due to its ability to retain fluid and swell, both as a result of its osmotic potential<sup>89</sup>. This Donnan osmotic potential arises due to an imbalance of ion concentration between the external sodium concentration (i.e. in the synovial fluid) and the internal tissue sodium concentration. Due to this osmotic potential, and a restriction for swelling and inflow of water by its collagen network, a hydraulic pressure is maintained in the tissue. The imbalance in sodium concentration is a result of the negative fixed charges on the plentiful glycosaminoglycans (GAGs) in cartilage extracellular matrix. These GAGs are bound to a protein backbone forming a proteoglycan which in turn is aggregated to a hyaluronic acid backbone forming a molecule 100's of millions of daltons in molecular weight. These PG-aggregates in turn are immobilized by being bound to and entangled in the collagen network of the cartilage extracellular matrix and form the ground substance of cartilage with an extremely low permeability to interstitial fluid flow. Thus, when the cartilage is compressed, the resisting stiffness, both immediate and after some time when deformation has become constant, i.e. at equilibrium, are due to the concentration of the GAGs and their fixed charge density (FCD). As electroneutrality is always maintained in the tissue, this FCD would also be reflected in the intratissue sodium concentration making sodium MRI a possible method to measure the stiffness of cartilage *in vivo*.

Sodium MRI has been able to show accurate measurements of the FCD *in vivo* in humans<sup>42</sup>. Sodium measurements in the patellae of healthy volunteers showed an average sodium concentration of 254 mM<sup>4</sup>. When using an inversion recovery pulse for

fluid suppression similar sodium concentrations have been shown in healthy cartilage ( $249 \text{ mM} \pm 45 \text{ mM}$ )<sup>45</sup>. The same range of sodium concentrations was observed in a comparative study in subjects without ( $220\text{-}270 \text{ mM}$ ) and with osteoarthritis ( $170\text{-}200 \text{ mM}$ )<sup>90</sup>.

Given the fact that the sodium concentration is responsible for (at least part of) the stiffness of the articular cartilage and sodium MRI is a proven method for assessment of FCD, we hypothesized that we could extend the usability of sodium MRI to approximate the stiffness of the cartilage to gain insight in early cartilage damage. For that purpose, tibial plateaus were tested for their compressive stiffness by means of a stress-relaxation test using an indenter mimicking an arthroscopic probe and consequently scanned *ex vivo* with sodium MRI on a 7T MRI, to assess whether those two parameters (stiffness and sodium concentration) are related to each other.

## Methods

Four tibial plateaus of women (age range 59 to 70) undergoing total knee replacement (TKR) were retrieved after their surgery and frozen at  $-20$  degrees Celsius. The use of these human donor tissues has been determined by the Medical Ethical Committee Maxima Medisch Centrum to not be subject to the guidelines of the Medical Research Involving Human Subjects Acts (WMO), and have been approved by the institutional review board under METC N16.148. The tibial plateaus were thawed to room temperature before the testing procedures began. The testing procedures were carried out as follows: indentation tests were carried out in a tensile tester (Criterion; MTS, Eden Prairie, USA), after which the samples were scanned in a 7T MRI scanner (Achieva; Philips Healthcare, Best, Netherlands). Samples were transported to the lab afterwards to quantify the GAG content by means of a dimethylmethylene blue assay (DMMB).

### Stress-relaxation tests

Stress-relaxation tests were carried out with a 50 N load cell on each individual plateau. The plateaus were submerged in room temperature phosphate-buffered saline (PBS) in a ceramic container. A stainless steel hemi-spherical tip indenter with a diameter of 2 mm was used, since the objective was to mimic the stiffness which the surgeon feels with an arthroscopic probe during surgery. The indentation protocol started with a deformation rate of  $50 \mu\text{m/s}$  until  $0.1\text{N}$  was reached to ensure tissue contact. After tissue contact, the indenter was advanced another 0.3 mm into the cartilage at  $0.5 \text{ mm/s}$  and then its position was maintained for 240 seconds to reach equilibrium.

The stiffness was mapped over the whole tibial plateau (on parts which were covered

with cartilage, parts with complete denudation were excluded). The spatial indentation measurements were at least 5 mm apart to ensure that there was no overlap in measurement areas. Each indentation location was marked with a waterproof marker and photographed to ensure proper location matching in the post-processing.

### MR imaging

The tibial plateaus were placed into a custom-made container (outer casing of polyvinyl chloride (PVC), inner sample holder of polyoxymethylene (POM), dimensions 8.5 by 8.5 by 16 cm) which made it possible to image all tibial plateaus at the same time. The plateaus were submerged in Galden PFPE (perfluoropolyether – MR inert fluid) to ensure no background signal was present while imaging the samples.

These samples were placed into a double tuned proton/sodium coil to acquire sodium images which was built in-house<sup>91</sup>. These sodium images were acquired with a 3D FFE with a cartesian readout; TE = 1.61 ms; TR = 100 ms; flip angle = 140 degrees (which was optimized via a flip angle series); FOV, 120 x 120 x 150 mm<sup>3</sup>; voxel size, 3 x 3 x 3 mm<sup>3</sup>; 25 signal averages; total acquisition time of 17 minutes and 34 seconds. Three phantoms containing a known sodium concentration (75, 225 and 300 mM) were placed next to the container to enable conversion to sodium concentration in post-processing.

To correct for partial volume effects, morphological imaging was carried out by the means of a fat-suppressed gradient echo (GRE) sequence with the following readout parameters: 3D GRE, SENSE factor of 3 (AP), TR/TE/ $\Delta$ TE/FA = 48 ms/ 4.5 ms / 7.3 ms / 16 degrees, ProSet fat suppression, field of view = 120 x 120 x 150 mm<sup>3</sup>, resolution = 0.3 x 0.3 x 0.3 mm<sup>3</sup> with a total acquisition time of 4 minutes and 17 seconds.

### Biochemical analysis

Biochemical analyses were carried out directly after the MRI measurements on each stress-relaxation indentation location, corresponding to the marked locations on the photographs. A biopsy punch with a 3 mm diameter was used to core full-depth cartilage samples at these locations, after which a scalpel was used to remove the cartilage from the subchondral bone. All cores were blotted dry and weighted before papain digestion solution (250  $\mu$ g/mL papain (Sigma-Aldrich)) was added to the cartilage samples to digest the samples, which were incubated overnight at 60° C afterwards. The digested samples were diluted in PBS and stained with the DMMB staining solution<sup>92</sup>. The extinction was measured photospectrometrically at 525 and 595 nm with chondroitin-6-sulfate (Sigma-Aldrich) as a standard, after which the total amount of GAGs was measured by dividing the extinction at 525 nm by the extinction at 595 nm. The GAG concentration per wet weight was used in the data analysis.

## Data analysis

Three biomechanical parameters were derived from the stress-relaxation curves: apparent peak force, permeability and apparent equilibrium modulus. The peak force was derived from the stress-relaxation curve as the maximum (i.e. the end of the linear slope transitioning to the exponential decay). The peak force was then used to calculate an apparent peak modulus, by first dividing the peak force with the nominal cross-sectional area of the contact between the indenter and cartilage (being 1.6 mm<sup>2</sup> at the indentation depth of 0.3 mm) resulting in stress values. These were divided by the nominal strain, calculated as the indentation depth divided by the height of the cartilage as measured by proton MRI at the indentation location, resulting in an apparent peak modulus. The exponential decay of the stress-relaxation curve was fitted with a third order exponential fit, which yields three signal fractions (compartments) and three time constants. These time constants represent permeability which was calculated using poroelastic theory with  $k = (z^2)/h\tau$  where permeability  $k$  is derived from the cartilage height  $z$  squared divided by the (apparent) equilibrium modulus  $h$  and time constant  $\tau$ . This apparent equilibrium modulus was derived from the endpoint force of the exponential decay curve in similar fashion to the peak modulus.

The sodium images were converted to sodium concentration values by using a calibration curve. Three phantoms with known sodium curves were fitted with a linear function which was consequently used to correct the data from sodium intensity values to sodium concentration values (in mM). These sodium concentration values were corrected for the assumed 70% of water content<sup>4</sup>. To correct for the likely effect of partial volume effects (since the voxels in the sodium imaging protocol are 3x3x3 mm<sup>3</sup> and the cartilage probably thinner than 3 mm), the morphological scans are used to calculate the actual thickness of the cartilage per indentation location. These thicknesses are used to correct the sodium concentration values, where the assumption is made that the thickness of the cartilage is the same within a voxel and no detectable sodium being present within the voxel outside the cartilage.

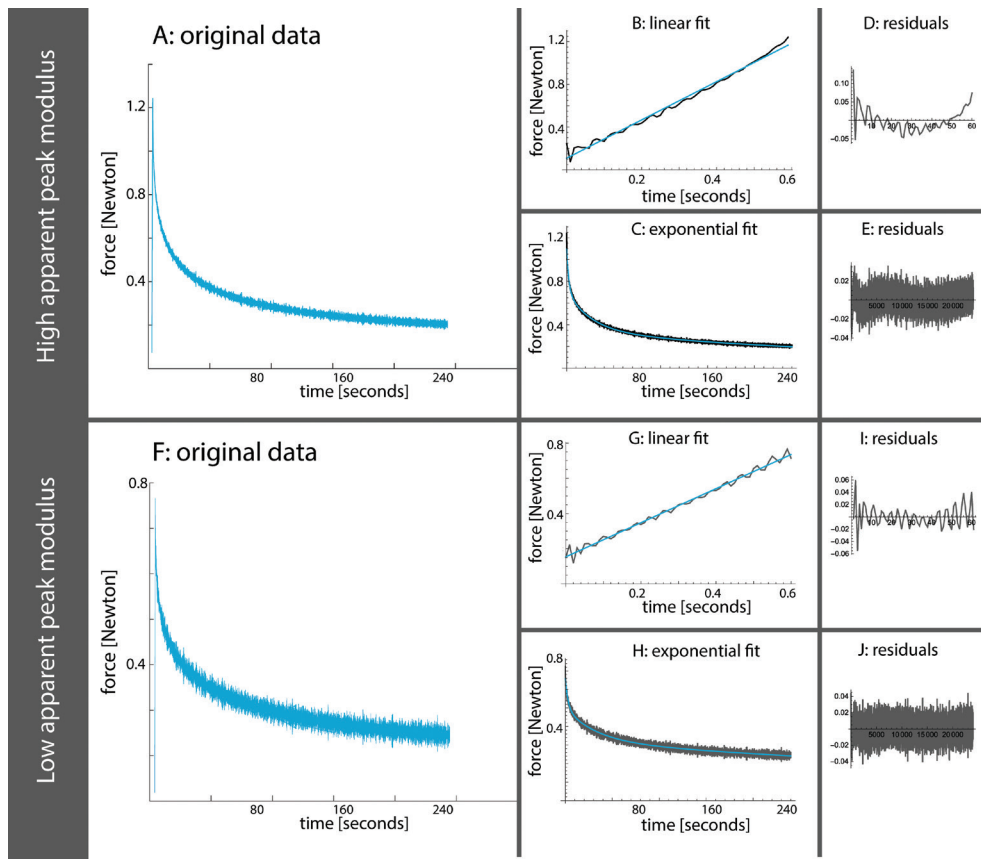
The sodium concentration values were manually matched to the indentation locations of the stress-relaxation tests for the comparative analysis. Data analysis was carried out in RStudio (version 1.2.1335; RStudio Inc., Boston, MA, USA). The first step of the analysis is the comparison of GAG concentration with the three biomechanical parameters. Hereafter the comparison is made between GAG concentration and MRI sodium concentration, which are known to be related to one another. Finally, the main hypothesis will be tested with the comparison of MRI sodium concentration values versus the biomechanical parameters.

Correlation coefficients (Pearson's  $r$ ) were calculated for outcome measures relating to each other. Consequently, generalized linear models were fitted to the same

parameters with plateau number as covariate. Data is stratified into severely degraded cartilage ( $\leq 1.5\text{mm}$  in height) and moderately degraded cartilage ( $>1.5\text{mm}$  in height).

## Results

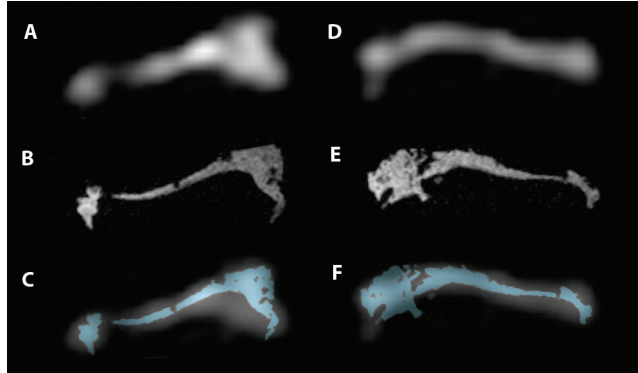
Four tibial plateaus were subjected to stress-relaxation indentation tests, over 64 locations (range 10-22 per plateau). Figure 1 shows two data examples, one of a sample with a higher apparent peak force and one of a sample with a lower apparent force. It can be appreciated that loading and relaxation behaviors of the high force sample do not have a constant pattern in the residuals of the fit.



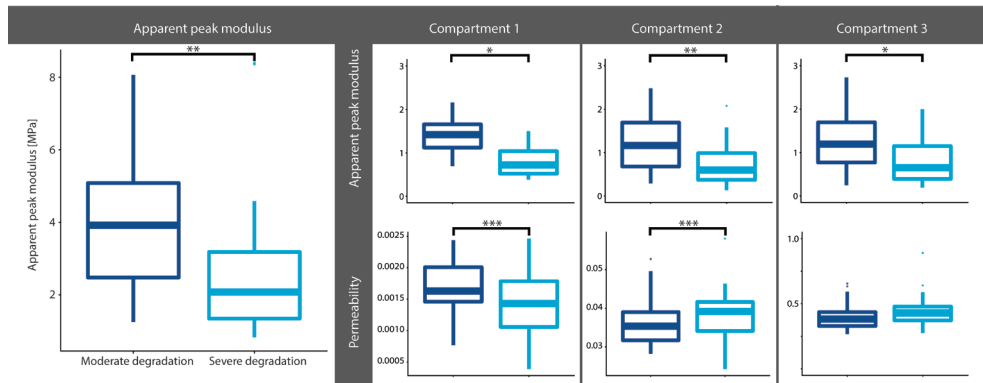
**Figure 1:** example of data fits (before conversion to apparent modulus) with a higher apparent peak force (upper part) and lower apparent peak force (lower part). Pane A&F show the original data in blue. Pane B&G show the first linear loading part of the stress relaxation test with fitted linear regression in blue. Corresponding residuals are shown in pane D&I. Pane C&H show the second part of the stress relaxation test fitted with a third order exponential decay in blue. Corresponding residuals are shown in pane E&J.



Figure 2 shows two MR image examples of tibial plateaus, in which the image quality can be appreciated of both sodium and proton scans. After MRI acquisition, tissue samples were harvested at each indentation location. In total 50 samples were acquired (range 4-19 per plateau). At 14 indentation locations, no samples were collected due to minimal to no cartilage.



**Figure 2:** image examples of two tibial plateaus. Sodium images are shown in pane A and D, with their corresponding proton images in B and E. Pane C and F shows the proton images (in blue) overlaid on the sodium scans, which is used for the partial volume correction.



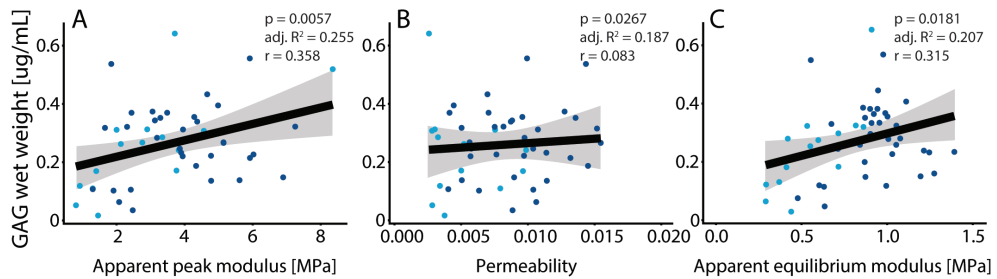
**Figure 3:** Exploration of difference in fit characteristics as shown in figure 1. Note: \*  $p < 0.05$ , \*\*  $p < 0.001$  and \*\*\*  $p < 0.0001$

Figure 3 shows the differences in apparent peak modulus between moderately and severely degraded cartilage. Higher apparent peak moduli are observed in moderately degraded cartilage, whereas lower apparent peak moduli are observed in severe degraded cartilage ( $p < 0.001$ ). These differences between moderate and severe degraded cartilage are also observed in the peak moduli and permeability within the first and second compartment of the exponential fit.

## Chapter 3

The stress-relaxation tests resulted in a mean apparent peak modulus of 3.36 MPa (range 0.83 – 8.37 MPa), a mean permeability (compartment 1) of 0.0077 (range 0.0006 – 0.0198) and a mean apparent equilibrium modulus of 0.81 MPa (range 0.30 – 2.28 MPa). The sodium 7T scans resulted in a mean sodium concentration of 108.1 mM over all the plateaus (range 40.3 – 255.2 mM) and the DMMB assays yielded a mean GAG wet weight content of 3.380 mg/mL (range 0.29 – 12.96 mg/mL).

Figures 4 to 6 show scatter plots of various outcome measures between one another. The linear model of whole data has been shown with a black line with corresponding confidence intervals in grey. The dark blue dots represent moderate degraded cartilage and light blue dots represent severe degraded cartilage. Figure 4 shows the correlation of GAG concentration with biomechanical parameters, showing weak correlations of GAG concentration with apparent peak modulus (4A) and apparent equilibrium modulus (4C). Figure 5 shows the lack of correlation of GAG concentration versus MRI sodium concentration.



**Figure 4: correlation of GAG concentration versus biomechanical parameters, showing weak correlations of GAG concentration with apparent peak modulus (pane A,  $p = 0.0057$ ) and apparent equilibrium modulus (pane C,  $p = 0.0181$ ). No tangible correlation was observed of GAG concentration versus permeability (pane B).**

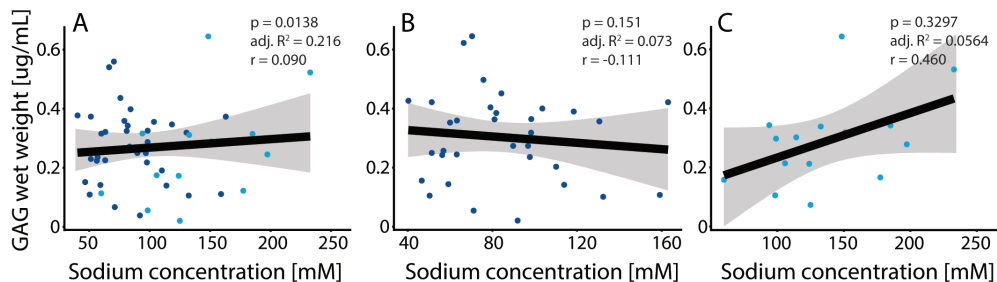


**Figure 5: correlation of GAG concentration versus MRI sodium concentration. Pane A shows a lack of tangible correlation. Pane B shows moderate degenerated cartilage samples, with no significant correlation. Pane C shows severe degenerated cartilage samples, with no significant correlation.**

Figure 6 shows the correlation of MRI sodium concentration with biomechanical parameters, showing a weak negative correlation of MRI sodium concentration with apparent peak modulus (6A) and a moderate correlation of MRI sodium concentration with permeability (6B).

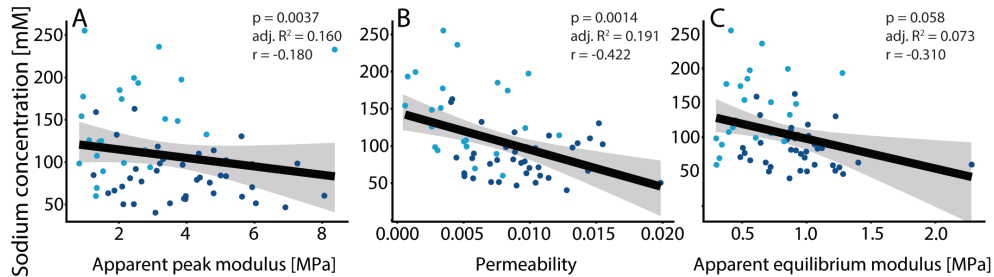


**Figure 6: correlation of MRI sodium concentration versus biomechanical parameters, showing a weak negative correlation of MRI sodium concentration with apparent peak modulus (pane A,  $r = -0.180$ ,  $p = 0.0037$ ) A moderate negative correlation was observed between MRI sodium concentration and permeability (pane B,  $r = -0.422$ ,  $p = 0.0014$ ). No significant correlation was observed between sodium concentration and apparent equilibrium modulus.**

## Discussion

We hypothesized that we could use sodium MRI to assess the stiffness of the cartilage to gain insight in early cartilage damage. No correlation was observed between apparent peak modulus and MRI sodium concentration, though the permeability was moderately correlated with MRI sodium concentration. GAG concentration was correlated with apparent peak modulus, but the expected correlation between GAG concentration and MRI sodium concentration was lacking.

This study was designed with a clear hypothesis in mind, for which state-of-the-art 7T MRI was used with a dedicated dual-tuned sodium/proton knee coil, optimized for cartilage imaging. We acquired high resolution sodium images (3 mm isotropic) and extremely high resolution isotropic proton images of 0.3 mm isotropic, fully using the potential of our 7T MRI. This led to a wide range of sodium concentration values observed on these plateaus, albeit on the lower end of the spectrum. The samples underwent thorough assessment on a tensile tester, mapping the entire cartilage surface of the tibial plateaus leading to a similarly wide range of apparent moduli observed. The apparent equilibrium modulus within this work of 0.82 MPa is in line with work of Kumar et al., showing an average equilibrium modulus of 0.9 MPa in moderately degraded cartilage (ICRS grade III)<sup>93</sup>.

Cartilage stiffness and GAG imaging, more specifically dGEMRIC (delayed

## Chapter 3

gadolinium-enhanced magnetic resonance imaging of cartilage), has been utilized in the past. Research of Baldassarri et al. showed differences in stiffness between cartilage specimen which were covered by meniscal tissue and specimen which were not covered<sup>94</sup>. Within our work, we do not have pre-TKR images which could confirm whether the menisci were intact. Some of the plateaus had some leftover meniscus, but it is likely that chunks are removed in the surgery. Additionally, the imaging analyses revealed that averaging tissue over a larger volume, as is the case with sodium imaging, possibly masks correlations. Earlier research of the same group found that the correlation decreased when the imaging results were averaged over the full thickness as compared with imaging results averaged over the indentation depth<sup>95</sup>. Given the 3 mm isotropic resolution of the sodium acquisition in this work, it could be that true correlations are masked due to the low imaging resolution.

The sequence of events in our testing procedures was as follows: first the indentation tests, followed by MR imaging and finally biochemical assays. Ideally, the least invasive test should be the first one to carry out, in this case MR imaging. Since Galden was used to submerge the plateaus for MR imaging (a thick, oily fluid) we were unsure whether this would influence the indentation tests. Therefore, we chose to do the indentation tests before the MR imaging, with the side-note that the stress-relaxation tests could have influence on the integrity of the cartilage. Within this sequence of events, we had to freeze the plateaus twice. This extra freeze-thaw cycle could possibly influence the cartilage properties, although the amount of GAGs should not change, therefore we expect this to be of minimal influence on the results. Additionally, Galden can cause the cartilage to dry out, though we did not assume any interaction between the fluid in the cartilage (and therefore no leakage of sodium) and the Galden.

The stress-relaxation tests were carried out with a spheroid indenter, with a diameter comparable to an arthroscopic probe (diameter of 2 mm). Due to the spheroid nature, the actual indented tissue is of a diameter smaller than 2 mm. The sodium MR images have a voxel size of 3 by 3 mm, which makes that the sodium concentration is measured in the area surrounding the indenter instead of directly underneath it. Theoretically, this resolution could be improved by increasing the acquisition time greatly. We chose to acquire the sodium MR images with this voxel size because of the acquisition time being clinically feasible, which makes it easier to translate these results to the clinic.

A number of post-processing steps are carried out in the conversion of sodium images to sodium concentration values, of which most are manually done. The segmentation, or selection, of voxels on the same location as the indentation tests have been carried out manually. Later on in this procedure, a number of conversion steps have been

taken. Firstly, for the water content correction within this work we chose a fixed content of 70% of water, which seems reasonable given the osteoarthritic nature of the cartilage. It is possible to measure the water content by using MRI but given the fact that all cartilage is osteoarthritic we chose a fixed content.

The final step in conversion to sodium concentration values is the partial volume effects correction. This correction is needed, because cartilage is often thinner than 3 mm (as is the sodium image resolution), meaning that the actual sodium signal comes from a smaller volume. Within each indentation location, the average thickness is measured on the morphological scan with a resolution of 0.3 mm isotropic. This means that a crude measurement (with steps of 0.3 mm, range of 1.2 to 3.0 mm) of thickness is retrieved, for which the sodium voxels are corrected. The assumption is made that the thickness is similar throughout the voxel. This thickness is also used to calculate the strain. The sodium concentration ranges we find are on the low side, since literature values suggest a range of 170-200 mM for osteoarthritic cartilage<sup>90</sup>. Although, a follow-up study of Madelin et al. showed a decrease of about 70 mM in osteoarthritic cartilage after a follow-up of 16 months<sup>96</sup>, which is more in line with our sodium concentration values.

The residuals resulting from fitting the stress-relaxation curves seem to be different in samples with a high apparent peak force versus a low apparent peak force. Though we do not expect changing the fitting parameters would lead to different results, the residuals shown a non-constant behavior in the linear fit and the exponential fit. We implemented a third-order exponential fit for the exponential part of the curve, which fits the data nicely with low residuals. Additionally, this third order exponential fit allows analysis in three compartments which could be related to triphasic models of articular cartilage<sup>89</sup>. Compartments 1 and 2 show the expected trends in permeability, which is expected to become higher with more severe cartilage degradation. This relation is confirmed with the moderate negative correlation of sodium and permeability, as shown in figure 6B. These observed differences between both groups in figure 2 are the reason behind the stratification of moderate and severe cartilage for instance in the analysis of sodium versus GAG wet weight. This stratification shows different relations in severely and moderately degraded cartilage, although both not significant relations.

Weak correlation of GAG concentration with apparent peak modulus ( $r = 0.358$ ) and apparent equilibrium modulus ( $r = 0.315$ ) have been observed, which is in line with the expected correlations although weaker. The equilibrium modulus should go down with decreasing GAG concentration, because at equilibrium the load is resisted by the solid modulus and swelling pressure – both directly proportional to GAG concentration. This questions whether a direct GAG MRI measurement should have

been applied within this work, which could have been done in theory with gagCEST<sup>74</sup>. Though, since gagCEST is temperature and pH dependent this would not have been a good choice in these *ex vivo* studies because those parameters are hard to keep controlled over various samples.

The correlation of GAG versus MRI sodium concentration was not observed. Here again, indentation locations (and therefore imaging locations) are manually co-registered with the cartilage samples taken for the assay. Degraded cartilage is often thinner, which makes it difficult to harvest. It could be that parts of the calcified layer of the cartilage are harvested as well, greatly increasing the weight of the cartilage but not increasing the GAG content. Though, the stratification based on height did not show better results in thicker (i.e. moderate degenerated) cartilage. Kulkarni et al. did DMMB assays in synovial fluid in various stages of OA, showing that there are basically two categories of end stage OA patients: one group with very high GAG content (possible active cartilage degeneration process) and significantly low GAG content (completely worn-out cartilage)<sup>97</sup>. This could be an important factor in the lack of correlation in our DMMB analyses versus sodium concentration, since mostly end-stage OA cartilage has been included. In the context of this work, the lack of correlation possibly shows that GAG measurements and MRI sodium measurements were potentially measuring different things in the context of biomechanical parameters. The relation of GAG concentration as measured with a DMMB assay and sodium MRI has been established in the past, but on intact animal samples<sup>42,98</sup> or healthy/early degraded cartilage<sup>99</sup>, all showing significant strong correlations. These results question whether sodium MRI could be validated in OA cartilage as included in this study. Additionally, a limitation of this work is that we did not include measurement of dry weight of GAG and water content separately, which theoretically could have given more insight in this (lack of) correlation.

The expected trend of a positive correlation of peak modulus versus MRI sodium concentration was not observed. On the contrary, a negative correlation of apparent peak modulus with MRI sodium concentration was observed (though very weak) as shown in figure 6A. The MRI sodium measurements did show a negative moderate correlation with permeability (as shown in figure 6B), again confirming that sodium MRI is potentially measuring different phenomena compared to GAG measurements.

In conclusion, sodium MR imaging was not found to be a good method to assess articular cartilage stiffness. GAG MRI measurements such as gagCEST might be a better alternative when interested in peak apparent moduli *in vivo*, but sodium MRI is a good alternative when interested in permeability of articular cartilage.

## Acknowledgements

The authors want to acknowledge Marieke van der Steen for her role in procuring the tissue and managing the IRB approval, Francesca Abinti and Rienk Schuiringa for their help with the indentation measurements and Mattie van Rijen for his help with the DMMB assays.

[illegible]



# T2\* mapping in an equine articular groove model – visualizing changes in collagen orientation

S. Brinkhof<sup>1</sup>, N.C.R. te Moller<sup>2</sup>, M. Froeling<sup>1</sup>, H. Brommer<sup>2</sup>, P.R. van Weeren<sup>2</sup>, K. Ito<sup>3,4</sup>, D.W.J. Klomp<sup>1</sup>

**1. Department of Radiology, University Medical Center Utrecht, Utrecht, Netherlands**

**2. Department of Clinical Sciences, Faculty of Veterinary Medicine, Utrecht University, Utrecht, The Netherlands.**

**3. Department of Orthopaedics, University Medical Center Utrecht, Utrecht, Netherlands**

**4. Orthopaedic Biomechanics, Department of Biomedical Engineering, Eindhoven University of Technology, Eindhoven, Netherlands**

**Journal of Orthopaedic Research, 2020**

## Chapter 4

## Abstract

T2\* mapping is promising for the evaluation of articular cartilage collagen. In this work, a groove model in a large animal is used as a model for post-traumatic arthritis. We hypothesized that T2\* mapping could be employed to differentiate between healthy and (subtly) damaged cartilage. Eight carpal joints were obtained from four adult Shetland ponies that had been included in the groove study. In this model, grooves were surgically created on the proximal articular surface of the intermediate carpal bone (radiocarpal joint) and the radial facet of the third carpal bone (middle carpal joint) by either coarse disruption or sharp incision. After nine months, T2\* mapping of the entire carpal joint was carried out on a 7.0T whole body magnetic resonance imaging (MRI) scanner by means of a gradient echo multi echo sequence. Afterwards, assessment of collagen orientation was carried out based on Picrosirius Red-stained histological sections, visualized by polarized light microscopy (PLM). The average T2\* relaxation time in grooved samples was lower than in contralateral control sites. Opposite to the grooved areas, the “kissing sites” had a higher average T2\* relaxation time than the grooved sites. PLM showed mild changes in orientation of the collagen fibers, particularly around blunt grooves. This work shows that T2\* relaxation times are different in healthy cartilage versus (early) damaged cartilage, as induced by the equine groove model. Additionally, the average T2\* relaxation times are different in kissing lesions versus the grooved sites.

## Introduction

Osteoarthritis (OA) is a progressive whole-joint disease which is characterized by degeneration of the articular cartilage, synovitis and bone remodeling in synovial joints resulting in patients suffering from joint stiffness, reduced range of motion and often pain<sup>18</sup>. This cartilage degeneration is characterized by loss of glycosaminoglycans (GAGs) and alterations to the collagen fiber network<sup>53</sup>. Although, up until today, there is no cure for osteoarthritis, early detection of cartilage damage is essential for (future) therapy planning in order to prevent or decelerate the progressive irreversible damage to the joint.

T2\* mapping is sensitive to water content and to the degree of orientation of the collagen fiber network within the articular cartilage<sup>100</sup>. In addition, zonal variations in the depth of the articular cartilage could be visualized by employing T2\* mapping<sup>101</sup>. Since articular cartilage has a high curvature, T2\* mapping is ideally implemented on an ultra-high field scanner to achieve a high spatial resolution which is needed to correctly map the thin layer of cartilage. It has been shown that T2\* mapping is feasible on a 7T MRI with diagnostic imaging quality<sup>62</sup>. However, T2\* relaxation time on 7T is significantly shorter than on 3T, which has to be taken into account for the imaging protocols used<sup>102</sup>. T2\* mapping has been successfully applied within a number of joints in the human body, such as the hip<sup>61,62</sup>, knee<sup>63,64</sup> and ankle<sup>65,66</sup>. To test whether T2\* mapping could serve as a biomarker for (early) cartilage degeneration in a controlled fashion, one could employ an animal model such as a groove model, serving as a model for post-traumatic arthritis.

The cartilage groove model has been used for OA research in rats<sup>103</sup>, dogs<sup>104</sup>, sheep<sup>105</sup>, and horses<sup>106</sup>, and has shown its potential to create post-traumatic arthritic changes in the joint. In this model, the cartilage layer is grooved through the superficial, middle and deep zone (leaving the calcified layer intact) and the joint is subjected to intensified loading. The horse in particular is an interesting model because of the similarities between equine and human cartilage<sup>107</sup>. Recently, the groove model has been applied in the equine carpal joint in two variants: grooves were surgically created by either blunt disruptions or sharp incisions (blunt grooves and sharp grooves, respectively). The contralateral joint was sham-operated and used as a control<sup>108</sup>.

It is believed that blunt grooves and sharp grooves create different types of damage and consequently different progression of disease. In this study, we investigated the difference in cartilage integrity between grooved and control sites and between the two groove types. For that purpose, ultra-high field magnetic resonance imaging (MRI) was employed by means of a T2\* mapping sequence to gain insight in cartilage quality. T2\* is sensitive to magnetic susceptibility differences, and shortens in

proximity to transitions between tissues like water to bone. We hypothesized that T2\* relaxation times 1) are shorter in grooved cartilage than in control cartilage, 2) are different in the “kissing sites” (i.e. the contact surface of the grooved cartilage) compared with grooved cartilage or control cartilage, and 3) can distinguish between blunt and sharp grooves.

## Methods

### Subjects

Four adult female Shetland ponies with a mean age of 7.3 years (SD 3.9 years, range 4 to 13 years) and with a mean bodyweight of 203 kg (SD 21.8 kg, range 171 to 220 kg) were included in this study (table 1). The study was authorized by the Utrecht University Animal Experiments Committee and the Central Committee for Animal Experiments (AVD108002015307).

**Table 1: Overview of subject characteristics, grooved side, and groove types per joint.**

Nr	Age at start of study (years)	Weight at start of study (kg)	Grooved joint	Control joint	Blunt-grooved joint	Sharp-grooved joint
1	6	209	Right	Left	Radiocarpal	Middle carpal
2	4	220	Left	Right	Middle carpal	Radiocarpal
3	13	171	Right	Left	Middle carpal	Radiocarpal
4	6	212	Right	Left	Middle carpal	Radiocarpal

### Surgical procedure

The grooves were induced in a randomly chosen front limb through an arthrotomy at two locations: the radial facet of the third carpal bone (in the middle carpal joint), and the dorsoproximal surface of the intermediate carpal bone (in the radiocarpal joint). Blunt and sharp grooves were randomly assigned to either one of the joints (table 1). Blunt grooves were induced with a hooked arthroscopic probe with a sharpened tip; sharp grooves were made with a surgical blade such that incisions were of equal depth and could not exceed 400  $\mu$ m. The contralateral joints were sham-operated and used as controls. The ponies were subjected to an exercise program for eight weeks, starting three weeks post-surgery<sup>108</sup>. The ponies were euthanized in week 39, after which the carpal joints were harvested and stored at -20 degrees Celsius.

### MRI experiments

MRI experiments were carried out on a 7.0 Tesla whole body scanner (Achieva; Philips Healthcare, Best, Netherlands) with a 32 channel receive head coil (Nova Medical, Wilmington, MA, USA). The carpal joints were placed in the head coil with the dorsal side upwards parallel to the Z-direction of the magnetic field, such that the articular

cartilage surfaces were located orthogonal towards the Z-direction of the magnetic field.

T2\* mapping was carried out by means of a multi-echo gradient echo (ME-GRE) sequence with the following readout parameters: 3D GRE, SENSE factor of 1.5 (AP), TR/TE/ $\Delta$ TE/FA = 48 ms/ 4.5 ms / 7.3 ms / 16 degrees, ProSet fat suppression, field of view = 120 x 120 x 70 mm<sup>3</sup>, resolution = 0.3 x 0.3 x 0.3 mm<sup>3</sup> with a total acquisition time of 17 minutes and 53 seconds. Four echo times were used: 4.5, 12, 19 and 27 ms, which were optimized based on the expected T2\* relaxation time of 15 to 20 ms.

### Polarized Light Microscopy

Osteochondral samples of the whole joint surface, including the grooved sites, the kissing sites, and the contralateral controls, were fixed in formalin and decalcified for histology<sup>108</sup>. Five- $\mu$ m sections, perpendicular to the articular surface and grooves, were stained with Picrosirius red staining. Stained sections were examined using a light microscope (Olympus BX51) by polarized light microscopy for visualization of collagen fibril orientation.

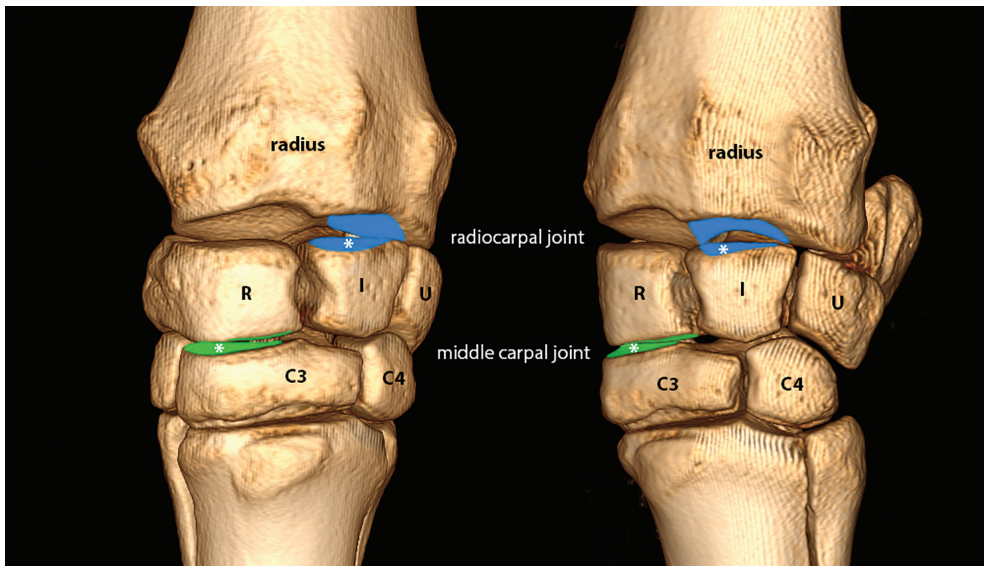


**Figure 1:** Dorsomedial-palmarolateral oblique view (left pane) and dorsolateral-palmaromedial oblique view (right pane) of a left carpus. The following VOIs are used in the analysis: distal surface of the radius, dorsoproximal surface of the intermediate carpal bone (I) (blue), distal surface of the radial carpal bone (R), radial facet of the proximal surface of the third carpal bone (C3) (green). Grooved surfaces are marked with \*.

## Image analysis

Volumes of interest (VOI) were drawn using ITK-SNAP (version 3.4.0) in the radiocarpal joint (distal surface of the radius and dorsoproximal surface of the intermediate carpal bone) and the middle carpal joint (distal surface of the radial carpal bone and radial facet of the third carpal bone). These locations included the grooved and kissing sites, and their contralateral controls. This resulted in four VOIs per joint (figure 1). These VOIs were saved as NIFTI files and transferred to MATLAB (R2017b, the MathWorks, Natick, MA, USA) to carry out the analysis. Fitting an exponential T2\* decay function was carried out by a nonlinear least-squares algorithm<sup>109</sup>. The average T2\* values per VOI were reported and the median T2\* values were reported per sample group.

## Results

From the 32 sites available (4 ponies, 2 legs/pony, 4 VOI/leg), a total of 30 sites were included for VOI analysis. Excellent high resolution T2\* imaging could be performed showing T2\* contrast as shown in figure 2A, with T2\* maps of sharp grooved and blunt grooved cartilage (2C and 2D). The left middle carpal joint of pony 2 contained a large air bubble (figure 2B) caused by the surgery that was performed upon euthanasia (out of the scope of this paper). Therefore, these two sites in this joint were excluded from analysis.

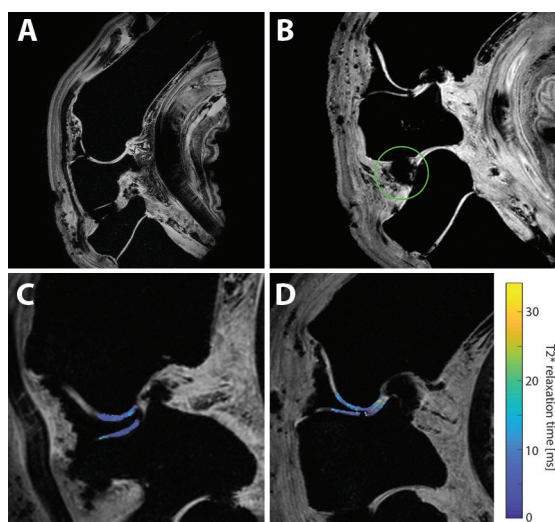


**Figure 2:** pane A shows a healthy, non-grooved carpus. Pane B shows a sagittal slice of the carpus of pony 2, highlighting the air bubble in the intercarpal joint (green circle). Pane C and D show T2\* maps of the radiocarpal joint with sharp grooved cartilage (pane C) and blunt grooved cartilage (pane D, where the cartilage defect due to the groove can be appreciated).

The median  $T2^*$  relaxation time of the sample group of grooved sites was lower (6.06 ms) compared to their contralateral (7.43 ms) counterparts in the blunt grooved sample group and similarly in the sharp grooved group (7.41 ms and 9.58 ms respectively), as shown in figure 3. Additionally, the median  $T2^*$  relaxation time of the grooved sites was lower (6.11 ms) as compared to their opposite kissing sites (7.17 ms). Similar patterns were observed in the sharp grooved sample group (7.77 ms and 8.34 ms, respectively) (Figure 4). No substantial differences have been observed in  $T2^*$  relaxation time between groove types.

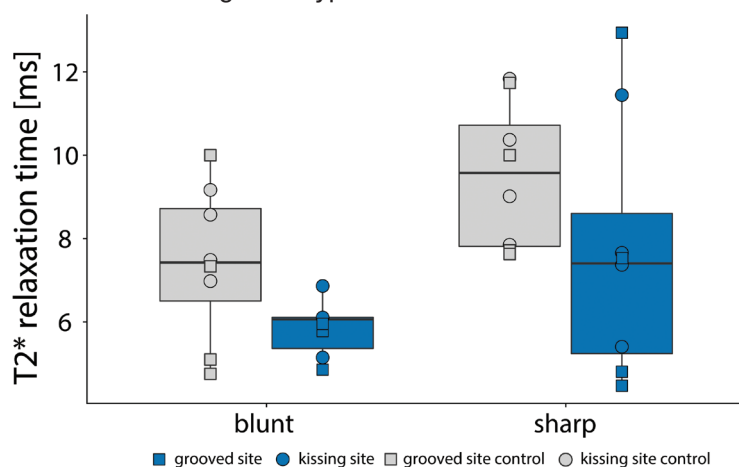


**Figure 3:  $T2^*$  relaxation times in VOIs with blunt grooves and sharp grooves compared with contralateral control sites. The grooved sites are shown in blue and control sites in grey.**

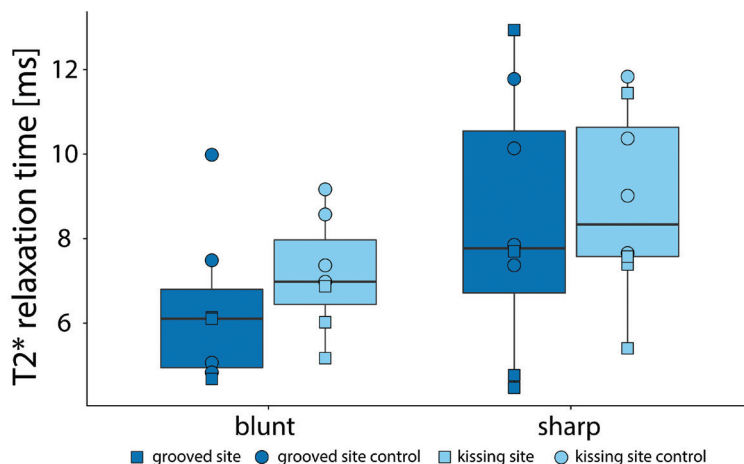


**Figure 4:  $T2^*$  relaxation times in VOIs with blunt grooves and sharp grooves compared with their kissing sites. The grooved sites are shown in dark blue and the kissing sites in light blue.**



When picrosirius red-stained sections were analysed under polarized light, typical collagen fibre structures could be recognized in control sites, i.e. parallel oriented fibres in the superficial layer (showing bright yellow), followed by a zone with low birefringence, first containing obliquely oriented and then perpendicular oriented fibres. This collagen structure did not seem to be affected in the cartilage tissue in between grooves. Only in cartilage with blunt lesions, higher birefringence (bright yellow) and slight disruption of normal orientation was observed in all blunt lesions directly around the grooves of which an example is shown in figure 5. The PLM images nicely showed the relatively unharmed control sites, with one example showing mild damage in the superficial layers of the cartilage. These could be due to the sham surgery performed on the contralateral control sites.

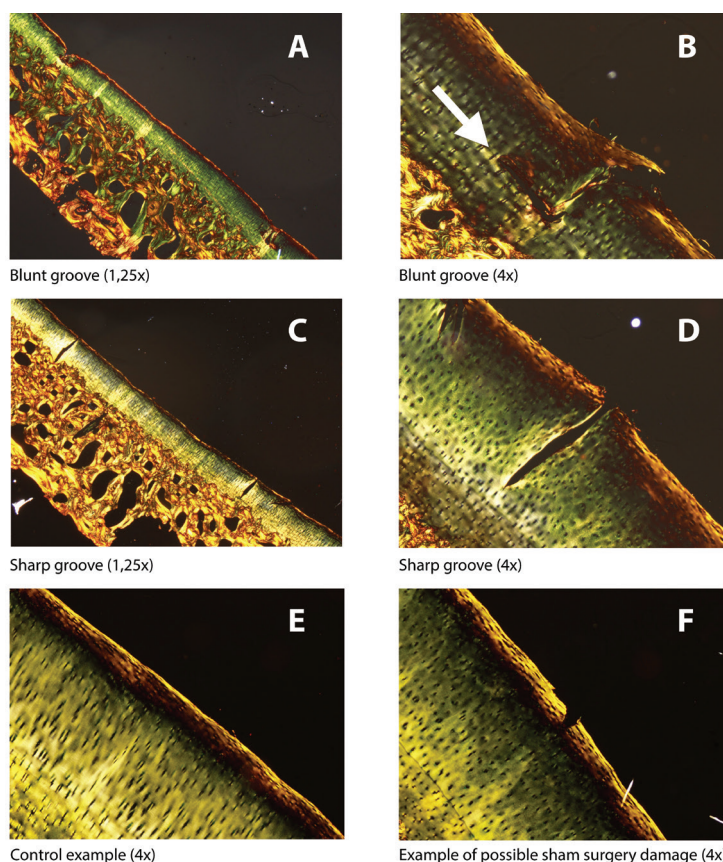


**Figure 5: Picro-sirius red stained sections analyzed under polarized light. Blunt grooves are shown in the panes A (1.25x magnification) and B (4x magnification). The white arrow points towards slight disruption of normal collagen orientation. Sharp grooves are shown in panes C (1.25x magnification) and D (4x magnification). Pane E shows an example of a control site and an example of possible damage due to sham surgery in a control site is shown in pane F.**

## Discussion

This explorative study investigated T2\* relaxation times in equine articular cartilage 39 weeks after application of two types of artificially created grooves (i.e. blunt grooves and sharp grooves randomized over the radiocarpal and middle carpal joint), followed by an 8-week exercise program. The median T2\* relaxation time of the sample group of grooved sites was lower compared to their contralateral control sites. Additionally, the median T2\* relaxation time of the sample group of grooved sites was lower in relation to their opposite kissing sites.

While a number of analyses are described in more detail in the thesis of te Moller<sup>108</sup>, the most important ones relating to this work are discussed here. Histology slides were stained with Safranin-O/Fast-green to enable scoring using the OARSI histopathological guidelines, showing significantly higher OARSI scores in blunt- and sharp-grooved sections compared to their contralateral control sites. This implies that there was damage in the cartilage, which could be measured with T2\* mapping. Additionally, blunt-grooved sections showed higher OARSI grades than sharp-grooved sections<sup>108</sup>. Blunt grooves showed to have an impact on the kissing site, in most samples an imprint was seen opposite to the groove. These two findings possibly explain the generally lower T2\* relaxation times in the sample group with blunt-grooved cartilage. Another explanation could be that the superficial zones are damaged or partly disappeared, such that the average T2\* values within the VOI mostly reflect the middle and deep zone of the cartilage. Several studies have shown a tendency to a decrease in T2\* relaxation times from superficial to deep zone<sup>101,110</sup>. Hesper et al. found that T2\* relaxation times were lower in damaged cartilage, as evaluated by arthroscopy<sup>61</sup>. T2\* relaxation has also shown to decrease in OA patients when compared with healthy controls<sup>109</sup>. These results confirm that T2\* mapping can be used as a measurement for damaged cartilage.

Since the end goal is an imaging protocol which can be used as a biomarker in human cartilage, the comparison is made with human ankle cartilage because of the similar cartilage thickness and load distribution. T2\* relaxation values in the human ankle are relatively low, where talar cartilage (the proximal surface of talus) has a higher T2\* relaxation (20.5 ms  $\pm$  1.6ms) compared to the tibial cartilage (the distal surface of tibia, 15.2  $\pm$  2.1ms)<sup>66</sup>. Other studies showed even lower values for talar cartilage (11.8 ms, also measured at 3T<sup>111</sup>). The same relation holds in carpal cartilage of ponies as shown in this work (comparison with kissing sites in figure 4), where the proximal surface of the intermediate carpal bone has higher T2\* relaxation times compared to the distal surface of the radial bone. The same relation holds for the (radial facet of) the proximal surface of the third carpal bone versus the distal surface of the radial carpal bone.

A limitation of this work is that due to the randomization, grooved sides and groove types were not evenly distributed (*i.e.* three right and one left front limb(s) grooved; three sharp grooved radiocarpal joints, one blunt grooved radiocarpal joint, and vice versa for the middle carpal joint). This relates to the differences in T2\* relaxation time between blunt grooves and sharp grooves which are present, but the differences between the joint types (radiocarpal versus middle carpal) have to be taken into account. The underlying limitation of this is the small sample size within this study - we included four ponies, with eight legs, divided into four groups (being contralateral control blunt, blunt grooved, contralateral control sharp and sharp grooved).

One of the limitations of T2\* mapping in general is that T2\* mapping is prone to magic angle artifacts. By placing the samples consequently in the same way in the scanner (dorsal side upwards which caused the cartilage surfaces to be orthogonally oriented towards the magnetic field) we tried to minimize the influence of magic angle effects. Cartilage T2 and therefore also T2\* was shown to approximately follow the angular dependence of the nuclear dipole-dipole interaction, which has its maximum at 55 degrees<sup>112</sup>. This effect is even more pronounced in highly ordered collagenous structures such as the meniscus<sup>113</sup>. Within this work we specifically chose to implement T2\* mapping instead of T2 mapping because it can be implemented with a higher spatial resolution and can be acquired faster, providing more specific information on local tissue disruption that causes steep transitions between tissues of different magnetic susceptibilities<sup>114</sup>.

Another limitation of the T2\* mapping is the number of echo times, which could be increased for a clinical T2\* mapping protocol (four in this work, where at least six would be beneficial for the fitting - although increasing the acquisition time in that case) and the actual chosen echo times can be optimized further. Since the end goal is an imaging protocol which can be used as a biomarker in human cartilage, the comparison is made with human ankle cartilage because of the similar cartilage thickness and load distribution. T2\* relaxation values in the human ankle are relatively low, ranging from 11.8 ms to 20.5 ms<sup>66,111</sup>. Given these values, we chose four echo times in the range of 4.5 to 27 ms, because of the expected T2\* relaxation times reported in literature. In retrospect, more echo times in the lower range (below 10ms) would have benefited our results. Additionally, the number of echo times chosen in this work does not allow for bi-exponential fitting, as is sometimes employed in the analysis of T2\* mapping in articular cartilage.

The acquisition time of the T2\* mapping protocol used was long due to the high spatial resolution, which has to be taken into account for clinical implementation. The scan time was long because the head coil was used with corresponding SAR model, which is too conservative for scanning of extremities. With our knee coil, we

## Chapter 4

could increase the SAR (IEC limit for extremities 40W/kg local SAR instead of 10W/kg for head), and therefore decrease the acquisition time. Additionally, the SENSE factor can be increased by using receive arrays close to the volume of interest, even decreasing the acquisition time further.

In conclusion, this work shows that T2\* relaxation times are different in healthy cartilage versus (early) damaged cartilage as induced by an equine groove model. Additionally, the median T2\* relaxation times are different in kissing lesions versus the grooved sites.

## Acknowledgements

The authors acknowledge Saskia Plomp for assistance with histology. This research was made possible by an NWO Graduate Programme Grant (022.005.018).

## T2\* mapping in an equine articular groove model

chapter  
chapter  
chapter  
chapter

4

[illegible]

# Detection of early cartilage damage: feasibility and potential of gagCEST imaging at 7T

S. Brinkhof<sup>1</sup>, R. Nizak<sup>2</sup>, V. Khlebnikov<sup>1</sup>, J.J. Prompers<sup>1</sup>, DWJ. Klomp<sup>1</sup>,  
D.B.F. Saris<sup>2,3,4</sup>

1. Department of Radiology, UMC Utrecht, Utrecht, the Netherlands
2. Department of Orthopaedics, UMC Utrecht, Utrecht, the Netherlands
3. MIRA institute for Biomedical Technology and Technical Medicine, University of Twente, Enschede, the Netherlands
4. Department of Orthopaedics, Mayo Clinic, Rochester, Minnesota, United States

European Radiology; 28; 2874-2881

## Abbreviations and acronyms

CV	coefficient of variation
GAG	glycosaminoglycans
gagCEST	glycosaminoglycan chemical exchange saturation transfer
ICC	intraclass correlation coefficient
ICRS	International Cartilage Repair Society
OA	osteoarthritis



## Abstract

### Objectives

The purpose was to implement a fast 3D glycosaminoglycan Chemical Exchange Saturation Transfer (gagCEST) sequence at 7T, test stability and reproducibility in cartilage in the knee in healthy volunteers, and evaluate clinical applicability in cartilage repair patients.

### Methods

Experiments were carried out on a 7T scanner using a volume transmit coil and a 32-channel receiver wrap-around knee coil. The 3D gagCEST measurement had an acquisition time of seven minutes. Signal stability and reproducibility of the GAG effect were assessed in eight healthy volunteers. Clinical applicability of the method was demonstrated in five patients before cartilage repair surgery.

### Results

Coefficient of variation of the gagCEST signal was 1.9%. The reproducibility of the GAG effect measurements was good in the medial condyle (ICC = 0.87) and excellent in the lateral condyle (ICC = 0.97). GAG effect measurements in healthy cartilage ranged from 2.6%-12.4%, compared with 1.3%-5.1% in damaged cartilage. Difference in GAG measurement between healthy cartilage and damaged cartilage was significant ( $p < 0.05$ ).

### Conclusions

A fast 3D gagCEST sequence was applied at 7T for use in cartilage in the knee, acquired within clinically feasible scan time of seven minutes. We demonstrated that the method has high stability, reproducibility and clinical applicability.

## Introduction

With the aging of our society, the prevalence of degenerative diseases, like osteoarthritis (OA), has increased<sup>19</sup>. OA is a degenerative whole-joint disease which affects the articular cartilage. Since cartilage tissue has a limited ability to regenerate, early identification of cartilage damage improves chances of successful treatment and prognosis<sup>1,87</sup>. Early-stage OA and early-stage cartilage damage in general are subject to delicate changes in biochemical composition, i.e. a loss of glycosaminoglycans (GAG), on the surface of the cartilage<sup>53</sup>). The measurement of reductions in GAG is a promising approach for the diagnosis and treatment monitoring of early-stage OA. MRI is an excellent modality to visualize cartilage morphology; however, a standard anatomical MRI is not sufficient to visualize early-stage OA.

Quantitative MRI has been used increasingly over the past years to quantify GAG content in vivo in OA<sup>115,116</sup>. Initial studies focused on the application of delayed Gadolinium Enhanced MRI of Cartilage (dGEMRIC)<sup>117,118</sup>, to measure GAG content indirectly. This technique is based on the distribution of negatively charged ions of a gadolinium-based contrast agent in cartilage, which is inversely proportional to the GAG content<sup>72</sup>. Another technique to assess GAG content, without the use of a contrast agent, is T1 $\rho$  mapping. In this technique, spinlock pulses of different durations are applied to assess the T1 $\rho$  relaxation time, which is lower in water associated with large macromolecules, such as GAG, as compared to free water. However, it is still disputed whether T1 $\rho$  is directly correlated with GAG content<sup>119</sup>. Alternatively, sodium (<sup>23</sup>Na) MRI measures the sodium ions in the interstitial fluid in the cartilage<sup>4,76,120</sup>. Sodium counterbalances the negative charge of the sulfate and carboxyl groups of GAG. A lower fixed charge density (FCD), thus a loss of GAG, causes a loss of sodium ions from cartilage<sup>4</sup>. However, for <sup>23</sup>Na MRI dedicated MRI coils are required, which are highly experimental and not widely available.

In contrast to these assessments of GAG, Chemical Exchange Saturation Transfer (CEST) directly quantifies GAG content based on the chemical exchange of its labile hydroxyl (-OH) protons with the bulk water<sup>44,47,48</sup>. These exchangeable protons resonate at a different frequency compared with bulk water protons and are saturated via selective radio frequency (RF) irradiation. Because of the exchange, the saturation is transferred to the bulk water pool, which ultimately results in large contrast enhancement factors<sup>47,49–51</sup>. The quantification of GAG in articular cartilage with the use of CEST, i.e. gagCEST, has a high potential for the examination of cartilage degeneration and hence diagnosis of early-stage OA. However, in previous applications gagCEST data were mostly acquired in 2D because 3D sequences are very time consuming<sup>48,121,122</sup>. The purpose of this study was to implement a fast 3D gagCEST sequence at 7T with a clinically feasible scan time, and to evaluate the

stability, reproducibility and clinical applicability of this method in articular cartilage in the knee.

## Methods

### Numerical simulations

The 3D gagCEST sequence implemented in this work is a pseudo-steady state pulsed 3D gradient echo CEST sequence recently developed in our group <sup>123</sup>. The sequence was optimized through the Bloch-McConnell simulations <sup>124</sup>. The following sequence parameters were investigated: the number of saturation pulses, transmit field ( $B_1^+$ ) amplitude and duty cycle. All other sequence parameters were fixed to the values that were eventually used for data acquisition <sup>123</sup>. Gradient and RF spoiling were simulated by setting the transverse magnetization components to zero. Two-pool (free water and GAG) Bloch-McConnell equations were solved numerically <sup>125</sup> assuming the parameters in Table 1.

**Table 1: Overview of parameters for Bloch-McConnell equation simulations**

	Water	GAG
$T_1$ (s)	1.2	1 *
$T_2$ (ms)	40	10
$\Delta\omega$ (ppm)	0	0.9
$M_0$ (%)	-	0.27
$R$ (Hz)	-	1000

\* Fixed in simulation

GAG effect size was quantified by the pool difference method:

$$\text{GAG} = S(0.9 \text{ ppm}, M_A = 0) - S(0.9 \text{ ppm}, M_A = 1) \quad (1)$$

where  $S(\Delta\omega, M_A)$  is the simulated signal in the z-spectrum at  $\Delta\omega = 0.9$  ppm, and  $M_A$  is the simulated amplitude of the GAG compartment. The saturation parameters were chosen to achieve an optimal GAG effect size, but with as low as possible acquisition time and within the limitations of RF amplifier duty cycle.

### MRI data acquisition

Eight healthy volunteers without a history of knee pain or trauma and five patients undergoing arthroscopy for repair of a focal knee cartilage defect were included in this study (approved by the medical ethics committee). Patients were selected within our specialized knee clinic of the University Medical Center Utrecht. Patients undergoing an arthroscopy for cartilage repair on the femoral condyle were included for a pre-

operative MRI. Exclusion criteria were as follows: history of cartilage repair, history of cruciate ligament tears or repair, and/or trochlear/patellar cartilage damage. Informed consent was acquired from all the subjects after explaining the study procedures. MRI experiments were carried out on a 7.0 Tesla whole-body scanner (Achieva; Philips Healthcare, Best, Netherlands), using an in-house developed and built volume transmit coil and a dedicated, 32-channel receiver wrap-around knee coil (MR Coils BV, Zaltbommel, the Netherlands).

The 3D gagCEST sequence included a pre-saturation module consisting of a train ( $n = 20$ ) of sinc-shaped pulses ( $B_1 = 2 \mu\text{T}$ , pulse length = 25 ms, duty cycle = 70%, based on simulations). The readout parameters were as follows: five shot Turbo Field Echo (TFE), TFE factor of 370, SENSE factor of 2, TR/TE/FA = 2.75 ms/1.4 ms/5 degrees, Field of View =  $140 \times 150 \times 135 \text{ mm}^3$ , resolution =  $1 \times 1 \times 3 \text{ mm}^3$ , inter-shot T1 recovery time = 2 seconds, k-space center-weighted acquisition, two dummy scans, total acquisition time = 6 min 59 s.

The gagCEST images were acquired at 17 saturation offsets ranging from -900 Hz to 900 Hz (-3 ppm to 3 ppm), i.e. -900, -600, -425, -350, -275, -200, -75, -25, 0, 25, 75, 200, 275, 350, 425, 600, and 900 Hz. In addition, gagCEST images were acquired at offsets of -100 kHz and +100 kHz to normalize the CEST spectrum. The expected resonance frequency of the hydroxyl side groups of GAG is 0.9 ppm, which is 270 Hz at 7 T<sup>47</sup>.

Signal stability tests were carried out in five healthy volunteers (mean age: 26 years, age range: 21 to 35 years, two males and three females). Each subject was scanned twice and during each session 19 gagCEST images were acquired at a single saturation offset of 0.9 ppm (270 Hz). 19 acquisitions were chosen to represent the same scan duration as for the gagCEST experiment with 19 different offsets.

The reproducibility of the measurement of the GAG effect was assessed in eight healthy volunteers (mean age: 24 years, age range: 21 to 30 years, three males and five females). Each subject was scanned twice within the same scan session.

The clinical applicability of the method was demonstrated by comparing the GAG effect size in healthy cartilage versus damaged cartilage in five patients before cartilage repair (age range: 21 to 41 years, all male, no significant/obvious varus or valgus leg axis). These patients were scanned up to 24 hours prior to surgery. During surgery, cartilage defects were graded with the International Cartilage Repair Society (ICRS) grading scale (grade 0 to 4, 0 = no damage, 4 = full thickness cartilage defect)<sup>126</sup>. The ICRS grade was graded in the femoral cartilage, because we solely included patients with defects in the cartilage of the femoral condyles. The cartilage on the healthy condyle was graded with ICRS grade 0.

## Image analysis

Data analysis was performed in MATLAB (R2016b, the MathWorks, Natick, MA, USA) with in-house developed processing scripts. The signal stability measurements were normalized with respect to the signal intensity of the first measurement. The signal stability was quantified from the averaged signal over all pixels in each of the three regions of interest (ROI): the medial condyle, the trochlear groove and the lateral condyle. These regions were also used for the quantification of the reproducibility of the GAG effect.

CEST spectra were  $B_0$  corrected using WASSR<sup>127</sup> and were normalized using the high off-resonant gagCEST images at  $\pm 100$  kHz. The  $B_0$  corrected and normalized spectra were fitted pixel-wise using a sum of three Lorentzians to account for GAG, water and magnetization transfer pools<sup>128</sup>. The GAG effect is expected around 270 Hz, for which we chose three offsets to represent that point (200, 275, 350 Hz). The amplitude of the GAG pool, is averaged over these three offsets to avoid outliers in the fit.

A 3D segmentation of the cartilage was used to evaluate the GAG effect in the patient group. Both weight-bearing condyles were divided into four regions (medial/lateral/superior/inferior) and the regions where a defect was present, according to the surgeon's notes, were used for the analyses. These defect regions also include the defect rim, which is of great interest for treatment planning. These defect regions were compared with the same regions on the healthy contralateral condyle. A detailed explanation of the analysis workflow and the described regions of interest are shown in the Appendix.

## Statistical analysis

Stability of the signal (i.e. the value of the CEST spectrum at 275 Hz, where the GAG effect is expected) is expressed with the coefficient of variation (CV), which was calculated by dividing the standard deviation by the mean of the signal. The coefficient of variation was calculated in the three aforementioned ROIs and was calculated for both acquired stability assessments. The reproducibility of the GAG effect size was assessed by means of Bland-Altman plots and correlation plots with corresponding intraclass correlation coefficients (ICC), i.e. the degree of absolute agreement among measurements (criterion-referenced reliability). To evaluate differences between healthy cartilage and damaged cartilage in the patients, a Wilcoxon signed rank test was applied.

## Results

### Simulation data

Figure 1 shows results of Bloch-McConnell simulations for the applied sequence. The number of pulses in the train was chosen to 20 pulses, which was close to the maximum effect size for GAG but still within a clinically feasible acquisition time. A duty cycle of 70% was used to stay within RF amplifier duty cycle limits. 2  $\mu\text{T}$  was chosen to approach the optimal effect size within the desired acquisition time. The combination of both leads to a maximum effect size of roughly 8 percent, which is in line with the chosen number of pulses in the prepulse train.

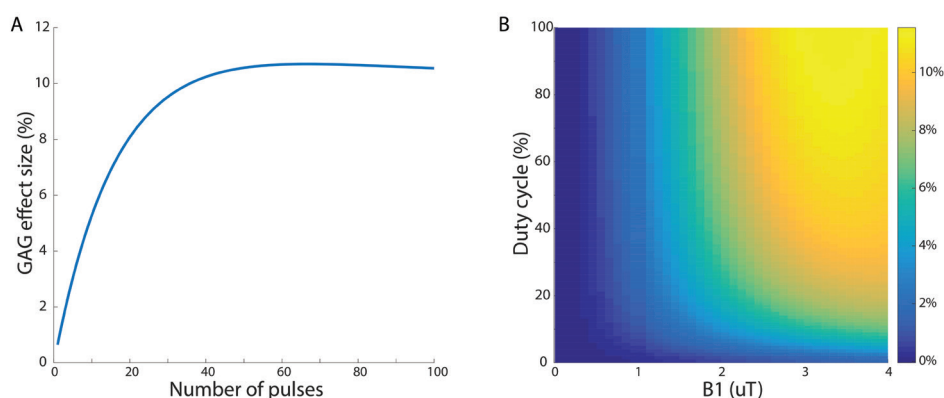


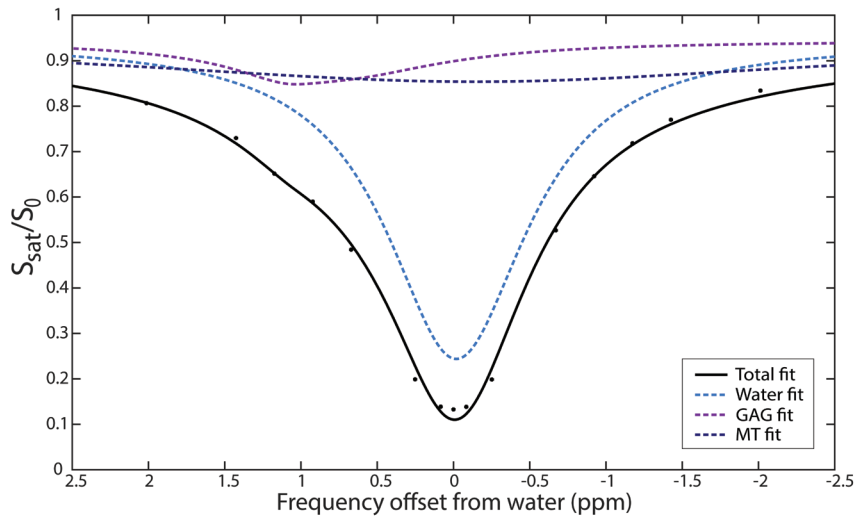
**Figure 1. (A) The simulated GAG effect size (%) as a function of the number of pulses in the CEST prepulse. (B) The simulated 3D plot of GAG effect size (%) as a function of RF duty cycle (of the CEST prepulse) and B1+ field amplitude.**

### Stability and reproducibility

The coefficients of variation of the signal stability assessments are reported in Table 2. The average CV in the medial condyle was 2.00%, average CV in the lateral condyle was 2.25% and the average CV in the trochlea was 1.40%. Figure 2 shows an example of a fitted CEST spectrum, with the GAG, water and MT pools visualized in purple, light blue and dark blue, respectively. The GAG effect can be observed at the expected offset around 0.9 ppm.

**Table 2: Stability assessments of GAG effect at 0.9 ppm in healthy volunteers**

Subject	Age	Gender	Scan	Medial CV (%)	Trochlea CV (%)	Lateral CV (%)
1	21	F	1	1.61	0.88	1.23
			2	1.67	2.07	1.11
2	29	M	1	0.89	0.52	2.89
			2	1.25	0.52	0.73
3	35		1	3.2	1.96	1.74
			2	5.44	2.96	3.34
4	21	F	1	1.64	1.55	6.57
			2	1.54	0.57	0.88
5	25	F	1	1.08	1.54	1.49
			2	1.67	1.38	3.54
Mean coefficient of variation				2.00	1.40	2.25

**Figure 2: An example of CEST spectrum and its three pool Lorentzian decomposition. The black line shows the multi-Lorentzian fit of the three pools, acquired data is represented with black dots.**

The correlation plots in Figure 3 show strong reproducibility in the lateral condyle (ICC = 0.97,  $p < 0.01$ ) and the medial condyle (ICC = 0.87,  $p < 0.01$ ). The ICC for the trochlear groove was weak (0.064,  $p = 0.43$ ). Bland-Altman plots of the medial condyle and the lateral condyle are shown in Figure 4. Bland-Altman analysis was not carried out in the trochlear groove because of the poor ICC. The Bland-Altman analyses show that there is no proportional bias between the two measurements.

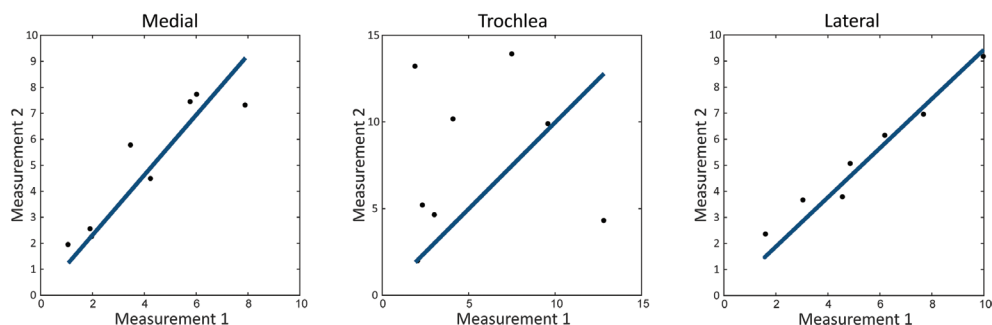


**Figure 3: the correlation graphs of three assessed locations (medial condyle, lateral condyle and trochlear groove). ICC medial condyle: 0.87 ( $p = 0.0049$ ), ICC trochlear groove: 0.063 ( $p = 0.43$ ) and ICC lateral condyle: 0.97 ( $p < 0.001$ ). Measurement 1 refers to the amplitude of the GAG fit in the first measurement, measurement 2 refers to the amplitude of the GAG fit in the second measurement.**

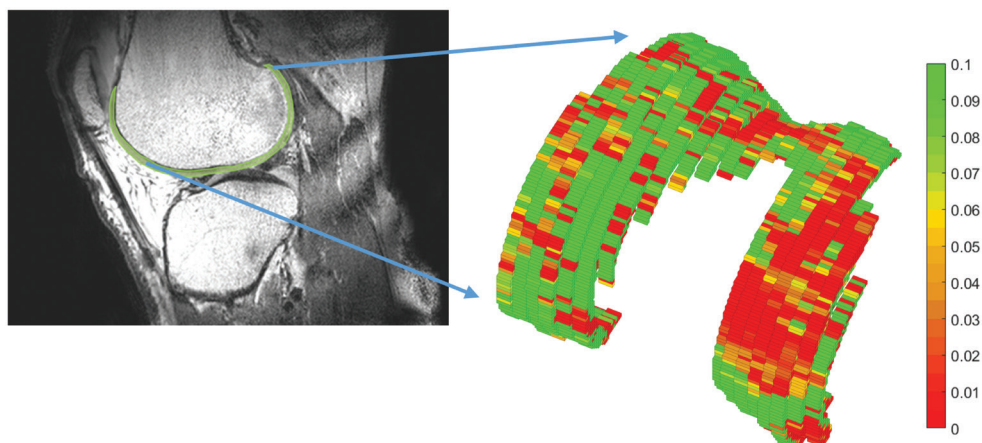


**Figure 4: 3D segmented GAG map of articular cartilage in the knee of a patient with an ICRS grade IV defect on the medial side of the knee.**

### Clinical applicability

A 3D segmented model of knee cartilage of a patient is shown in Figure 5. A difference in GAG effect in this patient was observed between the medial side and the lateral side. This specific patient had a ICRS grade IV defect in the medial condyle, which corresponds with the gagCEST findings.

An arthroscopic view of this patient and corresponding 3D gagCEST map is visualized in figure 6. The ICRS grades and GAG effects of all patients are summarized in Table 3. The ICRS grade ranged from 3 to 4 (> 50% thickness defects to full thickness cartilage defects). The GAG effect of healthy cartilage ranged from 2.6% to 12.4% and the GAG effect of damaged cartilage ranged from 1.3 to 5.1%. The GAG effect in damaged cartilage was significantly different ( $p < 0.05$ ) from healthy cartilage.



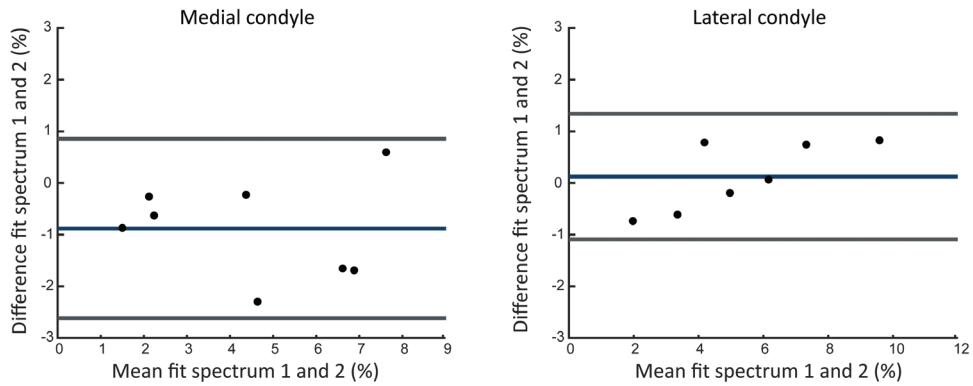


Figure 5: Bland-Altman plots of GAG effects in the medial condyle and the lateral condyle.

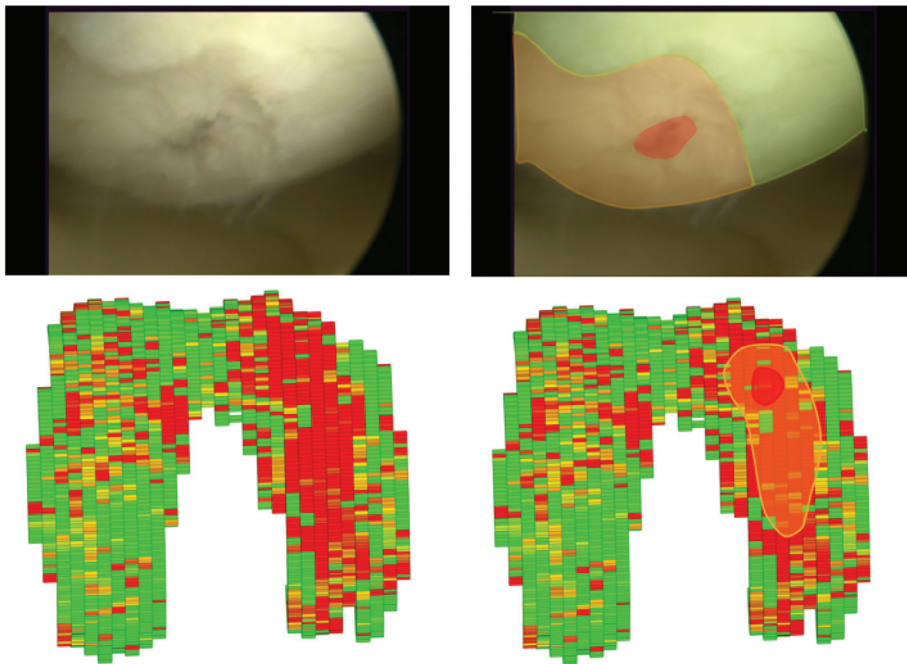


Figure 6: Comparison of arthroscopic view and gagCEST map. Left upper corner shows arthroscopic view of the knee of patient #1. The defect (red) and corresponding defect rim (orange) are highlighted in the image on the upper right. The lower left shows the gagCEST map of this patient, where the defect is clearly visualized. The same regions are highlighted again, with in red the defect and in orange the defect rim.

**Table 3: Comparison of GAG effect in cartilage repair patients: comparison of cartilage on damaged side of the knee versus cartilage on the healthy side of the knee. Difference between groups is statistically significant ( $p < 0.05$ ).**

#	Age (years)	BMI (kg/m <sup>2</sup> )	ICRS grade	Defect location	Defect size (cm <sup>2</sup> )	Defect origin	GAG effect healthy condyle	GAG effect defect condyle
1	38	21.1	4	MFC	3	No trauma, gradual increase of pain	12.0 (5.7 – 21.2)	5.1 (0.1 – 11.8)
2	21	22.5	4	LFC	2	Distortion trauma	12.4 (5.0 – 21.6)	1.3 (0 – 7.5)
3	25	23.0	3	LFC	1.5	Cartilage damage after removal of meniscal lesion	9.3 (2.2 – 20.1)	1.8 (0 – 8.8)
4	41	29.5	4	MFC	4	Distortion trauma	2.6 (0 – 11)	2.5 (0 – 9.7)
5	26	22.9	4	LFC	1.5	Rotational trauma	3.7 (0.2 – 10.8)	1.4 (0 – 7.3)

MFC = Medial Femoral Condyle; LFC = Lateral Femoral Condyle; GAG effect is expressed as a median and interquartile range.

## Discussion

This study presents a fast 3D gagCEST sequence with full cartilage coverage which can quantify the GAG effect in healthy volunteers and patients. The data is acquired within seven minutes and was shown to be stable and reproducible. Moreover, the method could differentiate healthy cartilage from damaged cartilage in patients before their cartilage repair surgery.

The main goal of this study was to present a fast 3D gagCEST sequence. The acquisition time for the gagCEST sequence used in this study was 6 minutes and 59 seconds, because a pseudo-steady state sequence was applied with an optimized number of saturation pulses. Other 3D sequences were published with scan times ranging from 11 minutes<sup>121</sup> to almost 15 minutes<sup>48</sup>. The latest study of the group of Trattnig reported a scan time of 19 minutes, albeit with a better resolution compared to our study<sup>122</sup>. Note that a higher resolution reduces signal to noise and is more prone to artifacts related to motion of the knee. All sequences published used the same number or comparable number of offsets and comparable field of view. We chose to implement an in-plane resolution of 1 x 1 mm<sup>2</sup> to minimize partial volume effects in the directions with most curvature of the cartilage. This comes with the drawback that the slice thickness needed to be 3 mm in order to achieve sufficient SNR. Several other 3D gagCEST studies also implemented a comparable slice thickness of 3 mm<sup>44,48</sup> or 5 mm<sup>129</sup>. An isotropic voxel-size would be more ideal for 3D visualization purposes, but this can only be achieved with a lower in-plane resolution or with much longer scan times.

This sequence was optimized using Bloch-McConnell simulations. Our goal was to minimize the scan time, which could lead to sub-optimal CEST effect size. The number of pulses in the prepulse train could be increased to 60 for optimal effect size, as shown in Figure 1A. However, this would increase the shot time to 5.4 seconds, which increases the acquisition time per offset with 8 seconds. This increase of 20% in effect size (8% to 10%) would lead to a 40% increase in total scan time (6:59 to 9:54). In our study we did not increase the scan time and selected a  $B_{1+}$  field amplitude of 2  $\mu$ T and DC of 70% to obtain the maximum achievable effect size of 8%.

We applied a Lorentzian fitting algorithm for quantification of GAG effect. We chose Lorentzian fitting to achieve better discrimination between the water peak and the metabolite peak, in this case GAG. Because we expect GAG to resonate at 0.9 ppm<sup>47</sup>, which is only 270 Hz upfield from the water peak, Lorentzian fitting was chosen. Lorentzian fitting also decreases the influence of  $B_0$  inhomogeneities<sup>130</sup>. Previous literature used MTR asymmetry as a method for quantification, which is prone to these  $B_0$  inhomogeneities<sup>44,48</sup>. We used WASSR to correctly center all CEST spectra as recommended by previous gagCEST studies<sup>131</sup>.

The reproducibility in the lateral and medial femoral condyles was very good, which is promising for implementation in clinical practice. However, one should notice the poor reproducibility in the trochlear groove. The reproducibility in the trochlea was much lower compared to the condyles, which was also shown at 7T in a study from Schreiner and colleagues<sup>122</sup>. The area around the trochlear groove is prone to movement of the patella. We speculate that this movement could be the cause of the poor reproducibility of the CEST spectra and their respective fits. Larger muscles could lead to more muscle twitches which ultimately leads to movement of the structures attached to the muscle, in this case the patella. The poor reproducibility could possibly be explained by this phenomenon. In addition, a 3 mm slice thickness could lead to volume averaging with surrounding tissue, especially in tissue with a high curvature such as the trochlea. Another limitation of this study is that measurements were only done on severe defects (ICRS grade III or IV) and healthy cartilage (ICRS grade 0). Because of the small population and the inclusion criteria for cartilage repair surgery in this study, no other defects were observed and gagCEST values of mild cartilage defects (ICRS grade I-II) are absent.

The GAG effect value is varying across the included healthy volunteers and patients. The range of GAG effect values is rather large in patients, healthy cartilage ranging from 2.6% to 12.4%, compared with 1.3% to 5.1% for damaged cartilage. A similar range is observed in healthy volunteers (1.6% to 13.9%), which raises the question if every volunteer had completely healthy cartilage. These ranges could indicate that there are underlying factors which affect the GAG effect, for instance age, gender

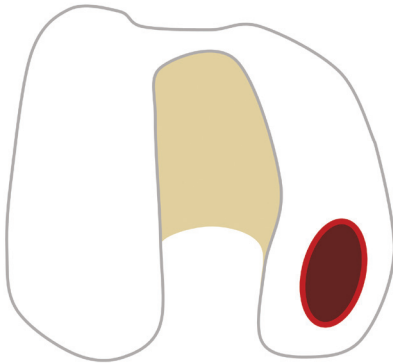
## Chapter 5

or BMI, as has been suggested in other studies<sup>132,133</sup>. Due to possible confounding effects of these factors, we chose not to compare the gagCEST values of patients with healthy volunteers.

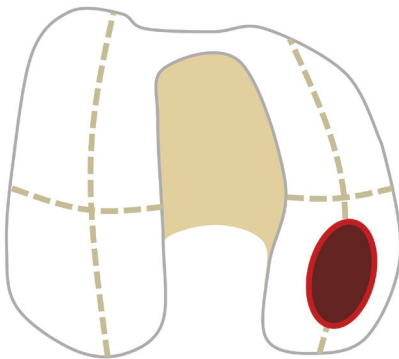
Detection of the range of GAG effect values could be an interesting tool for osteoarthritis research, for monitoring of disease but also for earlier diagnosis. Therefore, a next step in this research would be an analysis of GAG effect in patients with cartilage defects, ranging from small focal defects to osteoarthritic knees. This will reveal the value of gagCEST sequences in clinical practice and the patient characteristics affecting the GAG effect. In conclusion, this study presents a fast gagCEST sequence which is stable, reproducible and shows clinical value.

## Supplementary material

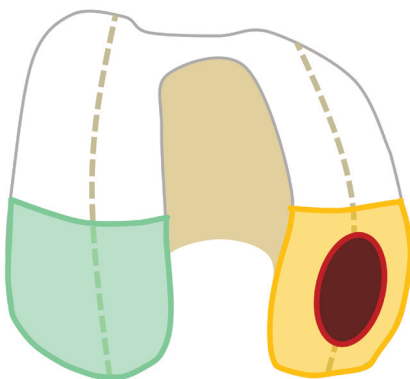
We chose to assess the defect location and the contralateral healthy location in a standardized way, to make sure we are not cherry-picking the results. In order to do this, we divide the condyle into four regions, as noted below. We select the quadrants in which the defect is located for the damaged side and select the same quadrants on the contralateral healthy side for comparison.



A: defect located on medial condyle



B: division of both condyles in four parts: superior-lateral, superior-medial, inferior-lateral and inferior-medial



C: defect is located in in two parts of the condyle: inferior-lateral and inferior-medial (visualized in orange). Same parts are used on contralateral healthy condyle to assess differences (visualized in green).

[illegible]

# In Vivo Cartilage Quantification with gagCEST MRI: Correlation with Cartilage Properties

S. Brinkhof<sup>1</sup>, R. Nizak<sup>2</sup>, S. Sim<sup>3</sup>, V. Khlebnikov<sup>1</sup>, E. Quenneville<sup>3</sup>,  
M. Garon<sup>3</sup>, D.W.J. Klomp<sup>1</sup>, D.B.F. Saris<sup>2,4,5</sup>

1. Department of Radiology, UMC Utrecht, Utrecht, the Netherlands
2. Department of Orthopaedics, UMC Utrecht, Utrecht, the Netherlands
3. Biomomentum Inc., Laval, Quebec, Canada
4. MIRA institute for Biomedical Technology and Technical Medicine, University of Twente, Enschede, the Netherlands
5. Department of Orthopaedics, Mayo Clinic, Rochester, Minnesota, United States

## Terms and abbreviations

DMMB	dimethylmethylene blue
GAG	glycosaminoglycans
gagCEST	glycosaminoglycan chemical exchange saturation transfer
MT	magnetization transfer
OA	osteoarthritis
QP	quantitative parameter
TKA	total knee arthroplasty



## Abstract

To assess articular cartilage *in vivo*, a non-invasive measurement is proposed to evaluate damage of the cartilage. It is hypothesized that gagCEST can be applied as a non-invasive imaging technique as it would relate to electromechanical indentation and GAG content as measured with biochemical assays. This pilot study applies gagCEST MRI in total knee arthroplasty (TKA) patients to assess substantially damaged articular cartilage. The outcome will be verified against electromechanical indentation and biochemical assays to assess the potential of gagCEST MRI. Five total knee arthroplasty patients were scanned on a 7.0T MRI with a gagCEST sequence. Articular resurfacing cuts after TKA were obtained for electromechanical and biochemical analyses. The gagCEST MRI measurements on the medial condyle show a moderate correlation with the GAG content, though, sensitivity on the lateral condyle is lacking. Additionally, a strong negative correlation of gagCEST MRI with the electromechanical measurements is observed in the regression analysis. Correlation of gagCEST MRI with electromechanical measurements was shown, demonstrating that gagCEST MRI could be a good indicator of GAG content in articular cartilage. In conclusion, gagCEST may be a valuable tool to assess the GAG content in articular cartilage non-invasively, although the mismatch in heterogeneity requires further investigation.

## Introduction

Early stage cartilage damage is characterized by changes in the integrity and biochemical composition of articular cartilage, mainly disorientation of the collagen fibers in the superficial zone of cartilage and loss of glycosaminoglycans (GAG) throughout the cartilage. The GAG content is of specific interest because it is useful for the joint, to withstand mechanical load by their hydrophilic capacities. Loss of GAG content leads to a decrease in stiffness of the articular cartilage and therefore a lower ability to withstand normal loads<sup>67,68</sup>. These changes can occur after trauma, during aging and/or during the course of degenerative joint diseases such as osteoarthritis (OA). The regenerative abilities of cartilage are virtually non-existent, which makes early identification of cartilage damage essential for a successful treatment<sup>1,87</sup>. To understand the development of cartilage damage and degeneration and identify possible treatment markers, measurements of these changes in biochemical composition are vital. These measurements can be carried out *ex vivo*, such as histological assessments, biochemical assays or biomechanical testing are measurements which are specific for biochemical composition in cartilage. However, they are invasive and destructive in nature and cannot be used *in vivo*.

Subtle changes in cartilage composition, in either healthy or damaged cartilage, can be visualized with quantitative MRI. The quantitative assessment of GAG content is a biomarker for early cartilage damage. Chemical Exchange Saturation Transfer (CEST) MRI is a promising technique for non-invasive evaluation of this GAG content in articular cartilage<sup>44,48,74,75</sup>. CEST can be used to monitor the GAG content in articular cartilage non-invasively, based on the chemical exchange of the labile hydroxyl protons of GAG with the bulk water. Recently, we have been able to show within a feasibility study that gagCEST MRI can clearly discriminate between healthy cartilage and damaged cartilage, with stable and reproducible measurements<sup>74</sup>.

Assessment of articular cartilage with quantitative MRI is not only necessary in diagnosis but is also of importance for treatment planning and monitoring. GagCEST could aid orthopaedic surgeons in the non-invasive pre- and post-operative assessment of cartilage. However, during surgery, orthopedic surgeons rely on their arthroscopic blunt probe to evaluate the cartilage, which is subject to interpretation.

Electromechanical indentation is a technique which can be used to assess the cartilage non-destructively *in vivo*. The probe is similar to an arthroscopic blunt probe but instrumented with an array of 37 microelectrodes on the surface of its hemispherical indenter. These microelectrodes measure streaming potentials induced through indentation which due to their molecular origins, are particularly sensitive to functional integrity of the collagen network and GAG content<sup>134,135</sup>. This technique

has shown to be correlated with destructive cartilage (quality) assessments such as histology, biochemistry and mechanical indentation<sup>136,137</sup>.

Implementation of a non-invasive measurement for quantitative assessment of cartilage *in vivo* has an added clinical value to either evaluate the damage, to plan treatment or to follow-up after treatment. GagCEST could be a valuable method to assess the cartilage for all these purposes, whereas electromechanical indentation can be used during surgery to precisely localize the lesion to be treated<sup>135,137</sup>. This pilot study aims to apply gagCEST MRI in total knee arthroplasty (TKA) patients to assess the articular cartilage. The outcome is consequently related with electromechanical indentation and biochemical assays to assess the potential of gagCEST MRI in clinical practice.

## Materials and methods

### Study workflow

This pilot study adheres to the Declaration of Helsinki, was approved by the institutional ethics review board (Medisch Ethische Toetsingscommissie Utrecht, protocol number 15/672D) and written informed consent was obtained from the participants. Five patients (aged 56 to 68, 2 males and 3 females) scheduled to undergo TKA were included in this study. Patients were selected within our specialized knee clinic of the University Medical Center Utrecht. The experiments were carried out on a 7.0T whole body scanner (Achieva; Philips Healthcare, Best, the Netherlands), using a volume transmit coil and a wrap-around 32-channel receiver knee coil (MR Coils BV, Zaltbommel, the Netherlands). Participants were scanned up to one day before their surgery. A 3D gagCEST sequence is used with 19 offsets, with an acquisition time of 6 minutes and 59 seconds and a resolution of  $1 \times 1 \times 3 \text{ mm}^3$ . The 3D gagCEST sequence entails a pre-saturation train of 20 sinc-shaped pulses ( $B_1 = 2 \text{ } \mu\text{T}$ , pulse length = 20 ms, duty cycle = 70%). The readout parameters were as follows: five-shot turbo field echo (TFE), TFE factor of 370, SENSE factor of 2, TR/TE/FA = 2.75ms/1.4ms/5 degrees, field of view  $140 \times 150 \times 135 \text{ mm}^3$  (covering the whole knee) and inter-shot T1 recovery time of 2 s. The sequence used is presented in earlier work<sup>74</sup>.

Femoral resurfacing cuts were collected for each TKA patient during surgery. The entire surface of these femoral weightbearing resurfacing cuts were mapped manually ex-vivo using a benchtop version of the electromechanical probe (Biomomentum Inc., Laval, QC, Canada), measuring streaming potentials induced from the compression of articular cartilage<sup>136</sup>. The output is the quantitative parameter (QP, A.U.) corresponding to the number of microelectrodes in contact with the articular cartilage when the sum of the streaming potentials is 100mV. The QP is thus inversely

proportional to the electromechanical response of the articular cartilage. This indicates that a low QP corresponds to strong electromechanical properties and high load-bearing characteristics, whilst a high QP is defined by signs of cartilage degeneration <sup>136</sup>. Recently, a new output of the electromechanical probe has been developed. This electromechanical grading system allows assessment of cartilage quality quantitatively <sup>138</sup> where the electromechanical QP (defined on a 0-37 scale) was translated into an electromechanical grade (defined on a 0-4 scale), a grade analogous to the ICRS grade. A position grid was overlaid through camera-registration software (Mapping Toolbox; Biomomentum Inc., Laval, QC, Canada) to guide through the manual electromechanical assessment of femoral cuts. The hemispherical indenter of the electromechanical probe was then rapidly compressed onto the cartilage surface (<1 second) and the electromechanical QP and electromechanical grade were recorded at each position of the grid.

After electromechanical indentation mapping, the cartilage samples (1x1 cm<sup>2</sup>) were taken from the resurfacing cuts and processed for biochemical analyses, by means of a dimethylmethylene blue (DMMB) assay to quantify the GAG weight in the samples <sup>139</sup>. The locations for biochemical analyses (blue squares) are shown in the graphical overview of femoral articular cartilage in figure 1.

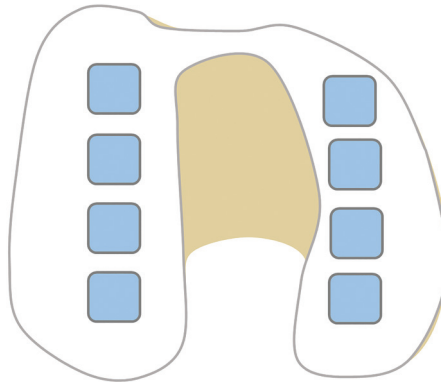


**Figure 1: Axial view of the knee. Overview of the cartilage samples (blue squares). Eight cartilage samples were taken for DMMB assay, four in each femoral condyle.**

Each distal condyle had four standardized sample locations for DMMB analyses, adding up to eight per knee, totaling up to 40 samples (though, not every sample location had enough cartilage to be included for further analyses). Additionally, DMMB analyses were also carried out on two standardized sample location for each posterior condyle, adding up to 20 extra samples in total. These samples were specifically used within the analyses of DMMB values versus gagCEST values. All samples were weighted before papain digestion solution (250 ug/mL papain, Sigma-Aldrich) was added for sample digestion by incubation overnight at 60 degrees

Celsius. The digested samples were diluted in PBS and stained with DMMB staining solution. The total amount of GAGs was measured photospectrometrically by dividing the extinction at 525 nm by the extinction at 595 nm. The GAG concentration per wet weight was used in the data analysis. A graphical overview of the study procedures is presented in figure 2.

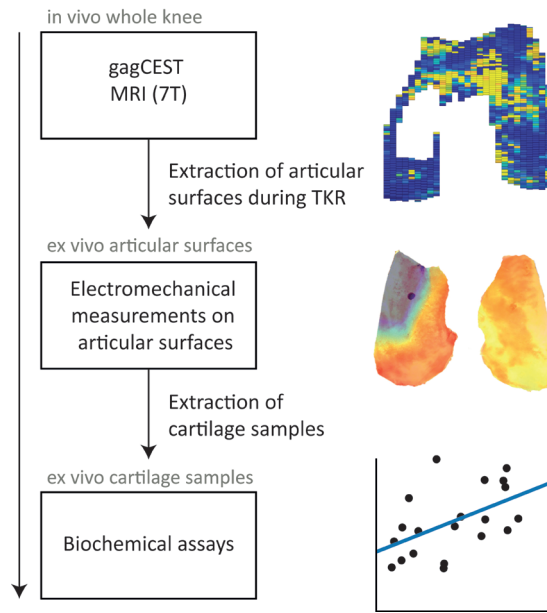


**Figure 2: overview of study procedures**

## Data analysis

The gagCEST MRI data is manually co-registered to the biochemistry locations using the pre-surgical MRI planning for patient-specific TKA planning (Visionaire; Smith & Nephew, Inc, Memphis, TN, USA). Using this information, the exact locations of the biochemical measurements and electromechanical measurements are registered and correlated with the gagCEST MRI values. The MRI data is corrected for B0 inhomogeneities and consequently normalized, whereafter a three-pool Lorentzian fit is carried out. The amplitude of the GAG pool is hereafter used as the outcome measure. Within this three-pool Lorentzian fit a separate fit is carried out for GAG, water and magnetization transfer (MT) effect. Possible effects of collagen in the articular cartilage reside in the MT effect and by fitting this separately there is no interference with the GAG pool. The registration and subsequent data analysis were performed in MATLAB (R2016b, the MathWorks, Natick, MA, USA) with in-house developed processing scripts.

### Statistical analysis

The cartilage samples were assumed to be independent, since we analyze a measurement for cartilage quality assuming to be independent for patient specific characteristics. The cartilage samples are therefore used as independent from one another in the analysis. The analysis is carried out in a three-step approach, where the first step is a general performance assessment – whether gagCEST can observe differences in GAG content between medial and lateral condyles. To achieve this, average gagCEST values are calculated per condyle with their respective ranges. The second step is an assessment on a sample-by-sample basis, where the data is divided between medial and lateral samples. The correlation between gagCEST values and GAG content as measured by DMMB is assessed by a linear mixed model, with patient as a random effect. The third and final step is a regression analysis between the electromechanical gradings (which are sampled on a finer grid, with about 110 datapoints in total) and the respective gagCEST values on those corresponding locations.

### Results

Ten cartilage sample locations were excluded due to complete denudation of the bone and one sample location had just one voxel in cartilage depth on MRI and was excluded as well to avoid partial voluming effects. Figure 3 shows gagCEST MRI maps (top row), corresponding QP maps (middle row) and corresponding electromechanical maps (bottom row) both superimposed on the femoral resurfacing cuts resulting from the electromechanical analyses. As an example, the data of T02 shows full-thickness cartilage loss on the medial condyle (exposed bone) but also very degraded cartilage, which is visible in the gagCEST MRI as dark blue or empty (since there is no cartilage), orange/red in the QP map and red/black in the electromechanical grade map. Some parts of the gagCEST map are empty, which correspond with parts where a complete denudation of bone was present (i.e. no cartilage).

Figure 4 shows the average gagCEST values per condyle, showing a higher gagCEST value in every lateral condyle compared to the corresponding medial condyle (gagCEST effect of 12.41% in the lateral condyle versus 9.95% in the medial condyle). The complete denudation of the medial condyle is the reason of lacking data in figure 3 for T02. This figure shows that the expected trend of a higher gagCEST effect in the lateral condyle compared to the medial condyle holds.

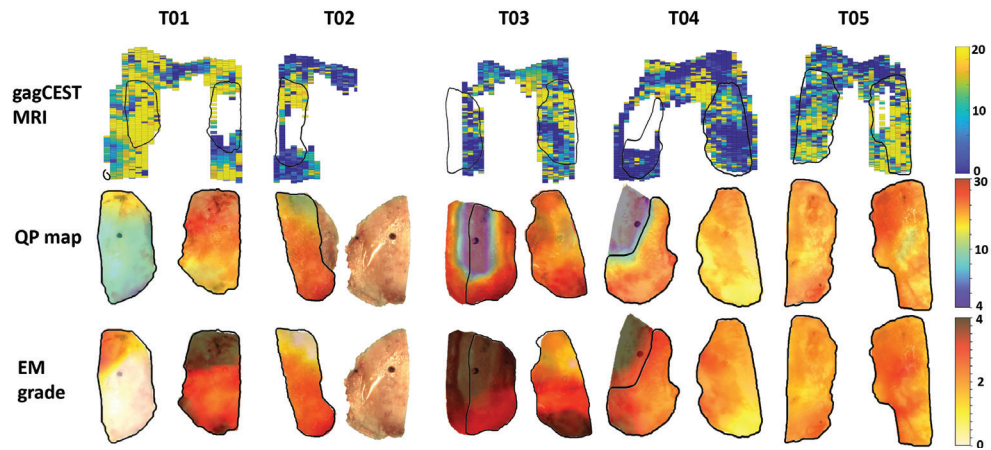


Figure 3: gagCEST MRI maps (upper row), articular resurfacing cuts with QP maps superimposed (middle row) and articular resurfacing cuts with electromechanical (EM) maps superimposed (bottom row). The outlines of the articular resurfacing cuts are shown on the gagCEST MRI map with the black lines.

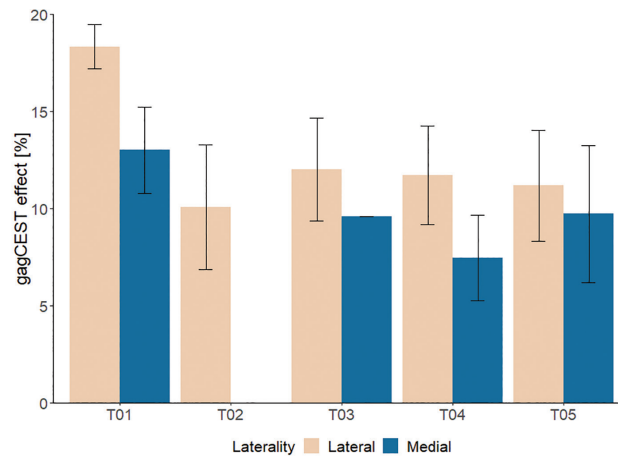
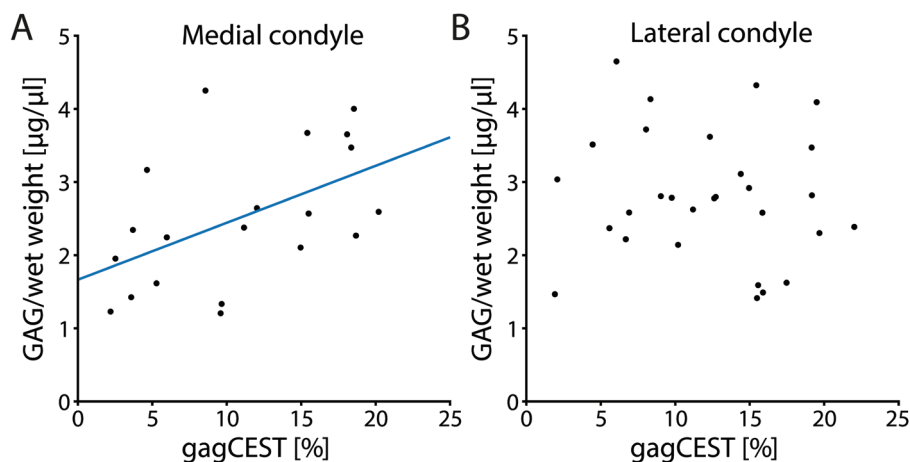


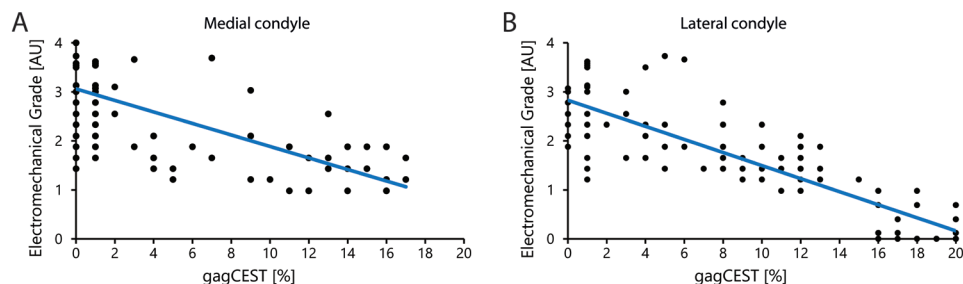
Figure 4: Average gagCEST MRI values per condyle (medial versus lateral) in every patient. Average medial gagCEST effect of 9.95% and average lateral gagCEST effect of 12.41%

Figure 5 shows the correlation of gagCEST with corresponding DMMB values of the medial (left pane) and lateral condyles (right pane). Whereas the medial values show a clear trend towards correlation of gagCEST with GAG per wet weight ( $p = 0.05$ ), the lateral values do not show this trend ( $p = 0.47$ ).



**Figure 5: Correlation graphs of GAG concentration as measured by DMMB and gagCEST MRI. On the left, all data points of the medial condyle are plotted including the trendline ( $r = 0.51$ ,  $p = 0.05$ ). On the right, all data points of the lateral condyle are plotted, which show no clear trend ( $p = 0.47$ ).**

GagCEST MRI shows to be related with the electromechanical grade, as shown in figure 6. Figure 6 is divided into the medial datapoints (left pane) and the lateral datapoints (right pane), showing regression lines for all data points in the medial and lateral condyle respectively. Both result in a moderate to strong negative linear relationship (medial:  $r = 0.69$ ,  $R^2 = 0.47$ ; lateral:  $r = 0.88$ ,  $R^2 = 0.77$ ).



**Figure 6: Plot of the electromechanical grade versus gagCEST MRI of each measured data point. On the left, all data points of the medial condyle are graphed including the regression line ( $r = -0.69$ ,  $R^2 = 0.47$ ). On the right, similar for all data points of the lateral condyle ( $r = -0.88$ ,  $R^2 = 0.77$ ).**

## Discussion

This pilot study shows the possibilities of pre-operative cartilage quality assessment with gagCEST MRI and intra-operative cartilage quality assessment with an electromechanical probe. Pre-operative assessment with gagCEST on 7T MRI



shows a good correlation with the ex vivo assessment using the electromechanical probe. The regression analysis results in a strong negative relationship ( $r = -0.69$  for medial samples and  $r = -0.88$  for lateral samples) between gagCEST MRI and electromechanical grade indicating that gagCEST MRI, just like electromechanical grading, may be valuable for accurate quantification of cartilage.

However, we also observe a lack of sensitivity, which is especially visible in the lateral condyle. There is no correlation between gagCEST MRI and cartilage wet weight (as measured with DMMB) in the lateral condyle. A possible explanation for this lack of sensitivity is that the general assumption that cartilage on the lateral condyle should be better is not met. If we compare the results with our earlier feasibility study, excellent test-retest values (ICC of 0.97) were observed in the lateral condyle – meaning that the signal stability should not lead to errors<sup>74</sup>.

The GAG content might be lower in the lateral condyle in this patient group compared with a general elderly population, since these patients suffer from medial osteoarthritis. These patients often have varus knees (as is the case in four of five patients included in this study), which has an influence on the weight-bearing distribution. Non-weightbearing cartilage has lower GAG content<sup>140</sup>, which therefore might be a spoiling effect in this analysis.

In the process of aging, GAGs are lost in the superficial and middle layers of the cartilage<sup>141</sup>, and the GAG synthesis in general decreases<sup>142</sup>. When GAGs are lost in the cartilage and general cartilage volume is retained, a very low DMMB measurement could be the result. GAG quantification by means of DMMB is an absolute measurement of GAG content, though, normalized by the wet weight of the sample. This implicates that DMMB might not be able to capture the subtle variations in GAG content throughout the depth of the cartilage<sup>143</sup>. In general, DMMB analyses in OA patients can be difficult to carry out properly. Cartilage is very thin and often some bone will come loose as well, increasing the weight greatly but not increasing the GAG content. This can lead to misinterpretations of the DMMB analyses.

In the medial condyle, a moderate correlation of gagCEST MRI and DMMB-measured GAG content was observed. Other parameters/factors in the cartilage could interfere with the measured GAG effect by gagCEST MRI. Articular cartilage consists of about 10-15 percent of GAG (wet weight) and 60 percent of collagen (dry weight) of which the latter could in principle interfere with our gagCEST results<sup>1</sup>. Within our data analysis, we fit for magnetization transfer effects, where we expect the effects of the collagen to be visible. The effects of collagen are fitted separately, and therefore minimizing its effect on the gagCEST measurements.

Our data does show a lower GAG content measured with gagCEST compared with

healthy controls from our previous study<sup>74</sup>. This is in line with results of Krishnamoorthy et al, showing that OA patients have a lower GAG content in general on gagCEST MRI<sup>121</sup>. In addition, gagCEST MRI has also shown to be age dependent, elderly patients included in this study are expected to have a lower gagCEST measurement<sup>133</sup>. We do observe differences in gagCEST effect size per patient, indicating that the gagCEST effect size could not only be age dependent, but could also be gender and BMI dependent<sup>132,133</sup>. In a pilot study such as this one, those effects cannot be considered due to the small number of patients. In a study with a larger population size these effects should be considered and corrected for when possible.

A limitation of this study is the small sample size of severe OA patients, which only enables the assessment of cartilage damage of ICRS grade III and IV. In order to develop a specific tool which can be used as a biomarker, one should include early cartilage damage (ICRS grade I and II) as well<sup>144</sup>. Another limitation in this study is the manual co-registration of biochemistry locations with the gagCEST MRI and electromechanical measurements. Since every knee has its own shape and curvature, a standard map could not be used. Using the patient-specific saw guides planning leads to the most optimal results for manual co-registration. Regarding the shape and curvature of the knee, one has also to consider the possible partial volume effects present. This effect is even more pronounced in our patient group with OA, because of the already thinner cartilage. To minimize the influence of the partial volume effects, we chose to exclude the data consisting of one voxel in cartilage thickness on gagCEST MRI.

Higher resolution acquisition could lead to better mapping of spatial variation of the curvatures in cartilage. By using a semi-continuous wave gagCEST protocol with alternating subsets of amplifiers it is possible to overcome duty cycle limitations and RF signal droop effects to ultimately achieve a 1 mm isotropic resolution<sup>145</sup>. By using this higher resolution for further work the sensitivity of gagCEST, especially in regions such as the trochlea, is expected to improve significantly. The maximum duty cycle can also be traded in for a higher in-plane spatial resolution, which may give insight in laminar differences of GAG content in cartilage depth.

The electromechanical measurements correlate well with the gagCEST measurements. In patients with OA, GAG content decreases which leads to a loss of negatively charged molecules residing in the articular cartilage. Less pressure is therefore generated through the compression of articular cartilage, leading to a lower compression-induced streaming potential resulting in a higher QP value in degraded cartilage. The strong correlation of electromechanical measurements with GAG content measured with gagCEST MRI in this study confirms this hypothesis.

In general, the results of this pilot study demonstrate that non-invasive gagCEST MRI

might have the potential to be a good indicator of cartilage GAG content and its electromechanical properties. Though, there is still a lack of sensitivity, mainly in the lateral condyle. This lack of sensitivity warrants further investigation within a larger study setting, given that other parameters do suggest gagCEST may be promising for application in clinical practice.



# Summary and general discussion

## Summary

As our population ages, the prevalence of osteoarthritis (OA) is rising amongst other degenerative diseases<sup>19</sup>. Ever since we encountered OA, the quest has been set out to find a treatment for this degenerative disease. Generally, physicians recommend conservative treatment including pain relief. When this is no longer sufficient, joint replacement remains the only option. In order to find new treatments, for instance in the form of disease-modifying OA drugs (DMOADs), we must properly stage and classify the phenotype of OA. To facilitate the development of new treatments, sophisticated imaging of articular cartilage is required, besides just measuring thickness of the joint space. This could be achieved by biochemical quantitative MRI, which could assess the stage of cartilage damage (and OA) as well as trying to find new phenotypes for OA.

Younger patients have several treatments options available which are able to fill a defect in articular cartilage with newly formed fibrous cartilage in the case of microfracturing or even hyaline cartilage when using autologous chondrocyte implantation. The choice for optimal treatment is mainly driven on defect size – which is often poorly estimated on standard-of-care MRI. Standard morphological MRI can underestimate the defect size extremely (up to 70%<sup>29,30</sup>), which can lead to a change in treatment when assessing the knee during arthroscopy. Quantitative biochemical MRI could be the ideal partner in this case by giving insight in the cartilage quality - especially in the defect rim.

Both the younger population with cartilage defects and the elderly population with OA can benefit from proper assessment of their articular cartilage, for which we use 7T MR imaging in this thesis. In order to get new imaging techniques embedded in the clinic, a number of stages must be completed before a new technique reaches the patient. Ideally, one could start with a perfectly functioning MR, with a dedicated coil and validated sequences. Sadly, this fairytale world does not exist (yet). Therefore, we developed a double tuned proton-sodium knee coil for this purpose, which has been described in **chapter 2**. We showed that this double tuned proton-sodium coil can achieve excellent imaging quality, comparable with the best available commercial (proton) knee coil on the market, while also being able to produce high-quality sodium images. Once we had produced and validated this coil, the next step was to validate sequences for clinical use, but not before choosing the imaging targets. Within this thesis, the choice has been made to pursue two components of articular cartilage, being GAG content and collagen structure/content.

Upon target selection, the next phase towards clinical implementation of new sequences is *ex vivo* validation. We chose to validate our sodium scans in *ex vivo*

tibial plateaus of patients who underwent a total knee replacement. We hypothesized that apart from assessing the FCD we could use sodium imaging to measure stiffness of articular cartilage. This hypothesis of correlation of stiffness as measured with a tensile tester with sodium concentration as measured with our sodium coil could not be confirmed, though we showed that sodium concentration is related to the permeability of cartilage. The design and results of this work, including the (lack of) correlation with DMMB analyses, are shown in **chapter 3**. Within **chapter 4** we scaled these *ex vivo* experiments up from small cartilage samples to whole joint samples, in this case carpal joints of Shetland ponies. These Shetland ponies were part of a larger experiment which tested the effect of a blunt groove model and a sharp groove model. We used T2\* mapping to gain insight in the collagen fiber network of the cartilage in the healthy contralateral control sites and the grooved sites. With this technique we were able to show differences in average relaxation time between grooved and healthy cartilage – paving the way for implementation in patients to discriminate between healthy and damaged cartilage.

The following step after *ex vivo* validation is *in vivo* feasibility. We designed a feasibility study for gagCEST MRI, to assess the feasibility and potential of gagCEST MRI in a group of patients, in this case cartilage repair patients. We showed (**chapter 5**) that we could apply gagCEST MRI in a clinically feasible scanning time of seven minutes and demonstrated high stability, reproducibility and clinical applicability. Now that we showed the feasibility, we went one step further and tried to prove that gagCEST is able to measure what we expect it does: (early) cartilage damage. In **chapter 6**, we implemented a pilot study where we acquired gagCEST images from patients before TKA, whereafter we retrieved the cartilage resurfacing cuts to assess those with electromechanical indentation and biochemical assays. We showed that there is indeed a good correlation of gagCEST with electromechanical indentation, on both the lateral and medial condyle. The same correlation was shown for gagCEST with biochemical assays (DMMB), although the correlation on the lateral condyle is lacking.

Summarizing, this thesis shows the applicability of 7T MRI within imaging and quantification of articular cartilage in various stages of (technical) development. This thesis describes several steps which are needed to implement imaging protocols in clinical practice. These steps are *ex vivo* feasibility and validation, *in vivo* feasibility and finally *in vivo* validation and implementation.

## General discussion

One of the main questions which I asked myself during my PhD was: how to get these interesting, new techniques for imaging articular cartilage implemented in the

clinic? This process often starts with developing a technology, which can be an MRI sequence, a coil, a new scanner (such as the META scanner being developed in the UMC Utrecht). When this technology has been developed and built, we go into the validation phase. In the case of articular cartilage imaging, one could use cartilage samples of animals (such as horses or pigs) or human samples (retrieved after TKR). After this validation phase, the implementation can start in healthy volunteers and possibly in patients, in a (small) feasibility study. After the feasibility is shown and proven, a (large) patient study can be implemented. Within this thesis, we went through all the steps as listed above, but a large patient study was lacking. These large studies are now in process at the orthopaedics department and the rheumatology department.

Given the topic of quantitative cartilage assessment a number of choices have to be made: which component(s) of the cartilage to focus on and which technique to use for these selected component of choice? Two components are often targeted in imaging studies of articular cartilage in literature: collagen and glycosaminoglycans (GAGs)<sup>115,116</sup>. Starting with the latter, the first few studies targeting GAGs implemented delayed Gadolinium Enhanced MRI of Cartilage (dGEMRIC)<sup>117,118</sup>, to measure GAG content indirectly. This imaging protocol relies on the inversely proportional relationship of the negatively charged GAGs with a gadolinium-based contrast agent in cartilage (i.e. a higher uptake of contrast agent means lower GAG content and consequently the higher uptake means a shorter T1 relaxation time, since gadolinium is a T1-shortening contrast agent)<sup>72</sup>. An alternative without the need for contrast material is T1rho, making use of a spin-lock pulse to quantify interactions between motion-restricted water molecules with their local macromolecular environment. Though this technique has been applied often in articular cartilage, the results seem to vary<sup>39,75</sup>. Alternatively, sodium (<sup>23</sup>Na) MRI can measure the GAG content by means of measuring the sodium ions in the interstitial fluid in the cartilage<sup>4,76,120</sup>. Sodium counterbalances the negative charge of the sulfate and carboxyl groups of GAGs, which means that the measurement of sodium and GAG are proportional to one another. Lastly, a relatively new technique targeting GAGs directly by selective saturation of exchangeable protons became available (gagCEST). This technique uses RF pulses to selectively saturate exchangeable protons bound to GAGs, more specifically to their hydroxyl sidegroups. Because of a fast exchange regime, this saturation is transferred to the bulk water pool and is therefore measurable<sup>47</sup>.

The second component often targeted in studies imaging articular cartilage is the collagen network. The collagen orientation changes throughout the thickness of the cartilage, which makes it an interesting biomarker to assess changes within this orientation – which happens during the course of cartilage damage. Given this directional anisotropy one immediately thinks about diffusion imaging, a technique



which is able to visualize this anisotropy<sup>55</sup>, but can be difficult to implement. An alternative which can be implemented in high resolution, making it possible to visualize cartilage layers, is T2\* mapping. T2\* mapping is sensitive to the orientation of the collagen fiber network within the cartilage and more importantly zonal variations in the depth of the cartilage could be visualized by employing T2\* mapping<sup>101</sup>.

## Feasibility

Within this thesis, we chose to implement GAG content imaging with gagCEST and sodium MRI, whereas we went with diffusion weighted imaging and T2\* mapping for collagen structure imaging. We chose gagCEST for the reason that it can be implemented in high resolution and that recent studies showed that it can be used to assess cartilage repair<sup>44,146</sup>, which was our first patient population for which we wanted to apply this protocol. Sodium MRI was an interesting option because in theory two measures could be captured: the sodium content (and therefore GAG content) and possibly the stiffness of the cartilage. Though, our work in chapter 4 showed that we could not link stiffness of cartilage to sodium content – at least not in the very degraded osteoarthritic cartilage samples used in this work.

Naturally, not every protocol is successful in (clinical) practice. Our first call to analyze the collagen structure in articular cartilage was diffusion weighted MRI. The basic option would be apparent diffusion coefficient (ADC) maps, but the more ideal option diffusion tensor imaging (DTI), which would make it possible to assess the directionality of collagen fibers. The potential of diffusion imaging on 7T was shown by Raya et al, demonstrating the change of fractional anisotropy throughout the depth of the cartilage<sup>57</sup>. This potential was confirmed in *ex vivo* studies, for instance with work of Wang and colleagues, showing excellent DTI metrics of articular cartilage<sup>147</sup>. The extremely high spatial resolution of 45  $\mu\text{m}$  made it possible to track collagen fibers from the deep zone to superficial zone, which was confirmed by polarized light microscopy. Though, there are not much *in vivo* diffusion studies around in articular cartilage, questioning the feasibility in these very thin cartilage layers with a high curvature. A new technique was developed in the University Medical Center Amsterdam to implement diffusion imaging which could be feasible for 7T cartilage imaging called diffusion-prepared stimulated-echo turbo spin echo (DPsti-TSE<sup>148</sup>). The first few results were promising, which led to an abstract presented at the ISMRM Annual Meeting in Paris called "Depth dependence of diffusion in articular cartilage of the knee visualized at 7T", showing that a significant depth dependence of the ADC in cartilage layers can be observed in vivo on 7T with diffusion weighted imaging.

Given the promising nature of these results we continued with this line of research, but were not able to reproduce the results. One of the problems could be B1 inhomogeneity, given the TSE nature of this sequence. We confirmed later in the

process that the coil was responsible for poor B1 performance and therefore bad scan results - and the diffusion project was stalled for now. When the new coil, that is composed of multi-transmit coils so to provide uniform B1 fields, is finalized this should be one of the research lines to pursue when developing protocols analyzing the collagen architecture of articular cartilage. Our second option was to implement T2\* imaging, as shown in chapter 4, being sensitive to the orientation of the collagen fiber network.

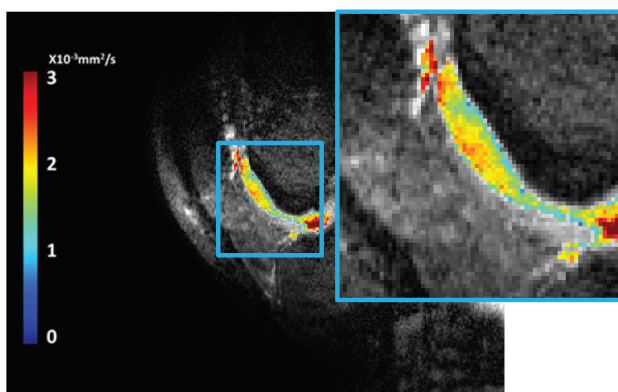


**Figure 1: depth dependence of ADC map in trochlea of a healthy volunteer, where the increase of ADC values can be appreciated from the bone-cartilage interface to the surface of the cartilage.**

## Validation

In order to get new imaging techniques embedded in the clinic one has to go through a validation phase, in which it is needed to know for sure whether the measurement is accurate and reproducible. The issue with reproducibility of quantitative biochemical imaging in articular cartilage is twofold; being the shape (high curvature) and movement, mostly of the patella. We suspect that these two are the reason that the reproducibility we found in our gagCEST feasibility study (chapter 6) was lower in the trochlea compared to the medial and lateral condyles. This does not come as a surprise, given the shape of the trochlea combined with a slice thickness of 3 mm. To top it off, there could be issues with movement of the patella in some of the offsets, which will add another noise factor to the measurement. One of the solutions is to improve the spatial resolution of the imaging protocol, in which we succeeded by using a parallel transmit setup, making it feasible to implement gagCEST in a 1mm isotropic voxelsize<sup>145</sup>. The improvements gained from this setup can also be used to achieve a higher in-plane resolution, depending on the application in which the gagCEST protocol will be used. These results will be brought into practice in the patient studies

carried out in the UMC Utrecht in combination with the newly developed knee coil.

Initial patient studies can be carried out after a successful validation phase, where differences between patients can be taken into account as well as variation within the joint. Within our patient study we saw some discrepancies when comparing the medial and lateral condyle, especially in the DMMB results. DMMB analyses are tough to carry out properly within highly degraded cartilage, because the cartilage which is left is often very thin and the underlying bone is degraded as well. When scraping off cartilage samples one easily includes some bone or parts of the calcified layer, increasing the overall weight of the sample but decreasing the (relative) amount of GAGs – spoiling the results with a too low GAG measurement. Additionally, at least in synovial fluid, DMMB analyses in end-stage OA seem to have two distinct categories: one with very high GAG content (possible active cartilage degeneration process) and one with very low GAG content (completely worn-out cartilage)<sup>97</sup>. These two causes could be the underlying factors of the lack of correlation of DMMB assays in the lateral condyle in chapter 6 or the samples used in chapter 3.

## Implementation

One of the issues with validation and implementation of cartilage assessment protocols on MRI often is the inclusion of subjects with early cartilage damage into clinical trials. In this thesis, most of the work has been done on OA patients (either induced OA in chapter 4 and end stage OA patients just before their joint replacement in chapter 6) and patients with cartilage defects (chapter 5). This means that in both cases the cartilage included in the trials will be ICRS grade III (defect >50% of thickness) or ICRS grade IV (full thickness defect). Ideally, patients with ICRS grade I and II defects would be subject of a clinical study. Svård and colleagues actually assessed ICRS grades I and II *in vivo* with T2 mapping showing differences in T2 relaxation time between ICRS grade 0 and I versus II on the medial condyle<sup>149</sup>. Though, this correlation was not found on all locations assessed, similarly as within our gagCEST patient study on severe cartilage defects. Often trials include healthy volunteers, as we did as well in our feasibility study of gagCEST in chapter 5. Though, healthy volunteers could in theory also have cartilage damage, which questions the validity of using so-called healthy volunteers. We also observed early cartilage damage on the healthy contralateral control joints of the Shetland ponies in chapter 4, though this could be induced due to the sham surgery.

Additionally, the validation and implementation of quantitative cartilage sequences could be troubled by the type of patients included. For instance, the gagCEST measurements can be influenced by age, gender and BMI<sup>132,133</sup>, which makes it important to include properly matched controls when comparing data with healthy volunteers. Within our feasibility study, we included matched controls based on those

factors, although the overall sample size was small.

Ideally, we want to implement these imaging protocols to assess early cartilage damage (ICRS grade I and II) in order to help patients earlier in the process when the solution can still be physiotherapy. Often the diagnosis is set in a later stage, diagnosing end stage OA or full thickness defects, where one has to undergo surgery (either joint replacement or cartilage replacement therapy) to fully “cure” their disease. To fully validate the potential added value of quantitative cartilage sequences large patient studies are necessary, although time-consuming and very costly. The larger studies to date are mostly carried out on clinical scanners, in order to make sure that most centers can fulfill the need for quantitative cartilage imaging. To fully unleash the potential, these studies will need to move to 7T scanners (or higher) to quantify cartilage to its full extent, with methods for instance presented in this thesis.

### Future prospects

A number of studies (morphological imaging<sup>150</sup>, T1rho mapping<sup>151</sup>, T2 mapping<sup>64,152</sup> and T2\* mapping<sup>64</sup>) try to port cartilage quality sequences to clinical field strengths such as 3T, which is excellent for part of the applications. Some quantitative MRI protocols even work better on 3T, for instance due to the longer T2 relaxation times for employing a T2 mapping protocol as shown by Juras and colleagues<sup>153</sup>.

Most of the academic centers will have ultra-high field scanners (7T, 9.4T or even higher) which have excellent applications for musculoskeletal research, due to the possibility for proper biochemical imaging or investing in ultra-high resolution. The same academic centers will be the referral centers for highly specialized cartilage treatments such as autologous chondrocyte implantation or even one-stage treatments such as the IMPACT trial carried out in the UMC Utrecht<sup>15</sup>. These highly specialized treatments are already followed in time by for instance T1rho imaging. These defects showed high T1rho values before surgery, which normalized to approximate the values of healthy cartilage 12 months post-surgery<sup>15</sup>. This example shows that quantitative cartilage sequences can work on 3T, but multiple examples in literature have shown that for at least the likes of sodium imaging and gagCEST a 7T MRI scanner is desired. Thus, the dedication to develop and implement new imaging techniques for assessment of articular cartilage should be on ultra-high field, because those ultra-high field scanners are available in (most) academic centers and these centers have the patient population to use in clinical studies (i.e. cartilage repair patients).

In contrast to these highly specialized treatments, most of the treatments carried out on OA patients (with a few examples here and there, such as the development of knee joint distraction techniques in the UMC Utrecht) will probably be done in top-

clinical and regional hospitals. These hospitals won't have access to ultra-high field scanners, at least not on a day-to-day basis, creating the need of cartilage quality assessments on 3T or even 1.5T. Therefore, the emphasis on going to clinical field strengths in these techniques should be on OA diagnosis and treatment stratification, which has also been described by the OARSI clinical trial recommendations for knee imaging (focus on improved detection, quantification and measurement performance of structural, compositional changes of hyaline and fibrocartilage)<sup>154</sup>. Large cohort studies around osteoarthritis imaging in Utrecht (Cohort Hip and Cohort Knee<sup>155</sup> and its successor APPROACH, carried out not only in Utrecht but also in A Coruna, Leiden, Oslo and Paris) were carried out on clinical scanners (1.5T and 3T), widening the application of cartilage imaging to not only academic centers but also regional hospitals. Although, an out of the box option for these centers could be a dedicated extremity scanner, which can be built on ultra-high field creating new, interesting possibilities for OA imaging.

One of the major remarks often seen in literature as well as in this work is that quantitative sequences for cartilage imaging often focus on one solitary component of the cartilage, it being the collagen structure, water content, FCD or GAG content. Often a lack of correlation is observed, due to variation in cartilage quality or sample quality or simply due to the fact that they were always measuring one component of the cartilage at a time. Thus, one of the results I would have liked to retrieve from the clinical studies is the possibility to create a composite model of multiple quantitative sequences. Within these clinical studies, we acquire gagCEST (GAG content), sodium imaging (FCD and GAG content) and T2\* imaging (collagen structure/water content) – giving rise to the possibility of quantification of every single component of cartilage. A next step could be the combination of these single components into one composite model, the ultimate quantification of cartilage quality. Not just one or two single components, but the quality of cartilage, being it healthy, early degraded or end stage OA – expressed in one number.



# Appendices

References

Nederlandse samenvatting

Dankwoord

List of publications

Curriculum vitae

## Appendices



## References

1. Fox, A. J. ., Bedi, A. & Rodeo, S. A. The Basic Science of Articular Cartilage: Structure, Composition, and Function. *Sports Health* **1**, 461–468 (2009).
2. Huber, M., Trattnig, S. & Lintner, F. Anatomy, biochemistry, and physiology of articular cartilage. *Invest. Radiol.* **35**, 573–580 (2000).
3. Han, E., Chen, S. S., Klisch, S. M. & Sah, R. L. Contribution of proteoglycan osmotic swelling pressure to the compressive properties of articular cartilage. *Biophys. J.* **101**, 916–924 (2011).
4. Wheaton, A. J. *et al.* Proteoglycan loss in human knee cartilage: quantitation with sodium MR imaging--feasibility study. *Radiology* **231**, 900–905 (2004).
5. Maroudas, A., Mizrahi, J., Katz, E. P., Wachtel, E. J. & Soudry, M. Physicochemical properties and functional behavior of normal and osteoarthritic human cartilage. in *Articular Cartilage Biochemistry* (ed. Keuttner, K.) 311–329 (Raven Press, 1986).
6. Maroudas, A. Balance between swelling pressure and collagen tension in normal and degenerate cartilage. *Nature* **260**, 808–809 (1976).
7. Heir, S. *et al.* Focal cartilage defects in the knee impair quality of life as much as severe osteoarthritis: A comparison of knee injury and osteoarthritis outcome score in 4 patient categories scheduled for knee surgery. *Am. J. Sports Med.* **38**, 231–237 (2010).
8. Brittberg, M. *et al.* ICRS Cartilage Injury Evaluation Package. *ICRS* 1–16 (2000). doi:papers3://publication/uuid/66E028C0-A295-4FE8-A270-02F51C233EA6
9. Steadman, J. R., Rodkey, W. G. & Rodrigo, J. J. Microfracture: surgical technique and rehabilitation to treat chondral defects. *Clin. Orthop. Relat. Res.* S362–9 (2001). doi:10.1097/00003086-200110001-00033
10. Gudas, R. *et al.* A prospective randomized clinical study of mosaic osteochondral autologous transplantation versus microfracture for the treatment of osteochondral defects in the knee joint in young athletes. *Arthrosc. - J. Arthrosc. Relat. Surg.* **21**, 1066–1075 (2005).
11. Mithoefer, K., Williams, R. J., Warren, R. F., Wickiewicz, T. L. & Marx, R. G. High-impact athletics after knee articular cartilage repair: a prospective evaluation of the microfracture technique. *Am. J. Sports Med.* **34**, 1413–8 (2006).
12. Gobbi, A., Karnatzikos, G. & Kumar, A. Long-term results after microfracture treatment for full-thickness knee chondral lesions in athletes. *Knee Surgery, Sport. Traumatol. Arthrosc.* **22**, 1986–1996 (2014).
13. Brittberg, M. *et al.* Treatment of deep cartilage defects in the knee with autologous chondrocyte transplantation. *N. Engl. J. Med.* **331**, 889–895 (1994).
14. Saris, D. B. F. *et al.* Treatment of symptomatic cartilage defects of the knee: characterized chondrocyte implantation results in better clinical outcome at 36 months in a randomized trial compared to microfracture. *Am. J. Sports Med.* **37 Suppl 1**, 10S–19S (2009).
15. Windt, T. S. de *et al.* Allogeneic MSCs and Recycled Autologous Chondrons Mixed in a One-Stage Cartilage Cell Transplantation: A First-in-Man Trial in 35 Patients. *Stem Cells* **35**, 1984–1993 (2017).
16. Gomoll, A. H., Farr, J., Gillogly, S. D., Kercher, J. & Minas, T. Surgical management of articular cartilage defects of the knee. *J. Bone Jt. Surg. - Ser. A* **92**, 2470–2490 (2010).
17. Bekkers, J. E. J., Inklaar, M. & Saris, D. B. F. Treatment Selection in Articular Cartilage Lesions of the Knee: A Systematic Review. *Am. J. Sports Med.* **37**, 148S–155S (2009).
18. Glyn-Jones, S. *et al.* Osteoarthritis. *Lancet* **386**, 376–387 (2015).
19. Madry, H., Luyten, F. P. & Facchini, A. Biological aspects of early osteoarthritis. *Knee Surgery, Sport. Traumatol. Arthrosc.* **20**, 407–422 (2012).
20. Nielen, M., Davids, R., Gommer, M., Poos, R. & Verheij, R. *NIVEL Zorgregistraties eerste lijn. Incidenties en prevalenties.* (2016).
21. Australian Orthopaedic Association. National Joint Replacement Registry, Hip and Knee Arthroplasty: annual report 2010. (2010).
22. Spruijt, S. *et al.* Knee joint distraction compared with total knee arthroplasty. *Bone Joint J.* **99-B**, 51–58 (2017).
23. van der Woude, J.-T. A. D. *et al.* Five-Year Follow-up of Knee Joint Distraction: Clinical Benefit and Cartilaginous Tissue Repair in an Open Uncontrolled Prospective Study. *Cartilage* **8**, 263–271

## Appendices

- (2016).
24. Kellgren, J. H. & Lawrence, J. S. Radiological Assessment of Osteo-Arthrosis. *Ann. Rheum. Dis.* **16**, 494–502 (1957).
  25. Alaia, M. J. *et al.* The utility of plain radiographs in the initial evaluation of knee pain amongst sports medicine patients. *Knee Surgery, Sport. Traumatol. Arthrosc.* 2213–2217 (2014). doi:10.1007/s00167-014-3003-8
  26. Barr, C. *et al.* MR imaging of the ankle at 3 Tesla and 1.5 Tesla: Protocol optimization and application to cartilage, ligament and tendon pathology in cadaver specimens. *Eur. Radiol.* **17**, 1518–1528 (2007).
  27. Peterfy, C. G. *et al.* Whole-organ magnetic resonance imaging score (WORMS) of the knee in osteoarthritis. *Osteoarthr. Cartil.* **12**, 177–190 (2004).
  28. Marlovits, S. *et al.* Magnetic resonance observation of cartilage repair tissue (MOCART) for the evaluation of autologous chondrocyte transplantation: Determination of interobserver variability and correlation to clinical outcome after 2 years. *Eur. J. Radiol.* **57**, 16–23 (2005).
  29. Gomoll, A. H., Yoshioka, H., Watanabe, A., Dunn, J. C. & Minas, T. Preoperative measurement of cartilage defects by MRI underestimates lesion size. *Cartilage* **2**, 389–393 (2011).
  30. Campbell, A. B. *et al.* Preoperative MRI underestimates articular cartilage defect size compared with findings at arthroscopic knee surgery. *Am. J. Sports Med.* **41**, 590–595 (2013).
  31. Bashir, A., Gray, M. L. & Burstein, D. Gd-DTPA2- as a measure of cartilage degradation. *Magn. Reson. Med.* **36**, 665–673 (1996).
  32. Bekkers, J. E. J. *et al.* Articular cartilage evaluation after TruFit plug implantation analyzed by delayed gadolinium-enhanced MRI of cartilage (dGEMRIC). *Am. J. Sports Med.* **41**, 1290–5 (2013).
  33. Brix, M. O., Stelzeneder, D., Trattnig, S., Windhager, R. & Domayer, S. E. Cartilage repair of the knee with Hyalograft C:® Magnetic Resonance Imaging assessment of the glycosaminoglycan content at midterm. *Int. Orthop.* **37**, 39–43 (2013).
  34. Besselink, N. J. *et al.* Cartilage Quality (dGEMRIC Index) Following Knee Joint Distraction or High Tibial Osteotomy. *Cartilage* 194760351877757 (2018). doi:10.1177/1947603518777578
  35. van Tiel, J. *et al.* Delayed Gadolinium-Enhanced MRI of Cartilage (dGEMRIC) Shows No Change in Cartilage Structural Composition after Viscosupplementation in Patients with Early-Stage Knee Osteoarthritis. *PLoS One* **8**, e79785 (2013).
  36. Owman, H., Tiderius, C. J., Neuman, P., Nyquist, F. & Dahlberg, L. E. Association between findings on delayed gadolinium-enhanced magnetic resonance imaging of cartilage and future knee osteoarthritis. *Arthritis Rheum.* **58**, 1727–1730 (2008).
  37. Borthakur, A. *et al.* Sodium and T<sub>1</sub>rho MRI for molecular and diagnostic imaging of articular cartilage. *NMR Biomed.* **19**, 781–821 (2006).
  38. Holtzman, D. *et al.* T(1p) and T(2) quantitative magnetic resonance imaging analysis of cartilage regeneration following microfracture and mosaicplasty cartilage resurfacing procedure. *J Magn Reson Imaging.* **32**, 914–923 (2010).
  39. van Tiel, J. *et al.* Is T1p Mapping an Alternative to Delayed Gadolinium-enhanced MR Imaging of Cartilage in the Assessment of Sulphated Glycosaminoglycan Content in Human Osteoarthritic Knees? An in Vivo Validation Study. *Radiology* **279**, 523–531 (2016).
  40. Madelin, G., Jerschow, A. & Regatte, R. R. Sodium relaxation times in the knee joint in vivo at 7T. *NMR Biomed.* **25**, 530–537 (2012).
  41. Trattnig, S. *et al.* Na-23 MR Imaging at 7 T after Knee Matrix-associated Autologous Chondrocyte Transplantation: Preliminary Results. *Radiology* **257**, 175–184 (2010).
  42. Shapiro, E. M., Borthakur, A., Gougoutas, A. & Reddy, R. 23Na MRI accurately measures fixed charge density in articular cartilage. *Magn. Reson. Med.* **47**, 284–291 (2002).
  43. Wang, L. *et al.* Rapid isotropic 3D-sodium MRI of the knee joint in vivo at 7T. *J. Magn. Reson. Imaging* **30**, 606–614 (2009).
  44. Krusche-Mandl, I. *et al.* Long-term results 8 years after autologous osteochondral transplantation: 7 T gagCEST and sodium magnetic resonance imaging with morphological and clinical correlation. *Osteoarthr. Cartil.* **20**, 357–363 (2012).
  45. Chang, G. *et al.* Improved assessment of cartilage repair tissue using fluid-suppressed 23Na inversion recovery MRI at 7 Tesla: Preliminary results. *Eur. Radiol.* **22**, 1341–1349 (2012).

46. de Bruin, P. W. *et al.* Time-efficient interleaved human  $^{23}\text{Na}$  and  $^1\text{H}$  data acquisition at 7 T. *NMR Biomed.* **28**, 1228–1235 (2015).
47. Ling, W., Regatte, R. R., Navon, G. & Jerschow, A. Assessment of glycosaminoglycan concentration in vivo by chemical exchange-dependent saturation transfer (gagCEST). *Proc. Natl. Acad. Sci. U. S. A.* **105**, 2266–2270 (2008).
48. Schmitt, B. *et al.* Cartilage Quality Assessment by Using Glycosaminoglycan Chemical Exchange Saturation Transfer and  $^{23}\text{Na}$  MR Imaging at 7 T. *Radiology* **260**, 257–264 (2011).
49. Ward, K., Aletras, A. & Balaban, R. A new class of contrast agents for MRI based on proton chemical exchange dependent saturation transfer (CEST). *J. Magn. Reson.* **143**, 79–87 (2000).
50. Vinogradov, E., Sherry, A. & Lenkinski, R. CEST: From basic principles to applications, challenges and opportunities. *J. Magn. Reson.* **229**, 155–172 (2013).
51. van Zijl, P. & Yadav, N. Chemical Exchange Saturation Transfer (CEST): What is in a name and what isn't? *Magn. Reson. Med.* **65**, 927–948 (2011).
52. de Visser, S. K., Crawford, R. W. & Pope, J. M. Structural adaptations in compressed articular cartilage measured by diffusion tensor imaging. *Osteoarthr. Cartil.* **16**, 83–89 (2008).
53. Maroudas, A. & Venn, M. Chemical composition and swelling of normal and osteoarthrotic femoral head cartilage. II. Swelling. *Ann. Rheum. Dis.* **36**, 399–406 (1977).
54. Ukai, T. *et al.* Diffusion tensor imaging can detect the early stages of cartilage damage: A comparison study. *BMC Musculoskelet. Disord.* **16**, 1–7 (2015).
55. Raya, J. G. *et al.* Change of diffusion tensor imaging parameters in articular cartilage with progressive proteoglycan extraction. *Invest. Radiol.* **46**, 401–409 (2011).
56. Deng, X., Farley, M., Nieminen, M. T., Gray, M. & Burstein, D. Diffusion tensor imaging of native and degenerated human articular cartilage. *Magn. Reson. Imaging* **25**, 168–171 (2007).
57. Raya, J. G. *et al.* Articular cartilage: in vivo diffusion-tensor imaging. *Radiology* **262**, 550–559 (2012).
58. Quirbach, S. *et al.* Initial results of in vivo high-resolution morphological and biochemical cartilage imaging of patients after matrix-associated autologous chondrocyte transplantation (MACT) of the ankle. *Skeletal Radiol.* **38**, 751–760 (2009).
59. Friedrich, K. M. *et al.* Diffusion-weighted imaging for the follow-up of patients after matrix-associated autologous chondrocyte transplantation. *Eur. J. Radiol.* **73**, 622–628 (2010).
60. Welsch, G. H. *et al.* Multimodal approach in the use of clinical scoring, morphological MRI and biochemical T2-mapping and diffusion-weighted imaging in their ability to assess differences between cartilage repair tissue after microfracture therapy and matrix-associated autolo. *Osteoarthr. Cartil.* **17**, 1219–1227 (2009).
61. Hesper, T. *et al.* T2\*-Mapping of Acetabular Cartilage in Patients With Femoroacetabular Impingement at 3 Tesla: Comparative Analysis with Arthroscopic Findings. *Cartilage* **9**, 118–126 (2018).
62. Lazik, A. *et al.* 7 Tesla quantitative hip MRI: T1, T2 and T2\* mapping of hip cartilage in healthy volunteers. *Eur. Radiol.* **26**, 1245–1253 (2016).
63. Hesper, T. *et al.* Quantitative T2\* assessment of knee joint cartilage after running a marathon. *Eur. J. Radiol.* **84**, 284–289 (2015).
64. Welsch, G. H. *et al.* Biochemical (T2, T2\* and magnetisation transfer ratio) MRI of knee cartilage: Feasibility at ultra-high field (7T) compared with high field (3T) strength. *Eur. Radiol.* **21**, 1136–1143 (2011).
65. Schütz, U. H. W. *et al.* Biochemical cartilage alteration and unexpected signal recovery in T2\* mapping observed in ankle joints with mobile MRI during a transcontinental multistage footrace over 4486km. *Osteoarthr. Cartil.* **22**, 1840–1850 (2014).
66. Van Ginckel, A. & Witvrouw, E. E. In vivo deformation of thin cartilage layers: Feasibility and applicability of T2\* mapping. *J. Orthop. Res.* **34**, 771–778 (2016).
67. Borthakur, A. & Reddy, R. Imaging Cartilage Physiology. *Top Magn Reson Imaging* **21**, 291–296 (2010).
68. Cohen, N. P., Foster, R. J. & Mow, V. C. Composition of Dynamics of Articular Cartilage: Structure, Function, and Maintaining Healthy State. *J. Orthop. Sport. Phys. Ther.* **28**, 203–215 (1998).
69. Schooler, J. *et al.* Longitudinal evaluation of T1 $\rho$  and T2 spatial distribution in osteoarthritic and

## Appendices

- healthy medial knee cartilage. *Osteoarthritis Cartilage* **22**, 51–62 (2014).
70. David-Vaudey, E., Ghosh, S., Ries, M. & Majumdar, S. T2 relaxation time measurements in osteoarthritis. *Magn. Reson. Imaging* **22**, 673–682 (2004).
71. Singh, A. *et al.* High Resolution T1p Mapping of In Vivo Human Knee Cartilage at 7T. *PLoS One* **9**, e97486 (2014).
72. Bekkers, J. E. J. *et al.* Delayed gadolinium enhanced MRI of cartilage (dGEMRIC) can be effectively applied for longitudinal cohort evaluation of articular cartilage regeneration. *Osteoarthr. Cartil.* **21**, 943–949 (2013).
73. Peterson, P. *et al.* Knee dGEMRIC at 7 T: comparison against 1.5 T and evaluation of T1-mapping methods. *BMC Musculoskelet. Disord.* **19**, (2018).
74. Brinkhof, S. *et al.* Detection of early cartilage damage : feasibility and potential of gagCEST imaging at 7T. *Eur. Radiol.* **28**, 2874–2881 (2018).
75. Kogan, F., Hargreaves, B. A. & Gold, G. E. Volumetric multislice gagCEST imaging of articular cartilage: Optimization and comparison with T1rho. *Magn. Reson. Med.* **77**, 1134–1141 (2016).
76. Reddy, R. *et al.* Sodium MRI of human articular cartilage in vivo. *Magn. Reson. Med.* **39**, 697–701 (1998).
77. Zbýň, Š., Mlynárik, V., Juras, V., Szomolanyi, P. & Trattnig, S. Sodium MR Imaging of Articular Cartilage Pathologies. *Curr. Radiol. Rep.* **2**, (2014).
78. Bottomley, P. A. Sodium MRI in human heart: A review. *NMR Biomed.* **29**, 187–196 (2016).
79. Shen, G. X., Boada, F. E. & Thulborn, K. R. Dual-Frequency, Dual-Quadrature, Birdcage RF Coil Design with Identical B1 Pattern for Sodium and Proton Imaging of the Human Brain at 1.5 T. *Magn. Reson. Med.* **38**, 717–725 (1997).
80. Wiggins, G. *et al.* A Nested Dual Frequency Birdcage/Stripline Coil for Sodium/Proton Brain Imaging at 7T. in *ISMRM 1500* (2010).
81. Brown, R. *et al.* A flexible nested sodium and proton coil array with wideband matching for knee cartilage MRI at 3T. *Magn. Reson. Med.* **76**, 1325–1334 (2016).
82. Grapperon, A. *et al.* Quantitative Brain Sodium MRI Depicts Corticospinal Impairment in Amyotrophic Lateral Sclerosis. *Radiology* **292**, 422–428 (2019).
83. Brownlee, W. J. *et al.* Cortical grey matter sodium accumulation is associated with disability and secondary progressive disease course in relapse-onset multiple sclerosis. *J. Neurol. Neurosurg. Psychiatry* **90**, 755–760 (2019).
84. Ianniello, C., Madelin, G., Moy, L. & Brown, R. A dual-tuned multichannel bilateral RF coil for <sup>1</sup>H/<sup>23</sup>Na breast MRI at 7 T. *Magn. Reson. Med.* mrm.27829 (2019). doi:10.1002/mrm.27829
85. Lanz, T., Kienlin, M. Von, Behr, W. & Haase, A. Double-tuned four-ring birdcage resonators for in vivo 31p nuclear magnetic resonance spectroscopy at 11.75 T. *MAGMA* **5**, 243–246 (1997).
86. Brown, R. W., Cheng, Y.-C. N., Haacke, E. M., Thompson, M. R. & Venkatesan, R. Appendix B.5 Rayleigh Distribution. in *Magnetic Resonance Imaging - Physical Principles and Sequence Design* 906–907 (Wiley Blackwell, 2014).
87. Bekkers, J. E. J., Creemers, L. B., Dhert, W. J. A. & Saris, D. B. F. Diagnostic Modalities for Diseased Articular Cartilage--From Defect to Degeneration: A Review. *Cartilage* **1**, 157–164 (2010).
88. Oakley, S. P. *et al.* Arthroscopy -- a potential 'gold standard' for the diagnosis of the chondropathy of early osteoarthritis. *Osteoarthritis Cartilage* **13**, 368–78 (2005).
89. Lai, W. M., Hou, J. S. & Mow, V. C. A Triphasic Theory for the Swelling and Deformation Behaviors of Articular Cartilage. *J. Biomech. Eng.* **113**, 245–258 (1991).
90. Madelin, G. *et al.* Articular Cartilage: Evaluation with Fluid-suppressed 7.0-T Sodium MR Imaging in Subjects with and Subjects without Osteoarthritis. *Radiology* **268**, 481–491 (2013).
91. Brinkhof, S., Ali Haghnejad, A., Ito, K., Markenroth Bloch, K. & Klomp, D. W. J. Uncompromised MRI of knee cartilage while incorporating sensitive sodium MRI. *NMR Biomed.* **32**, 1–9 (2019).
92. Farndale, R. W., Buttle, D. J. & Barrett, A. J. Improved quantitation and discrimination of sulphated glycosaminoglycans by use of dimethylmethylene blue. *BBA - Gen. Subj.* **883**, 173–177 (1986).
93. Kumar, R. *et al.* Comparison of compressive stress-relaxation behavior in osteoarthritic (ICRS graded) human articular cartilage. *Int. J. Mol. Sci.* **19**, (2018).
94. Baldassar, M. *et al.* Relationship between Cartilage Stiffness and dGEMRIC Index: Correlation

- and Prediction. *J. Orthop. Res.* 904–912 (2007). doi:10.1002/jor.20378
95. Samosky, J. T. *et al.* Spatially-localized correlation of dGEMRIC-measured GAG distribution and mechanical stiffness in the human tibial plateau. *J. Orthop. Res.* **23**, 93–101 (2005).
  96. Madelin, G. *et al.* Longitudinal Study of Sodium MRI of Articular Cartilage in Patients with Knee Osteoarthritis: Initial Experience with 16- Month Follow-Up. *Eur. Radiol.* **28**, 133–412 (2018).
  97. Kulkarni, P. *et al.* Glycosaminoglycan measured from synovial fluid serves as a useful indicator for progression of Osteoarthritis and complements Kellgren-Lawrence Score. *BBA Clin.* **6**, 1–4 (2016).
  98. Wang, C. *et al.* Validation of Sodium MRI of intervertebral disc. *Spine (Phila. Pa. 1976)*. **35**, 505–510 (2010).
  99. Zbýň, Š. *et al.* Sodium magnetic resonance imaging of ankle joint in cadaver specimens, volunteers, and patients after different cartilage repair techniques at 7 T: initial results. *Invest. Radiol.* **50**, 246–254 (2015).
  100. Hesper, T. *et al.* T2\* mapping for articular cartilage assessment: Principles, current applications, and future prospects. *Skeletal Radiol.* **43**, 1429–1445 (2014).
  101. Welsch, G. H. *et al.* In vivo biochemical 7.0 tesla magnetic resonance: Preliminary results of dGEMRIC, zonal T2, and T2\* mapping of articular cartilage. *Invest. Radiol.* **43**, 619–626 (2008).
  102. Lazik-Palm, A. *et al.* Morphological and quantitative 7 T MRI of hip cartilage transplants in comparison to 3 T-initial experiences. *Invest. Radiol.* **51**, 552–559 (2016).
  103. de Visser, H. M. *et al.* Groove model of tibia-femoral osteoarthritis in the rat. *J. Orthop. Res.* **35**, 496–505 (2017).
  104. Marijnissen, A. C. A. *et al.* Steady progression of osteoarthritic features in the canine groove model. *Osteoarthr. Cartil.* **10**, 282–289 (2002).
  105. Mastbergen, S. C., Pollmeier, M., Fischer, L., Vianen, M. E. & Lafeber, F. P. J. G. The groove model of osteoarthritis applied to the ovine fetlock joint. *Osteoarthr. Cartil.* **16**, 919–928 (2008).
  106. Maninchedda, U. *et al.* Development of an equine groove model to induce metacarpophalangeal osteoarthritis: A pilot study on 6 horses. *PLoS One* **10**, 1–18 (2015).
  107. Frisbie, D. D., Cross, M. W. & McIlwraith, C. W. A comparative study of articular cartilage thickness in the stifle of animal species used in human pre-clinical studies compared to articular cartilage thickness in the human knee. *Vet. Comp. Orthop. Traumatol.* **19**, 142–146 (2006).
  108. te Moller, N. C. R. Does cartilage damage doom the joint?: Diagnosis and impact of subtle cartilage defects in the (equine) joint. (Utrecht University, 2019).
  109. Newbould, R. D. *et al.* T2\* measurement of the knee articular cartilage in osteoarthritis at 3T. *J. Magn. Reson. Imaging* **35**, 1422–1429 (2012).
  110. Nykänen, O. *et al.* T2\* and quantitative susceptibility mapping in an equine model of post-traumatic osteoarthritis: assessment of mechanical and structural properties of articular cartilage. *Osteoarthr. Cartil.* **27**, 1481–1490 (2019).
  111. Marik, W., Apprich, S., Welsch, G. H., Mamisch, T. C. & Trattnig, S. Biochemical evaluation of articular cartilage in patients with osteochondrosis dissecans by means of quantitative T2- and T2\*-mapping at 3 T MRI: A feasibility study. *Eur. J. Radiol.* **81**, 923–927 (2012).
  112. Xia, Y., Moody, J. B. & Alhadlaq, H. Orientational dependence of T2 relaxation in articular cartilage: A microscopic MRI ( $\mu$ MRI) study. *Magn. Reson. Med.* **48**, 460–469 (2002).
  113. Hager, B. *et al.* Orientation dependence and decay characteristics of T2\* relaxation in the human meniscus studied with 7 Tesla MR microscopy and compared to histology. *Magn. Reson. Med.* **81**, 921–933 (2019).
  114. Mamisch, T. C. *et al.* T2 star relaxation times for assessment of articular cartilage at 3 T: A feasibility study. *Skeletal Radiol.* **41**, 287–292 (2012).
  115. Guermazi, A. *et al.* Compositional MRI Techniques for Evaluation of Cartilage Degeneration in Osteoarthritis. *Osteoarthr. Cartil.* **23**, 1639–1653 (2015).
  116. Trattnig, S. *et al.* Advanced MR methods at ultra-high field (7 Tesla) for clinical musculoskeletal applications. *Eur. Radiol.* **22**, 2338–2346 (2012).
  117. Bashir, A., Gray, M. L., Hartke, J. & Burstein, D. Nondestructive imaging of human cartilage glycosaminoglycan concentration by MRI. *Magn. Reson. Med.* **41**, 857–865 (1999).
  118. Trattnig, S. *et al.* MRI visualization of proteoglycan depletion in articular cartilage via intravenous administration of Gd-DTPA. *Magn. Reson. Imaging* **17**, 577–583 (1999).



## Appendices

119. Li, X. *et al.* In vivo T(1rho) and T(2) mapping of articular cartilage in osteoarthritis of the knee using 3 T MRI. *Osteoarthritis Cartilage* **15**, 789–797 (2007).
120. Shapiro, E. M. *et al.* Sodium visibility and quantitation in intact bovine articular cartilage using high field Na-23 MRI and MRS. *J. Magn. Reson.* **142**, 24–31 (2000).
121. Krishnamoorthy, G., Nanga, R. P. R., Bagga, P., Hariharan, H. & Reddy, R. High quality three-dimensional gagCEST imaging of in vivo human knee cartilage at 7 Tesla. *Magn. Reson. Med.* **77**, 1866–1873 (2017).
122. Schreiner, M. M. *et al.* Reproducibility and regional variations of an improved gagCEST protocol for the in vivo evaluation of knee cartilage at 7T. *Magn. Reson. Mater. Physics, Biol. Med.* **29**, 513–521 (2016).
123. Khlebnikov, V. *et al.* Comparison of pulsed three-dimensional CEST acquisition schemes at 7 tesla: steady state versus pseudosteady state. *Magn. Reson. Med.* **77**, 2280–2287 (2016).
124. McConnell, H. Reaction rates by nuclear magnetic resonance. *J. Chem. Phys.* **28**, 430–431 (1958).
125. Woessner, D., Zhang, S., Merritt, M. & Sherry, A. Numerical solution of the Bloch equations provides insights into the optimum design of PARACEST agents for MRI. *Magn. Reson. Med.* **53**, 790–799 (2005).
126. Brittberg, M. & Peterson, L. Introduction of an articular cartilage classification. *ICRS Newsl.* **5**:8 (1998).
127. Kim, M., Gillen, J., Landman, B. A., Zhou, J. & Van Zijl, P. C. M. Water saturation shift referencing (WASSR) for chemical exchange saturation transfer (CEST) experiments. *Magn. Reson. Med.* **61**, 1441–1450 (2009).
128. Zaiss, M., Schmitt, B. & Bachert, P. Quantitative separation of CEST effect from magnetization transfer and spillover effects by Lorentzian-line-fit analysis of z-spectra. *J. Magn. Reson.* **211**, 149–155 (2011).
129. Singh, A. *et al.* Chemical exchange saturation transfer magnetic resonance imaging of human knee cartilage at 3 T and 7 T. *Magn. Reson. Med.* **68**, 588–94 (2012).
130. Windschuh, J. *et al.* Correction of B1-inhomogeneities for relaxation-compensated CEST imaging at 7T. *NMR Biomed.* **28**, 529–537 (2015).
131. Schleich, C. *et al.* Glycosaminoglycan chemical exchange saturation transfer at 3T MRI in asymptomatic knee joints. *Acta radiol.* **57**, 627–632 (2016).
132. Müller-Lutz, A. *et al.* Gender, BMI and T2 dependencies of glycosaminoglycan chemical exchange saturation transfer in intervertebral discs. *Magn. Reson. Imaging* **34**, 271–275 (2016).
133. Müller-Lutz, A. *et al.* Age-dependency of glycosaminoglycan content in lumbar discs: A 3T gagCEST study. *J. Magn. Reson. Imaging* **42**, 1517–1523 (2015).
134. Garon, M., Légaré, A., Guardo, R., Savard, P. & Buschmann, M. D. Streaming potentials maps are spatially resolved indicators of amplitude, frequency and ionic strength dependant responses of articular cartilage to load. *J. Biomech.* **35**, 207–216 (2002).
135. Légaré, A. *et al.* Detection and analysis of cartilage degeneration by spatially resolved streaming potentials. *J. Orthop. Res.* **20**, 819–826 (2002).
136. Sim, S. *et al.* Non-destructive electromechanical assessment (Arthro-BST) of human articular cartilage correlates with histological scores and biomechanical properties. *Osteoarthr. Cartil.* **22**, 1926–1935 (2014).
137. Sim, S. *et al.* Electromechanical probe and automated indentation maps are sensitive techniques in assessing early degenerated human articular cartilage. *J. Orthop. Res.* **35**, 858–867 (2017).
138. Sim, S. *et al.* Development of an Electromechanical Grade to Assess Human Knee Articular Cartilage Quality. *Ann. Biomed. Eng.* **45**, 2422 (2017).
139. Dey, P., Saphos, C., McDonnell, J. & Moore, V. Studies on the quantification of proteoglycans by the dimethylmethylen blue dye-binding method. Specificity, quantitation in synovial lavage fluid, and automation. *Connect. Tissue Res.* **28**, 317–324 (1992).
140. Rogers, B. A., Murphy, C. L., Cannon, S. R. & Briggs, T. W. R. Topographical variation in glycosaminoglycan content in human articular cartilage. *J. Bone Joint Surg. Br.* **88-B**, 1670–1674 (2006).
141. Li, X. F. *et al.* Observation of sGAG content of human hip joint cartilage in different old age groups based on EPIC micro-CT. *Connect. Tissue Res.* **56**, 99–105 (2015).

142. Hickery, M. S. *et al.* Age-related changes in the response of human articular cartilage to IL-1 $\alpha$  and transforming growth factor- $\beta$  (TGF- $\beta$ ): Chondrocytes exhibit a diminished sensitivity to TGF- $\beta$ . *J. Biol. Chem.* **278**, 53063–53071 (2003).
143. Kuiper, N. J. & Sharma, A. A detailed quantitative outcome measure of glycosaminoglycans in human articular cartilage for cell therapy and tissue engineering strategies. *Osteoarthr. Cartil.* **23**, 2233–2241 (2015).
144. Link, T. M. Editorial comment : the future of compositional MRI for cartilage. (2018).
145. Brinkhof, S., Khlebnikov, V., Visser, F. & Hoogduin, H. High resolution 1 mm isotropic semi continuous wave gagCEST of articular cartilage using parallel transmit at 7T. *Proc. Intl. Soc. Mag. Reson. Med* **26**, 5191 (2018).
146. Koller, U., Apprich, S., Schmitt, B., Windhager, R. & Trattnig, S. Evaluating the cartilage adjacent to the site of repair surgery with glycosaminoglycan-specific magnetic resonance imaging. *Int. Orthop.* **41**, 969–974 (2017).
147. Wang, N. *et al.* Diffusion tractography of the rat knee at microscopic resolution. *Magn. Reson. Med.* **81**, 3775–3786 (2019).
148. Zhang, Q., Coolen, B. F., Versluis, M. J., Strijkers, G. J. & Nederveen, A. J. Diffusion-prepared stimulated-echo turbo spin echo (DPsti-TSE): An eddy current-insensitive sequence for three-dimensional high-resolution and undistorted diffusion-weighted imaging. *NMR Biomed.* **30**, 1–12 (2017).
149. Svärd, T. *et al.* Quantitative MRI of Human Cartilage In Vivo: Relationships with Arthroscopic Indentation Stiffness and Defect Severity. *Cartilage* **9**, 46–54 (2018).
150. Stahl, R. *et al.* Assessment of cartilage-dedicated sequences at ultra-high-field MRI: Comparison of imaging performance and diagnostic confidence between 3.0 and 7.0 T with respect to osteoarthritis-induced changes at the knee joint. *Skeletal Radiol.* **38**, 771–783 (2009).
151. Wyatt, C. *et al.* Improved differentiation between knees with cartilage lesions and controls using 7T relaxation time mapping. *J. Orthop. Transl.* **3**, 197–204 (2015).
152. Wyatt, C. *et al.* Improved differentiation between knees with cartilage lesions and controls using 7T relaxation time mapping. *J. Orthop. Transl.* **3**, 197–204 (2015).
153. Juras, V. *et al.* The comparison of the performance of 3 T and 7 T T2 mapping for untreated low-grade cartilage lesions. *Magn. Reson. Imaging* **55**, 86–92 (2019).
154. Hunter, D. J. *et al.* OARSI Clinical Trials Recommendations: Knee imaging in clinical trials in osteoarthritis. *Osteoarthr. Cartil.* **23**, 698–715 (2015).
155. Wesseling, J. *et al.* CHECK (Cohort Hip and Cohort Knee): Similarities and differences with the Osteoarthritis Initiative. *Ann. Rheum. Dis.* **68**, 1413–1419 (2009).

## Appendices



## Nederlandse Samenvatting

De prevalentie van degeneratieve ziekten zoals artrose neemt toe door de vergrijzing van onze bevolking. Hierdoor is de zoektocht opgezet naar een behandeling voor deze degeneratieve ziekte. Patiënten met artrose hebben last van stijfheid en pijn in hun gewrichten, wat onder andere komt door schade aan het kraakbeen. Tot nu toe zijn we meestal beperkt tot conservatieve behandeling en pijnverlichting, waarna we in het eindstadium een gewricht kunnen vervangen wanneer deze conservatieve behandeling niet meer afdoende is. Om nieuwe behandelingen te vinden, bijvoorbeeld in de vorm van artrose geneesmiddelen, moeten we het artrose en al zijn subtypen op de juiste manier stadiëren en classificeren. Om dat te kunnen doen hebben we geavanceerde beeldvorming van het kraakbeen nodig, omdat het meten van alleen de dikte van het kraakbeen niet voldoende is. Biochemische, kwantitatieve MRI kan helpen om het stadium van kraakbeenschade (en artrose) te beoordelen en nieuwe subtypen voor artrose te vinden.

Gelukkig zijn voor jongere patiënten verschillende behandelingen beschikbaar. Deze behandelingen kunnen een defect vullen met nieuw gevormd fibreus kraakbeen in het geval van een microfracturing, of zelfs hyaline kraakbeen bij gebruik van autologe chondrocyten implantatie. De behandelkeuze voor een van deze therapieën is voornamelijk gebaseerd op de grootte van het defect, die vaak slecht wordt geschat op standaard MRI. Standaard anatomische MRI kan de defectgrootte extreem onderschatten (tot 70%), wat kan leiden tot een verandering in de behandelkeuze bij het beoordelen van de knie tijdens artroscopie. Kwantitatieve biochemische MRI zou in dit geval de ideale oplossing kunnen zijn doordat deze op voorhand inzicht geeft in de kraakbeenkwaliteit.

Zowel de jongere populatie met kraakbeendefecten als de oudere populatie met artrose kunnen baat hebben bij een goede beoordeling van hun kraakbeen, waarvoor we 7T MRI-beeldvorming gebruiken in dit proefschrift. Om nieuwe beeldvormingstechnieken in de kliniek te krijgen, moeten er een aantal fasen doorlopen worden voordat een nieuwe techniek de patiënt bereikt. Idealiter zou dit onderzoek beginnen met een perfect functionerende MRI, met een geavanceerde kniespoel en gevalideerde MRI-sequenties. Helaas was dit (nog) niet het geval. Daarom hebben we voor dit doel een dubbel-resonante proton-natrium kniespoel ontwikkeld, die in hoofdstuk 2 is beschreven. We hebben aangetoond dat deze dubbel-resonante proton-natrium kniespoel een uitstekende beeldkwaliteit geeft, vergelijkbaar met de best beschikbare commerciële (proton) knie spoel op de markt, terwijl deze kniespoel ook natriumbeelden van hoge kwaliteit kan maken.

Na de productie en validatie van deze kniespoel is de volgende stap het valideren van

## Appendices

sequenties voor klinisch gebruik, maar dat kan niet voordat er een keuze is gemaakt welke componenten van kraakbeen we in beeld willen brengen. Kraakbeen is een specifiek soort bindweefsel wat op het uiteinde van botten zit, zodat de gewrichten goed kunnen bewegen en krachten kunnen weerstaan. Kraakbeen is ongeveer twee tot vier millimeter dik en bestaat voornamelijk uit water, collageenvezels en glycosaminoglycanen (GAGs). In dit water zit ook een bepaalde hoeveelheid ionen, met name natrium. Wanneer kraakbeen schade oploopt, kan het minder water vasthouden en wordt het daardoor minder stevig. Hierdoor vloeien de GAGs langzaam weg en kunnen collageenvezels breken.

In dit proefschrift is de keuze gemaakt om twee onderdelen van kraakbeen af te beelden, namelijk de GAG-concentratie en de collageenstructuur. Dit hebben we gedaan door gagCEST MRI en sodium MRI toe te passen om de GAG-concentratie te meten en T2\* mapping om de collageen concentratie in beeld te brengen.

Dus nu we onze componenten in het kraakbeen weten, is de volgende stap voor klinische implementatie van nieuwe sequenties een ex vivo validatie. We hebben ervoor gekozen om onze natriumscans te valideren in ex vivo tibiale plateaus van patiënten die een totale knie vervanging ondergingen. Onze hypothese was dat we, afgezien van het meten van de fixed charge density (FCD), natriumbeeldvorming konden gebruiken om de stijfheid van kraakbeen te meten. We konden onze hypothese niet bevestigen, alhoewel we aangetoond hebben dat natriumconcentratie samenhangt met de permeabiliteit van het kraakbeen. De methode en de resultaten van dit onderzoek, inclusief correlatie met DMMB-analyses, zijn beschreven in hoofdstuk 3.

In hoofdstuk 4 hebben we deze ex vivo experimenten opgeschaald naar onderzoek in gehele gewrichten, in dit geval carpale gewrichten van Shetland-pony's. Deze Shetland-pony's maakten deel uit van een groter experiment dat het effect van een groefmodel testte, een model wat uiteindelijk post-traumatische artrose zou moeten veroorzaken. We gebruikten T2\* mapping om inzicht te krijgen in het collageenvezelnetwerk van het kraakbeen. Met deze techniek waren we in staat om verschillen in gemiddelde T2\* tijd tussen aangedaan en gezond kraakbeen aan te tonen - waarmee we een eerste stap hebben gemaakt om in patiënten onderscheid te kunnen maken tussen gezond en beschadigd kraakbeen.

De volgende stap na ex vivo validatie is de in vivo toepassing, en met name de haalbaarheid binnen een klinische aanvaardbare scantijd. We hebben een haalbaarheidsonderzoek opgezet voor gagCEST MRI, om de haalbaarheid en de mogelijkheden van gagCEST MRI bij een groep patiënten te beoordelen, in dit geval patiënten met kraakbeenherstel. We toonden in hoofdstuk 5 aan dat we gagCEST MRI konden toepassen in een klinisch haalbare scantijd van zeven minuten en toonden een hoge stabiliteit en reproduceerbaarheid aan.

Nu we de haalbaarheid hebben aangetoond, zijn we nog een stap verder gegaan en hebben we geprobeerd aan te tonen dat gagCEST kan meten wat we ervan verwachten: (vroege) kraakbeenschade. In hoofdstuk 6 hebben we een pilotstudie uitgevoerd waarbij we gagCEST beelden van patiënten voor een totale knie vervanging hebben verkregen, waarbij we de stukken kraakbeen (die verwijderd zijn om de prothese te kunnen plaatsen) hebben gebruikt om die met elektromechanische metingen en biochemische assays te relateren. Wij toonden aan dat er een duidelijke relatie is tussen gagCEST en elektromechanische metingen, zowel op de laterale als de mediale zijde van de knie. Dezelfde correlatie werd aangetoond voor gagCEST met biochemische testen (DMMB), hoewel de correlatie op de laterale zijde ontbreekt.

Samenvattend toont dit proefschrift de toepasbaarheid van 7T MRI in beeldvorming en kwantificering van kraakbeen in verschillende stadia van (technische) ontwikkeling aan. Dit proefschrift beschrijft verschillende stappen die nodig zijn om beeldvormingsprotocollen in de klinische praktijk te implementeren.

## Appendices

## Dankwoord

Tijdens het schrijven van dit proefschrift kwam ik steeds meer mensen tegen die het verdienen om in dit dankwoord te staan – ik hoop dat ik niemand vergeten ben.

Allereerst wil ik Dennis, mijn promotor, bedanken. Bedankt dat je altijd alles met een positieve insteek probeert te bekijken, zelfs als dat lastig is. Ik heb waardering voor je extreme doorzettingsvermogen, in het pushen voor abstracts van de ISMRM tot het realiseren van de METAscan, iets wat de MRI wereld echt gaat veranderen. Nu nog hopen dat er een mooie MSK lijn bij de META terecht komt en dan is het project compleet!

Keita, my sincere thanks for all the productive, in-depth discussions we had. You always tried to challenge me to think for myself and not take everything for granted. I enjoyed the collaboration with you and your colleagues in Eindhoven.

Ik zou graag alle leden van de beoordelingscommissie, prof. dr. B.W. Raaymakers, prof. dr. ir. A.J. Nederveen, prof. dr. H.H. Weinans, prof. dr. C.T.W. Moonen, dr. R.J.H. Custers en prof. dr. ir. C.A.T. van den Berg hartelijk danken voor het beoordelen van mijn proefschrift en hun bereidheid plaats te nemen in de oppositie.

Ik wil graag van de gelegenheid gebruik maken om de klinische afdelingen waarmee we samen werken te bedanken. Roel en Nienke, dank voor het includeren van patiënten of het verzorgen van stukken kraakbeen waar ik test scans op kon doen. Hopelijk komen er mooie resultaten uit de nieuwe IMPACT studie! Niet te vergeten Lucienne en Mattie, voor alle hulp op het lab in het Hubrecht. Ook wil ik graag Simon en Mylène bedanken voor de prettige samenwerking, ik hoop dat de KJD/Meta studie snel kan gaan draaien.

Zonder onze 7T scanner was dit proefschrift er nooit geweest. In de categorie zonder hen was dit proefschrift er ook niet gekomen: Fredy, dank voor alle hulp rondom het scannen, ontwikkelen van protocollen en geouwehoer over fietsen – hoe kan het dat ik je dan toch maar een keer echt op een racefiets heb gezien? Sylvia, de echte organisator van de 7T groep, altijd in voor een praatje. Hans, Tijn: hartelijk dank voor alle troubleshootings bij de 7T! Ik denk dat de kniespoel een rode draad door mijn proefschrift is, iets wat zelfs geëindigd is in een apart hoofdstuk, met dank aan Aidin. Natuurlijk ook dank aan de rest van de coilboys (Mark, Dimitri, Luca, Erik, Ingmar), die altijd klaar staan om te helpen als er weer eens wat stuk was.

Dan wil ik een heel aantal collega's bedanken waar ik met veel plezier mee samen heb gewerkt. Martijn, dank voor alle fitjes die je gedraaid hebt en goede wetenschappelijke discussies (met of zonder whisky). Tim, we hebben ons uiterste best gedaan voor diffusie in kraakbeen op 7T. Maar je weet wat ze zeggen: we had many collaborative

## Appendices

projects, most of them failed. Vitaliy, thanks for all our discussions on CEST – the solution to everything. Anneloes, ik noem je vaker een matlabber dan een dokter, maar ik heb er alle vertrouwen in dat je het ook gaat maken op dat laatste vlak! Razmara, eerst als begeleider tijdens mijn M3 stage maar later ook als collega. Naast “oude” collega’s wil ik ook mijn nieuwe collega’s bij Lygature bedanken dat ik de tijd en ruimte heb gekregen om mijn proefschrift netjes af te ronden.

Naast al het harde werken hebben we ook een sportieve groep rondom onze 7T; op de racefiets met de Cycling for Science crew of een rondje hardlopen met Bart en Janot. Dank voor de mentale ondersteuning tijdens mijn marathoningstraining en de goede gesprekken! Naast al dit sportieve gedoe moet er natuurlijk ook ontspannen worden: Oscar, ik ben blij dat je me aangestoken hebt met het koffie virus en het leren hoe je een goede cappuccino maakt. Niek en Peter, naast dat jullie me altijd bijstaan met een goed glas whisky wil ik jullie ook heel erg bedanken dat jullie op deze dag letterlijk en figuurlijk achter mij staan!

Dan wil ik de rest van de 7T groep natuurlijk ook bedanken voor alle borrels, vierdaagsefeesten, divisie-beeld-feesten en andere gelegenheden: Arjan, Arjen, Erwin, Jeroen, Carel, Evita, Lisa, Carlo, Tine, Mario, Kyung-Min, Rick, Seb, Ria, Lieke, Zahra, Ayhan, Mike, Edwin, Kees, Quincy, Sarah, Deji, Mike, Stefano, Jeanine, Jacob-Jan, Wybe, Alessandro, Alexander, Jaco, Natalia en natuurlijk ook alle studenten!

Zonder een fijne verzameling van vrienden en familie om mij heen was dit proefschrift er nooit gekomen. Dank voor de vele whisky-avonden, nog meer koppen koffie, fietstochten, spelletjesavonden, fietsvakanties, borrels, weekendjes weg en nog veel meer. Dat er nog veel mogen volgen!

Lieve pap, mam en zus: dank dat jullie er altijd voor mij zijn. Ik vind het altijd erg fijn om weer in Raalte te komen en zal dat ook nog vaak blijven doen. Ik ben blij dat mijn familie nog aanvulling heeft mogen vinden in Dalen en omstreken. Heel erg bedankt voor al het vertrouwen en de steun in de afgelopen jaren.

Lieve Floor, ik kan niet beschrijven hoe fijn ik het vind dat jij er altijd was de afgelopen jaren, ook al zaten we soms op afstand in Amerika of Denemarken. We zijn allebei gegroeid in ons professionele leven, maar zo mogelijk nog meer in ons leven samen. Op dat er nog vele mooie jaren samen mogen volgen!

## Publication list

Brinkhof S, Nizak R, Khlebnikov V, Prompers JJ, Klomp DWJ, Saris DBF, Detection of early cartilage damage: feasibility and potential of gagCEST imaging at 7T, *European Radiology* 28 (7), 2874-2881

Brinkhof S, Haghnejad AA, Ito K, Markenroth Bloch K, Klomp DWJ, Uncompromised MRI of knee cartilage while incorporating sensitive sodium MRI, *NMR in Biomedicine*, e4173

Brinkhof S, Froeling M, Janssen RPA, Ito K, Klomp DWJ, Can sodium MRI be used as a method for mapping of cartilage stiffness? *manuscript submitted*

Brinkhof S, te Moller NCM, Froeling M, Brommer H, van Weeren R, Ito K, Klomp DWJ, T2\* mapping in an equine articular groove model – visualizing changes in collagen orientation, *Journal of Orthopaedic Research*, 2020

Brinkhof S, Nizak R, Sim S, Khlebnikov V, Quenneville E, Garon M, Klomp DWJ, Saris DBF, In Vivo Cartilage Quantification with gagCEST MRI: correlation with cartilage properties *manuscript submitted*

## Conference proceedings (first author only)

Brinkhof S, Nizak R, Khlebnikov V, Klomp DWJ, Saris DBF, 3D gagCEST in knee cartilage at 7T, 13th International Cartilage Regeneration and Joint Preservation Society World Congress 2016 in Sorrento (oral presentation)

Brinkhof S, Nizak R, Khlebnikov V, Prompers JJ, Klomp DWJ, ten Haken B, Saris DBF, Correlation of 7T gagCEST MRI with Electromechanical and Biochemical Properties of Femoral Articular Cartilage, 9th annual meeting International Society for Magnetic Resonance in Medicine Benelux 2017 in Tilburg (oral presentation)

Brinkhof S, Nizak R, Sim S, Khlebnikov V, Klomp DWJ, Saris DBF, Correlation of 7T gagCEST MRI with Electromechanical and Biochemical Properties of Femoral Articular Cartilage, 23th annual meeting International Society for Magnetic Resonance in Medicine 2017 in Hawaii (power pitch and digital poster - Magna Cum Laude Merit Award)

Brinkhof S, Nizak R, Khlebnikov V, Prompers JJ, Klomp DWJ, ten Haken B, Saris DBF, 3D gagCEST of articular cartilage in the knee at 7T correlates with clinical findings, 23th annual meeting International Society for Magnetic Resonance in Medicine 2017 in Hawaii (traditional poster)

## Appendices

Brinkhof S, Zhang Q, Froeling M, Strijkers GJ, Nederveen AJ, Ito K, Klomp DWJ, Depth dependence of diffusion in articular cartilage of the knee visualized at 7T, 10th annual meeting International Society for Magnetic Resonance in Medicine Benelux 2018 in Antwerp (traditional poster)

Brinkhof S, Khlebnikov V, Visser F, Hoogduin JM, High resolution 1 mm isotropic semi continuous wave gagCEST of articular cartilage using parallel transmit at 7T, 24th annual meeting International Society for Magnetic Resonance in Medicine 2018 in Paris (digital poster)

Brinkhof S, Zhang Q, Froeling M, Strijkers GJ, Nederveen AJ, Ito K, Klomp DWJ, Depth dependence of diffusion in articular cartilage of the knee visualized at 7T, 24th annual meeting International Society for Magnetic Resonance in Medicine 2018 in Paris (digital poster)

Brinkhof S, Ito K, Klomp DWJ, Multiparametric cartilage MRI within 30 minutes, 11th annual meeting International Society for Magnetic Resonance in Medicine Benelux 2019 in Leiden (traditional poster)

Brinkhof S, Haghnejad AA, Ito K, Markenroth Bloch K, Klomp DWJ, Uncompromised MRI of knee cartilage while incorporating sensitive sodium MRI, 25th annual meeting International Society for Magnetic Resonance in Medicine 2019 in Montreal (digital poster)



## Curriculum vitae

Sander Brinkhof (August 25th, 1991, Deventer) obtained his MSc in Technical Medicine at the University of Twente, with a focus on Medical Imaging & Interventions, for which he followed rotations in the UMC Groningen, UMC Utrecht and Fred Hutchinson Cancer Center in Seattle. This master program was concluded with research at the Orthopaedics department in the UMC Utrecht, focusing on the implementation of a new MRI technique to assess the cartilage before repair surgery. He also obtained a MSc in Health Sciences with a thesis assessing the budget impact of lung cancer screening in the Netherlands.



The work carried out in the Orthopaedics department continued into a PhD program at the 7T MRI group in the UMC Utrecht, focusing on quantitative MRI protocols for articular cartilage assessment of which the results are described in this thesis. Towards the end of this PhD research, Sander started to work as a program manager at Lygature.